A new earthquake clustering algorithm based on space density and inter-event time analyses

Doctoral Thesis

A new earthquake clustering algorithm based on space density and inter-event time analyses

空間密度と発生間隔解析に基づく新たな地震群抽出アルゴリズム

Wei Peng

平成 29 年

Doctoral Thesis

A new earthquake clustering algorithm based on space density and inter-event time analyses

空間密度と発生間隔解析に基づく新たな地震群抽出アルゴリズム

Wei Peng
(彭　葦)

Department of Geophysics
Graduate School of Science
Tohoku University

Thesis Committee Members

Professor	Shinji Toda (Chair, Supervisor, IRIDeS, Tohoku University)
Professor	Toru Matsuzawa
Professor	Motoyuki Kido (IRIDeS, Tohoku University)
Associate Professor	Tomomi Okada
Associate Professor	Yo Fukushima (IRIDeS, Tohoku University)

2017

Acknowledgements

To my supervisor, Professor Shinji Toda, thanks for all of the support, encouragement and brilliant suggestions for my study, and my life. Words cannot express how much I appreciated it. It was a bless learning under your guiding.

I would like to thank Dr. Ross stein of the US Geological Survey, Associate Prof. Jiancang Zhuang of the Institute of Statistical Mathematics, Associate Prof. Bogdan Enescu of the Graduate School of Science Department of Geophysics of Kyoto University for their helpful suggestions for my study.

Thanks to the other members of my dissertation committee, Professor Toru Matsuzawa, Professor Motoyuki Kido, Associate Prof. Tomomi Okada and Associate Prof. Yo Fukushima for their reading and comments.

I would also like to thank all the staff and member of the AOB center, Tohoku University and IRIDeS, Tohoku university for their unfailing assistance and support.

A very grateful to Kate Huihsuan Chen, National Tawian Normal University, you are my teacher, my friend. You are the one who encouraging me to study abroad, I cannot be here without you.

A special thanks to Junko Omori and the member of the Mori room of Tohoku University who kindly take care of foreigner students.

A special thanks to Yuchen Ling, Chaokai Liang and Wenzoe Chen who have supported me spiritually all along.

Finally, huge thanks to my family: my parents and to my sisters for their unconditionally love, understanding and support.

Abstract

In this study, I present a new catalog-based algorithm to identify background seismicity and spatiotemporal clusters for cases characterized by both mainshock-aftershock sequence and swarm activity. We found that simple equations with a few parameters can identify the background seismicity from an earthquake sequence.

Background seismicity plays an important role on earthquake hazard estimation. The scientific background of earthquake hazard estimation is to realize earthquake scenarios with knowing physical knowledge, and one of the approaches to understand earthquake scenarios is to study the seismicity. Seismicity based on the mechanism of the occurrence could be separated into background seismicity and triggered seismicity. Background seismicity, also referring as tectonic seismicity, is described as the earthquakes who are independent of each other, the term independent indicates that the occurrence of the earthquakes are not associated with the stress perturbation of the previous earthquake but related to the elastic strain accumulation by the tectonic loading and as a product by releasing the energy through the slip on a fault. It could be seen as a homogenous condition on a large scale of areas. On the other hand, triggered seismicity indicates the occurrence of earthquakes is related to a previous large earthquake (mainshock). These triggered earthquakes are often referred to as aftershocks. A sudden stress perturbation imparted by a mainshock caused the occurrence of the aftershocks. There is another special case of earthquake cluster called earthquake swarm, which is also an earthquake cluster, but their occurrence is mainly driven by the aseismic slip or fluid migration around the volcanic area. It is important to distinguish those groups, the variety of applications such as seismic hazard assessment or earthquake prediction and seismicity rate change estimation.

Previous researches for separating the earthquake clusters with the background seismicity all have success on modeling the mainshock-aftershock sequence but they faced a difficulty on separating swarm sequence. The reason is because the seismicity of swarm sequence does not usually follow the aftershock decay law, and it has a variation in seismicity rate, earthquake productivity, magnitude, and its duration. Because the inconsistence of properties in the swarm sequence, it makes a huge difficulty to separate those events with pervasive empirical laws. Recently, a study using mean seismicity rate as a primary parameter to detect enhanced seismicity rate sequences successfully identified earthquake clusters in a swarm dominate region. Using seismicity rate to divide earthquake catalog into several enhanced seismicity sequences enables us to select more independent declustered earthquakes. However, the choice of parameters for combining sequences is arbitrary and largely influences their results.

To select the spatio-temporal clusters, the algorithm first searches spatial clusters by considering the spatial distribution with time in a 2-D cell-gridded map. Second, the algorithm identifies temporal sequences from a spatial cluster by comparing inter-event time with a temporal threshold. A self-driven time-dependent parameter is also presented based on the observation of earthquake inter-event time. The advantage of this algorithm is that only two parameters are required for near-complete earthquake declustering process. A filtering process is designed to find the proper parameter combination to maximize the number of declustered earthquakes. Several tests are presented with JMA catalog recorded

from 1998 through 2016 in and around Japanese Islands. The results indicate that this algorithm is capable of selecting spatiotemporal clusters with regard to the various tectonic environments. For deeper subduction-related earthquakes, we have further developed the 2D cell grid to 3D cubic grid system to adopt our approach to a wide range of seismicity. Finally, we compare our declustered catalogs with ones computed from several other declustering algorithms and suggest that this new algorithm would be competitive with other declustering/clustering techniques.

By extracting spatiotemporal earthquake clusters properly from an input catalog, background rate of seismicity could be used as a stress indicator, and change in background seismicity may suggest stress perturbation related to a large earthquake is occurring. In our declustered catalogs, we found that background seismicity rate increase in several areas in Honshu Island after the M=9.0 2011 Tohoku-oki earthquake. Further studies may prove that fluctuation of true background rate of seismicity might be one of the key factors to evaluate time-dependent earthquake hazard.

Contents

Chapter 1 Introduction

To assess earthquake hazard, background seismicity plays an important role on investigating the frequency of the future seismicity [Cao et al., 1996; Wiemer, 2000; Kafka, 2002; Kagan and Jackson 2000]. Based on the characteristics of distribution in space and time, observed earthquakes could be divided into triggered events and secular background activity. In terms of the observed rate of seismicity, clustered seismicity can be mainly categorized into mainshock-aftershock sequence [Omori 1894; Utsu 1970] and swarm sequence [Mogi, 1963; Scholz, 2002]. Generally, clustered seismicity indicates the earthquakes that are triggered by other earthquakes. Background seismicity, on the other hand, describes as the seismicity which is independent each other and often reflected from the state of tectonic loading. Studying clustered seismicity can help us understand the earthquake mechanism such as static triggering [e.g., King et al., 1994; Stein et al., 1994; Toda et al., 2012], dynamic triggering [e.g., Kilb et al., 2000; Felzer and Brodsky, 2006], or aseismic triggering [e.g., Peng and Gomberg, 2000]. On the other hand, analyzing background seismicity enables us to estimate the regional stress level. In addition, anomalies from stable background seismicity may suggest the stress perturbation on a regional scale [Ogata 2005].

There are several methods already proposed to distinguish triggered seismicity from background seismicity. These approaches are often referred to as earthquake clustering/declustering methods [Utsu, 1970; Gardner and Knopoff, 1974; Reasenberg, 1985; Ogata, 1988; Frohlich and Davis, 1990; Zhuang et al., 2002]. However, despite their efforts, each algorithm has its own advantage and disadvantage, and the best and versatile method does not exist. A common standard to test the declustering process is if the computed background seismicity follows Poisson behavior in space and time.

The Epidemic Type Aftershocks Sequence [ETAS, Ogata,1988] Model, is one of the most widely used models in the recent earthquake hazard estimation. The ETAS model describes seismicity as a point process, which consists of a constant background seismicity with a triggering process. The strength of the ETAS model is that every earthquake has a capability of generating its own aftershocks, and the productivity of aftershocks are controlled by the empirical Omori-Utsu law. But a limitation of ETAS model is not to well reproduce seismic swarm sequence. The reason is that the temporal distribution of swarm sequence cannot be simply described by aftershock decay law and do not follow any epidemic type behavior. Recently, cumulative rate analysis [CURATE, Jacobs, 2013] is proposed to find spatio-temporal earthquake clusters from the swarm dominated area in New Zealand. This analysis is fundamentally different from the others because they do not involve any direct and arbitrary assumptions that cause the biases. The CURATE method employs an average rate of seismicity as a threshold for detecting enhanced seismicity rate sequence. However, arbitrary choice of additional parameters in the CURATE method exposes a limitation to apply to other areas.

In Chapter 1, we first describe the reason why we need to seek a precise rate of background seismicity. We then briefly introduce the previously published major declustering techniques and their pros and cons.

In Chapter 2, we propose a new algorithm that is different from most of the declustering techniques

that aimed to “remove” the aftershocks. Our algorithm first identifies spatial cluster, which is an enhanced seismicity density area that can be seen on the seismicity density map. We then deal with how to automatically select enhanced seismicity density area (spatial clusters). This is a process to link the earthquakes occurred closely in space and time. During this process, two parameters are adopted, S° for spatial dependency and T (days) for temporal dependency. After selecting spatial clusters, we identify spatiotemporal sequence by evaluating temporal behavior in each spatial cluster. Based on the observation of earthquake inter-event times, we adopt a self-driven time-dependent temporal threshold to quantify the temporal relationship between two continued events. This time-dependent temporal threshold is represented as the minimum waiting time for the next event to occur. Earthquake catalog adopted in this algorithm would be separated into spatiotemporal sequences and background seismicity (combination of spatially independent event and temporally independent event). To find the proper combination of S and T, we design a parameter filtering process to find the proper parameter combination from a range of S and T. The suggested combination of the parameters is aimed for not only produced a smooth background seismicity but also keeping the maximum number of the background events. The primary result of this algorithm adopted in western side of Hokuriku region, Japan with JMA catalog shows that this technique is capable of selecting the spatiotemporal sequence in such tectonic heterogeneous environment.

To further investigate the algorithm, in Chapter 3, we adopt this algorithm to several areas in and around the Japanese Islands. We select the test areas based on various seismo-tectonic environments.

In Chapter 4, we discuss the issues raised by the tests in Chapter 3. For example, we find that background seismicity decreasing after the 2011 Tohoku-oki earthquake in Tohoku area is due to the over-declustering of 2-Dimensional gridded system. We then expand the 2-Dimension grid into 3-Dimension cube system. The decreased rate of background seismicity then disappeared with the 3-Dimension cube, instead, a sudden increase of background seismicity was observed. This sudden increase of background seismicity associated with the 2011 Tohoku earthquake also appeared in the Iwate region, suggested that a local stress field had been perturbed due to the stress imparted from the M9.0 Tohoku earthquake. Another issue is seismicity increase occurred after the 2016 Kumamoto earthquake in the central Kyushu area. We found that the increase is due to the limitation of the time-dependent threshold we designed for quantifying the temporal relationship, which attracts our attention to future development of the algorithm.

1.1 Background seismicity to detect seismic anomaly

Several studies have indicated there exists seismic quiescence prior to large events in and near their epicenters [e.g., “Mogi’s donuts” in Mogi, 1979; Wyss and Habermann, 1988; Katsumata, 2015]. Seismic quiescence in space and time is defined as and detected by seismicity rate decrease in a seismically active region during a specified period, compared to stable activity in the region. However, it is not yet clear how common this phenomenon is, what its characteristics are, and what types of physical mechanism bring such spatiotemporal dormancy preceding large earthquakes. Recent studies suggested that aseismic

slow slip preceding a major earthquake that might have occurred on the plate interface around major subduction zones may contribute to hampering regional seismicity. The spatial correlation between area of seismic quiescence and location of the aseismic fault plane suggest that the seismic quiescence might be related to stress reduced by preceding aseismic slip, which might lead a contribution on the earthquake prediction [Seno, 2004; Katsumata, 2015]. Two commonly used stochastic values for computing seismicity rate change are *z*- value [Habermann, 1983] and β- value [Matthews and Reasenberg, 1988]. *Z*- value is to compare the seismicity rate for two different periods by the following equation

$$Z = \frac{\frac{n_1}{T_1} - \frac{n_2}{T_2}}{\sqrt{\frac{n_1}{T_1^2} + \frac{n_2}{T_2^2}}}, \tag{1.1}$$

where T_1 (background) represents overall period except the time window of interest T_2, and n_1 and n_2 are the number of earthquake samples in these periods. A general computation for *Z*-value is implemented into a software package ZMAP [Weimer, 2001] operated in MATLAB. ZMAP computes seismicity rate change simply by generating a map with equally sized grid cells, and separating earthquake occurred in each cell. Then earthquakes occurred in different grid cells could be sampled in a giving time window. A comparison of seismicity rate between a giving time window (T_2) and total period (background, T_1) could be presented. Figure 1.1 shows a schematic plot for how to compute *Z*-value. *Z*-values can be also calculated and shown as a function of time shifting the range of time window (T_2). According to equation (1.1), a positive *Z*-value indicates a decrease in seismicity rate, whereas a negative value indicates an increase in seismicity rate. The seismic anomalies could be identified by the variation of *Z*-value. The previous study has suggested $|Z| \geq 5$ would be reckoned as a significant change over background noises [Katsumata, 2015, 2017].

The other value commonly used to detect the seismicity rate change is β- value defined by the following equation

$$\beta_n(t,\delta) = \frac{M(t,\delta) - n\delta}{\sqrt{n\delta(1-\delta)}}, \tag{1.2}$$

where n indicates the number of independent events in the period *T* (background), and $M(t,\delta)$,the number of samples between time interval $(t-\delta,t)$ under the condition of $t<T$. The β statistics demonstrates a direct difference between the observed number and the expected number of earthquakes. A modified standard β approach for seismicity [Matthews and Reasenberg, 1988; Reasenberg and Simpson, 1992] is defined as

$$\beta = \frac{N_a - N_e}{\sqrt{v}}, \tag{1.3}$$

where N_a represents the number of earthquakes occurred after an event and N_e represents the expected earthquake number estimated by the seismicity rate before that event. A positive β- value indicates an increase in seismicity rate and a negative value indicates a decrease in seismicity rate. β-value is more sensitive than *Z*-value, a slight change in seismicity can be emphasized in β-value. But it leads to a difficulty to find the increase in seismicity compared to rate decrease [Matthews and Reasenbreg, 1988]. According to equation (1.1) and equation (1.2), rate of background seismicity controlled the significance of the seismicity rate change. Therefore, using proper background seismicity in such analysis becomes

essential. Previous studies suggest that changes in seismicity rates are easily produced by any effects, such as the improvement of the seismic station coverage leads to increase of seismicity rate or the abundant aftershock activities lead to reduce potential seismic anomalies. Therefore, to investigate precise and reliable temporal changes in seismicity, a homogenous earthquake catalog should be presented [Habermann, 1987].

1.2 Forecasting seismicity after a mainshock

The values introduced above are the perspectives of statistic approaches. The ultimate purpose to quantify these statistical values is to predict the time and location of future large earthquakes. For the physical aspects, another approach for seismic hazard estimation is to forecast seismicity after mainshocks by considering the effect of the coseismic stress change. Aftershocks and other triggered earthquakes could be interpreted as a product of stress transfer from a mainshock source. Such a stress perturbation due to a mainshock and associated seismicity rate change could be comprehended by the static Coulomb stress change and/or dynamic stress change. Based on recent numerous studies, remote triggering aftershocks are often related to dynamic stress change caused by the passage of seismic wave, whereas static Coulomb stress change dominates near-field aftershock triggering behavior. The rate and state friction law, introduced by Dieterich [1992, 1994], has been often introduced to convert stress perturbation into time-dependent seismicity with background rate of seismicity in a region. Based on the laboratory experiment, this law describes a relation between the physical properties and its associated slip behavior on a fault. By a simple assumption that earthquake nucleation is associated with the instability of the initial slip on a fault, seismicity rate R is found to evolve following an equation,

$$R = \frac{r}{\gamma \dot{\tau}_r}, \tag{1.4}$$

while r indicates background seismicity, $\dot{\tau_r}$ indicates reference shear stressing rate and γ indicates a time-dependent state variable with

$$d\gamma = \frac{1}{A\sigma}[dt - \gamma dS], \tag{1.5}$$

where A represents a constitutive parameter. S indicates a modified Coulomb stress function as

$$\Delta S = \Delta\tau + \mu' \Delta\sigma, \tag{1.6}$$

where $\Delta\tau$ and $\Delta\sigma$ represent the changes in shear stress and normal stress, and μ indicates the effective coefficient of friction. According to Dieterich [1994], assuming a constant stressing rate following a stress step and steady-state seismicity rate prior to a stress step, the state variable γ can be described as

$$\gamma_n = \gamma_{n-1} exp\left(\frac{-\Delta S}{A\sigma}\right), \tag{1.7}$$

γ_n and γ_{n-1} represents the state variable in different stress states, and substituting equation (1.7) to equation (1.4), seismicity rate R in any stress perturbation yields

$$R(t) = \frac{r}{\left[exp\left(\frac{-\Delta S}{A\sigma}\right) - 1\right] exp\left(\frac{-t}{t_a}\right) + 1}, \tag{1.8}$$

where t_a is the aftershock duration, indicating the time comes back to the background level and derived by

$$t_a = \frac{A\sigma}{\dot{t}}. \tag{1.9}$$

The Dieterich model can be used to forecast seismicity rate change caused by stress change after a mainshock, or any stress perturbation caused by aseismic slip. According to equation (1.8), the expected seismicity rate is directly affected by the level of background rate, and it is also worth noting that equation (1.8) is only valid when the seismicity rate prior to the stress perturbation is underlying steady state condition.

Cocco et al., [2010] suggests that background seismicity rate in a steady state should not change with time, which leads to a general statement that background seismicity should follow Poissonian behavior. Stable Poisson distribution of background seismicity indicates that earthquakes occur independently each other. To incorporate such a statistical hypothesis into model, random (Poissonian) behavior in seismicity must be assumed. But a fundamental but crucial question is how to quantify proper background seismicity. During the past 40 years, there are several methods and models challenged to estimate true background seismicity. Most of the previous studies and their approaches concentrated on removing clustered seismicity (aftershocks) from an earthquake catalog, and those methods are therefore often described as "earthquake declustering method." Untill now there does not exist the best declustering algorithm to properly describe background seismicity. Several declustering algorithms are suitable for dealing with data with certain types, and some are fit to handling data with a particular type of space and time distribution. In general, declustering algorithms can be divided into deterministic and stochastic types. Deterministic type focuses on finding the independent event, whereas stochastic type uses probability criterion to estimate the chance that earthquake would be triggered by the previous one. Regardless of different types, the basic concept of the declustering algorithm is to separate earthquake clusters from the original catalog by quantifying the spatial and temporal dependency between earthquakes under some criteria.

Table 1 lists several major declustering algorithms published since 1970s and detailed information is presented in the following section.

1.3 Types of declustering methods

1.3.1 Window method

The Gardner and Knopoff [1974] method is a straightforward technique that focuses on the creation to decluster a catalog. The method quantifies the spatial and temporal dependency of earthquakes by a set of magnitude-dependent space-time windows based on visual scanning of earthquake clusters in Southern Californian earthquake catalog. An approximation of the windows sizes is given in

$$L = 10^{0.1238\times M+0.983}\text{, (km)}, \tag{1.10}$$

$$t = \begin{cases} 10^{0.032\times M+2.7389}, & M < 6.5 \\ 10^{0.5409\times M-0.547}, & M \geq 6.5 \end{cases}\text{, (days)} \tag{1.11}$$

where L indicates the length of the space window (km) and t indicates the length of the time window (day). This method removes earthquakes occurred in the space-time window defined by other earthquakes, the remaining events are considered as background seismicity. Note that the space-time window size might be changeable depending on target areas.

1.3.2 Linked method

Reasenberg [1985] developed an algorithm that identifies aftershocks by linking earthquakes into clusters based on a concept of spatial and temporal interaction zone. In the Reasenberg's theory, spatial interaction zone is defined by assuming a circular crack radius for each event and searches within its vicinity for aftershocks, which yields a spatial extension = Q x source dimension (S), where Q is a non-dimensional constant parameter governed the amplitude of spatial extension and S is driven by

$$M_0 = \mu S\overline{D} = \frac{16}{7}\Delta\sigma a^3 = \left(\frac{16\Delta\sigma}{7\pi^{\frac{3}{2}}}\right)S^{\frac{3}{2}}$$

[Kanamori & Anderson, 1975], (1.12)

and temporal interaction zone is based on the Omori-Utsu decay of observed aftershock activity with probability form,

$$\tau = \frac{-\ln(1-P)t}{10^{2(\Delta M-1)/3}} \tag{1.13}$$

The equation (1.13) describes a time to wait to be P confident of observing the next event in the sequence. P indicates the probability of detecting the next event and ΔM = (M - Mc). Mc indicates the minimum magnitude of completeness, which defines a minimum magnitude that earthquakes magnitude above Mc is considered to be reliably detected. The Reasenberg's algorithm needs two free parameters Q and τ. In general, Q is set to be 10, which is according to the maximum distance of earthquakes estimate by the stress related process. τ gives a range from 1 to 10, which also indicates the maximum interaction time between two earthquakes is smaller than ten days. In summary, the Reasenberg's algorithm first estimates spatial extension of earthquakes by equation (1.12) and lasts a duration τ after the earthquake event by equation (1.13). If one earthquake falls into a window for another earthquake, both belong to the same cluster.

1.3.2.1 Shortcoming of Gardner and Knopoff and Reasenbeg declustering methods

The primary target for above declusteirng methods was for seismicity in California region, and the observation might only valid for those areas that are represented as seismo-tectonics in the San Andreas fault system. The Gardner and Knopoff [1974] method might have been extreme that declustered catalog only contained a few events and the Reasenbeg method might be too weak to select aftershocks adequately from the modern seismic catalog that include more small earthquakes [Luen and Stark 2012].

1.3.3 Stochastic EATS model

Stochastic process can analyze a time series data with a combination of probability controlled random variables, which can be adapted to a large number of various phenomena where the population of interest varies through time. Ogata [1988] first introduced Epidemic Type Aftershock Sequence (ETAS) model to reproduce the seismicity as a combination of background seismicity and its branch structure of all aftershocks. The seismicity rate λ as a function of time t yields

$$\lambda(t|H_t) = \mu + \sum_{t_i<t} \frac{Ke^{\alpha(M_i-M_c)}}{(t-t_i+c)^p}, \tag{1.14}$$

where μ indicates a constant background seismicity rate, t indicates time, K indicates the aftershock productivity, α represents the earthquake efficiency of a given magnitude at generating aftershocks, c and p are the parameters from the Omori-Utsu law. In the ETAS model, background seismicity rate μ follows a Poisson distribution. The ETAS model assumes every event can generate its own aftershocks, which gives the uniqueness and strength for modeling seismicity. For each earthquake event, the rate of aftershocks decreases in time according to the modified Omori-Utsu law. The rate of aftershocks of an earthquake with magnitude M_i increases exponentially with the size of Mi, which gives a similar description with the Gutenberg–Richter law. The ETAS model treats all parameters to be constant over a study region, the reasonable choice of the study region often becomes crucial. Zhuang [2002] then proposed the space-time ETAS model to overcome the issue. It incorporates a location function into the original ETAS model

$$\lambda(t,x,y) = \mu(x,y) + \sum_{\{k:t_k<t\}} k(m_k)g(t-t_k)f(x-x_k, y-y_k|m_k), \tag{1.15}$$

$$k(m) = Ae^{\alpha(m-m_c)}, \qquad m \geq m_c, \tag{1.16}$$

$$g(t) = \frac{p-1}{c}\left(1+\frac{t}{c}\right)^{-p}, \qquad t > 0, \tag{1.17}$$

$$f(x,y;m) = \frac{q-1}{\pi De^{\gamma(m-m_c)}}\left(1+\frac{x^2+y^2}{De^{\gamma(m-m_c)}}\right)^{-q}. \tag{1.18}$$

In the space-time ETAS, $\mu(x,y)$ indicates the background seismicity as a function of space. $k(m)$ indicates the aftershock productivity generated by magnitude m. $g(t)$ indicates the probability function of the modified Omori-Utsu law, and newly added $f(x,y)$ indicates location of aftershocks controlled by a probability function from the kernel function.

These stochastic models to identify background seismicity with probabilities share the following common processes:

1. Calculate the probability (P_i) that event i as the background event by

$$P_i = \frac{\mu(x_i,y_i)}{\lambda(t_i,x_i,y_i)}. \tag{1.19}$$

2. Generate a uniform random number Ui between 0 and 1.
3. If Pi > Ui, define event i as the background event.

1.3.3.1 Shortcoming for ETAS model

There are two crucial problems that the ETAS confronted. First, the ETAS model is model dependent, and different choice of area and time period varies the final result. Marsan and Lengline [2008] tackled to resolve this issue by adopting a non-parametric ETAS model in which every parameter settings are implicitly given by kernel function. Second, several studies addressed that the ETAS model failed to model seismic swarm sequence [e.g., Llenos et al., 2009; Harte 2012; Chouliaras et al., 2015], which is still unresolved. The main reason why ETAS cannot fully reproduce swarm sequence is that the temporal changes of swarm activity is not uniform. Swarm sequence could be regarded as an outlier from earthquake clusters. Instead, swarm sequence is a group of earthquakes occurred closely in space and time but does not include a significant mainshock unlike typical mainshock-aftershock sequence. During the swarm sequence, seismicity rate often seems to be randomized. Aftershocks following the largest event in the swarm sequence do not simply decay with time, makes swarm sequence puzzling. Recently, several studies modified the conventional ETAS model by changing the background seismicity (μ) or the aftershock efficiency (α) to fit swarm sequences, but their adjustments seem to be hindsight and not yet to make the proper contribution to forecast earthquakes prospectively [Llenos et al., 2009].

1.3.4 CURATE analysis

Jacobs et al., [2013] developed a cumulative rate analysis (CURATE) to overcome the difficulty of ETAS model for seismic swarm sequence. This analysis consists of two main steps. The first step is to select the enhanced seismicity rate sequence. Instead of using an empirical statistical function to model the seismicity, they connected earthquakes by time-dependent seismicity rate. CURATE analysis is the modified version of CUSUM (cumulative sum) analysis, which is a sequential statistical analysis for changing detection in a time series data

$$D = \frac{N(t_s, t_f)}{t_f - t_s}, \tag{1.20}$$

$$CURATE = N(t_s, t_i) - D(t_i - t_s), \quad t_s \le t_i \le t_f, \tag{1.21}$$

where D indicates the mean seismicity rate during time period (t_s,t_f), $N(t_s,t_f)$ indicates the observed cumulative number of earthquakes in time period (t_s,t_f), the CURATE at time t_i indicates the residual between observed cumulative number of earthquakes at t_i and expected cumulative number of earthquakes at t_i. For a time series data, according to equation (1.21), each positive slope of the CURATE represents an enhanced seismicity rate, and the positive slope can be simply represented as when an inter-event time between two continuous events is smaller than 1/mean rate. After enhanced seismicity rate sequence is identified, a "distance rule" is adopted to quantify the spatial dependency. The distance rule is used to remove earthquakes if the distance between an event location and the mean location of a seismic sequence chosen in the first step is over the defined distance rule. First two steps are an iteration process and the CURATE analysis continues working on the residuals until no enhanced seismicity rate sequences could be identified. The original input catalog would be divided into several enhanced seismicity rate sequences based on CURATE analysis. Next step is to focus on those enhanced seismicity

rate sequences and combine those sequences with distance rule and day rule. Two or multiple sequences would be then combined into one sequence if the spatiotemporal relationship is fulfilled with the following conditions:

1. The distance between mean location of sequences is smaller than distance rule.
2. The length of the sequences is overlapped or the time interval between sequences are shorter than day rule.

The CURATE analysis focuses on extracting earthquake clusters and the parameters could successfully be adopted all kinds of earthquake sequences, and it may satisfactorily overcome the shortcoming of the ETAS model on a swarm dominated area.

1.3.4.1 Shortcoming of the CURATE analysis

Jacobs et al. [2013] suggests that using rate as the primary indicator for monitoring activity gives a better aspect to evaluate spatial dependency for earthquake occurrence. This independent treatment of distance enables to better identify sparse increases in activity and leads to better categorization of decay of sequences. However, a proper parameter set for distance rule and day rule is arbitrarily assumed and hardly adjustable.

1.4 Motivation

From a brief review of the existing algorithms above, we temporarily conclude that no best and versatile technique exists to properly decluster observed earthquakes. Some of them are only suited for a specific type of earthquakes, and some of them might be only applicable for certain areas. To capture the seismicity in more general perspective, we here develop an algorithm that aims to be suitable for any types of seismic sequences under any tectonic environments (mainshock-aftershock sequence, swarm sequence or in-between). Based on the knowledge of preexisting techniques in mind, that is, seismicity fitted by an empirical formula is only validated on the mainshock-aftershock sequence. We thus keep the advantage of the usage of seismicity rate parameter to be the primary parameter as the CURATE analysis reducing the arbitrary choice of additional parameters for our further investigation. In chapter 2, we propose a new algorithm. An initial test of this algorithm adopted in an area mixing inland mainshock-aftershock sequence with large swarm sequence demonstrates the new technique can select the spatiotemporal sequence in such tectonic heterogeneous environment. Chapter 3 shows a series of tests for earthquakes in and around the Japanese Islands. In Chapter 3, we adopt this new algorithm with the various areas to investigate the power of selecting spatiotemporal sequences; from a single mainshock-aftershock sequence to enhanced seismicity rate areas. In Chapter 4, we discuss several strengths and limitations recognized from these applications in Chapter 3, and then conclude our study in Chapter 5.

Table 1.1 List of major declustering techniques since 1970.

Methods	Spatial dependency	Temporal dependency	Parameters	Issues
Window method Gardner and Knopoff [1975]	Empirical scaling Law	Empirical scaling Law	L (km),T (day)	Laws are not generally applicable
Linked method Reasenberg [1985]	Seismic moment	Omori-Utsu law (probability form)	S (m),τ (day)	Probability form is not generally applicable
ETAS model Ogata [1988]	x	Omori-Utsu law	$\alpha(M^{-1})$,$\mu(day^{-1})$,c(day), p,K	Omori-utsu law is not performed well with swarm
Space-time ETAS model Zhuang et al., [2002]	Kernel function	Omori-Utsu law (probability form)	$\alpha(M^{-1})$,$\mu(day^{-1})$,c(day), p,A,γ,Q,D(km) d,h (kernel bandwidth)	Omori-utsu law is not performed well with swarm
CURATE method Jacobs et al. [2013]	Free parameter	Mean seismicity rate	seismicity rate (day^{-1}) distance rule (km), day rule (day)	Subjective parameter choice

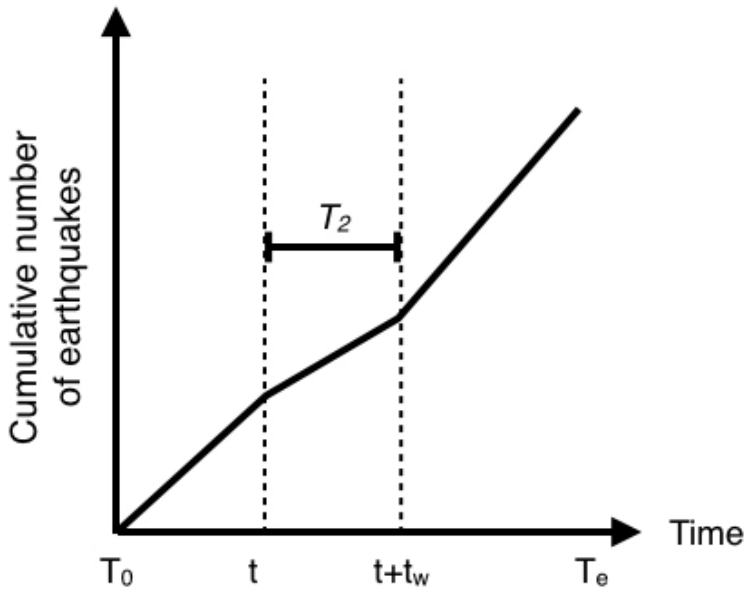

Figure 1.1 Schematic explanation of how to calculate Z-value. The Z-value is calculated for all times t between T_0 and T_e to T_w. According to the equation 1.1, T_2 represents the time period from t to $t + t_w$, and T_1 represent the time period from T_0 to T_e subtracting T_2. ($T_0<t<T_e$)

Chapter 2 A new algorithm

2.1 Multiple steps to find spatio-temporal clusters

Our newly proposed algorithm for clustering/declustering is based on detailed observations of seismicity in which a group of earthquakes occurred closely in space and time. In terms of spatial distribution, earthquake clusters can be visually identified as high density areas on a map. On the other hand, temporal distribution, earthquake clusters can be identified as a sudden increase of seismicity in a time series plot. In order to recognize earthquake clusters, a key factor is to quantify the temporal and spatial dependency between two continuous events without causality assumptions. This algorithm focuses on finding spatiotemporal earthquake clusters and discriminates from remaining events as background seismicity.

The new algorithm includes the following three steps. The first two steps are the primary processes that aim to extract clusters, and the final step is a filtering process to find the best clustered/declustered catalog from all the catalogs from the first two processes with a proper combination of parameters. Two parameters are adopted in the primary process (first two steps) and additional two parameters are adopted in the filtering process (final step).

At the first step, we deal with the spatial dependency. We first bound the space volume of the spatiotemporal earthquake sequences by selecting high seismicity density areas. The first step includes a linking process with spatial and temporal parameters and aims to identify high seismicity density areas from an earthquake catalog automatically.

After selecting high seismicity density areas, next step is to extract the enhanced seismicity rate sequences from those high seismicity density areas. To quantify the temporal dependency, we adopt the same concept as the CURATE analysis that compares an inter-event time of two sequential events to a temporal threshold. The second step is the modified version of CURATE analysis and intends to overcome the shortcoming of CURATE analysis. As we mentioned in Chapter 1, the CURATE analysis used two subjective rules to link the enhanced seismicity rate sequences. But these two rules directly affect the size and duration of the earthquake sequences. The only reason why two rules are required in the CURATE analysis is the simple usage of a constant mean rate throughout the study period. A constant rate in multiple runs of CURATE to reduce residuals leads to an unavoidable requirement of additional rules to combine the sequences. In the second step, instead of using a constant temporal threshold like CURATE, we seek to find time-dependent automatically determined temporal thresholds to quantify the relationship between two continuous events and try to select enhanced seismicity rate sequences in one run with these threshold values. A flowchart of this algorithm is shown in Figure 2.1.

2.1.1 Step 1 : Identifying the spatial clusters (neighboring cell connection method)

The purpose of step 1 is to identify high seismicity density areas. A dense seismicity area, what we call “spatial cluster,” represents a group of earthquakes occurred closely in space. To identify those spatial

clusters, here we adopt a linking procedure to connect events occurred nearby. Earthquakes would be linked if they occurred close enough, and the spatial dependency is quantified by a 2-dimension grid (S, in degree) discarding the information of hypocenter depth. However, if an area is enhanced in seismicity, it is possible that all of the earthquakes would be linked as one large spatial cluster. To avoid such a possible but unfavorable situation, we also introduce a temporal parameter T (in day) to select transient spatial clusters.

A simple schematic plot of step 1 is shown in Figure 2.2. Before the screening process started, an initial cluster number ($n_c = 0$ as the initial value) is set up for all events (events are sorted by ascending order of occurrence time). This cluster number is critical in this step. This screening is to update the value of cluster number into all events in the input earthquake catalog. This step starts with screening the events with time window T from the first event of the catalog and girding the catalog spatially with a two-dimensional cell size of $S°$ x $S°$. After dividing the spatial distribution into multiple cells, the cell location of the screening events could be identified, and the program will select the events which are in the same or neighboring cells with respect to the first event of the screening events. The input earthquake catalog will be divided into two sub-catalogs, one is the selecting events and the other is remaining events. Next, the program will examine the cluster numbers of selecting events and try to update the cluster numbers. Three possible cases of updating cluster numbers are presented in the following contents:

Case 1 (Figure 2.2a): if the cluster number of selecting events equals to the initial number ($n_c = 0$), the program will update the cluster number with $n_c' = n_c'' + 1$ in to all selecting events, n_c'' indicates the minimum non-zero value of n in remaining events (except one condition when $n_c = 0$ in all remaining events, $n_c'' = 0$).

Case 2 (Figure 2.2b): if the cluster number of selecting events had been updated in the previous screening, the program will compare the size of cluster number in selecting events and choose the smallest cluster number and update that number into all selecting events.

Case 3: if the cluster number inside the selecting events are the same and not the initial number, the program will pass this run of the screening and shift to the next run.

After the screening process is finished, which means that all of the earthquakes in the catalog are updated and re-labeled their cluster numbers, we divide the input catalog into two groups based on how many earthquakes are sharing same cluster number. The input catalog will be divided into (1) spatial cluster (a cluster number shared with multiple earthquakes) and (2) spatially independent event (a cluster number only owned by one earthquake). The spatial cluster represents a relatively dense seismicity area in periods, which include all kinds of clustered seismicity.

Figure 2.3 shows an example of selected spatial independent events (black open circle) and spatial clusters (colored open circle) of earthquakes occurred shallower than 20 km in the western part of Hokuriku region, Japan, where five $M \geq 6.5$ mainshocks and one large swarm sequence occurred during the period of 1998-2016. Note that in the figure we only show the spatial clusters that include the number of earthquakes larger than or equal to 20. Based on the temporal distribution of Mc (minimum magnitude of catalog completeness) (Figure 2.4), here we used cutoff magnitude 2.0 for the input earthquake catalog. The parameters used for this example are $S = 0.05°$ and $T = 64$ days. Distribution of spatial clusters shows that those clusters are often related to large mainshocks, while some spatial clusters are not associated

with any particular large mainshock could be a swarm sequence. Besides the spatial clusters, the first order of background seismicity also can be identified. It is clear that there exists high background seismicity in the southern part of the study area. Based on their temporal distribution, spatial clusters can be characterized with: (1) Spatial cluster with a relatively large event and daily seismicity rate decayed with time since the mainshock (Figure 2.5a). (2) Spatial cluster without any relatively large event and seismicity rate followed by the largest shock do not have a clear temporal rate decay (Figure 2.5b). (3) A cluster with very few events. As a consequence of using two parameters for identifying spatial clusters, the size of the spatial clusters is dominated by the size of *S* and *T*. For instance, the size of the high background seismicity area would be significantly reduced if we choose a large *S* or *T*. It is thus evident that the choice of *S* and *T* becomes important. We will address this topic in section 2.2.

2.1.2 Step 2 : Identifying the temporal sequence in a spatial cluster

The next step is to find the enhanced seismicity sequence in each spatial cluster chosen from step 1. This step is indeed a modified version of the CURATE analysis. We keep the concept of the CURATE but uniquely incorporated an automatically determined temporal threshold values into the CURATE analysis to quantify the temporal relationship between two subsequent earthquake events. Such automatically determined temporal threshold value can be represented as the background level at a temporal location of each event. By comparing an inter-event time to the threshold background time interval, it provides a general statement that interaction between two events occurs when the inter-event time between two events is shorter than the background threshold at that time. This is one of the advantages in our analysis without any additional assumptions. However, the challenge is how to assign a proper temporal threshold rate (inter-event time) to represent time-dependent background level.

The CURATE analysis, as we introduced before, use a mean inter-event time (1/mean rate) as the background level to quantify the temporal dependency, which yields

$$\bar{T} = \frac{t_e - t_1}{e - 1}, \tag{2.1}$$

where t_e indicates the occurrence time of the last event and t_1 indicates the occurrence time of the first event. However, it requires multiple runs in residual to select the enhanced rate sequences completely, and it also requires additional parameters to combine those selected sequences. To overcome the flaw of the CURATE analysis, other automatically determined temporal parameters are introduced. First, we describe the evolution of inter-event time in a spatial cluster. Figures 2.6a and b show the temporal change in inter-event times in the mainshock-aftershock and swarm like sequences, respectively. For mainshock-aftershock type (Figure 2.6a, corresponding to Figure 2.5a), the time evolution of inter-event times in mainshock-aftershock cluster indicates an overall trend that inter-event times rapidly shortened immediately after the mainshock and gradually increased with time. For swarm type (Figure 2.6b, corresponding to Figure 2.5b), even though the inter-event time is small during the whole period, a gentle trend that inter-event times have gradually increased with time is also identified. Regarding cluster types, both inter-event times become gradually longer started from the first event to the end, while the increased amplitude seems larger and sharper in the one with a significant mainshock. Thus, a proper temporal

threshold can be set to be (1) representing as the time-dependent background level and (2) selecting enhanced seismicity rate sequence without additional parameters. The task here is how to asses this automatically determined temporal parameters that fulfill the above requirements.

We first focus on a time-dependent parameter which we call "forward mean inter-event time", which is the mean inter-event time before a target event. In a spatial cluster containing e events (i = 1,2,3,….e), for every i_{th} event, forward mean inter-event time $\overline{T_f}$ can be described as :

$$\overline{T_{f\text{i}}} = \frac{t_i - t_1}{i - 1}, \tag{2.2}$$

where t_i indicates the occurrence time of the i_{th} event. Figure 2.7 shows the schematic plot for this process. Comparing equation (2.2) with equation (2.1), the difference between the CURATE analysis and our forward mean rate analysis is that $\overline{T_{fi}}$ varies with time. Similar to the CURATE analysis, we now define two sequential events (event i, event i+1) are temporally related if their inter-event time ($\Delta t = t_{i+1} - t_i$) is shorter than the forward mean inter-event time ($\overline{T_{fi}}$) at that time. For an earthquake which is not related to any of the events will be defined as the temporally independent event and will combine with the other spatially independent events as background seismicity. Figure 2.8 shows the comparison between the temporal change of observed inter-event time (Δt) and forward mean inter-event time ($\overline{T_{fi}}$). Figure 2.8a and 2.8c show the temporal change of Δt in mainshock-aftershock sequence and swarm like sequence, respectively. Figures 2.8b and 2.8d show the temporal change of $\overline{T_f}$ in mainshock-aftershock sequence and swarm like sequence, respectively. Temporal change of $\overline{T_f}$ indicates that the value of $\overline{T_f}$ is shorter during the seismicity enhanced period and longer in a relatively dormant period.

We expected this time-dependent rate parameter would be more suitable to quantify the temporal dependency on the seismic data. But surprisingly, the results of background seismicity adopted with $\overline{T_{fi}}$ performed poorly. Figures 2.9 show the comparison of the spatial cluster (Figures 2.9a and 2.9c for mainshock-aftershock sequence swam sequence, respectively) and background seismicity adopting forward mean inter-event time (Figures 2.9b and 2.9d for mainshock-aftershock sequence swam sequence, respectively). Regardless of types of the spatial cluster, declustered earthquakes were caught as background seismicity with forward mean inter-event time. It may suggest the forward mean inter-event time approach failed to select aftershock sequences. We found that this $\overline{T_{fi}}$ performs worst when aftershock decay is fast. During a rapid aftershock decay period, most of the events are concentrated in a relatively short amount of time, and it will indeed result in a very low value of $\overline{T_f}$, even lower than mean inter-event time. It leads to raising the threshold to identify temporal clusters.

In order to overcome the insufficiency of $\overline{T_f}$, we then introduce an alternative approach, which is the backward rate analysis ($\overline{T_b}$) formulated as

$$\overline{T_{b\text{i}}} = \frac{t_e - t_i}{e - i}, \tag{2.3}$$

where t_i, and t_e represent the occurrence time of i_{th} and the last event (e_{th}) of a spatial cluster, respectively. Figure 2.10 shows the schematic plot for the criterion. Equation (2.3) is the flipped version of the equation (2.2), which we call it "backward mean inter-event time analysis". This analysis, on the contrary to $\overline{T_f}$, $\overline{T_b}$ represents a background level estimated by the time difference from the last event of the cluster. Two successive events are defined as a temporal sequence if the inter-event time ($\Delta t = t_{i+1} - t_i$) is

shorter than the backward mean inter-event time ($\overline{T_{bi}}$) at that time. Figure 2.11 demonstrates a time series of backward mean inter-event time. Time series of $\overline{T_b}$ seems to fit the observed data well. According to equation (2.3), $\overline{T_b}$ is estimated by the reciprocal of seismicity rate after an event. The value of $\overline{T_b}$ would be sensitive to the decay of aftershock rate. If we use this backward rate analysis to select the temporal clusters, any enhanced seismicity rate sequence would be selected in one run (Figure 2.12, See also Figure 2.9 for comparison). More importantly, there is no need to set up any extra parameter to link those temporal sequences like the CURATE approach. So far, we cannot explain any physics why this backward rate analysis works better than CURATE and forward rate analysis. When a relatively larger event (mainshock) occurs, the lengths of the inter-event times for the following events gradually become longer with time after the mainshock.

We tested those three different thresholds for the spatial clusters and found that the background seismicity estimated from the backward mean inter-event time fulfilled the requirement that we need. We then decided to use the backward rate analysis to find the enhanced seismicity rate sequences. Spatial clusters adopted the backward rate analysis would be divided into two groups, temporally independent event, and temporally related sequences. The temporally related sequences are regarded as spatiotemporal sequences, whereas the temporally independent events are combined with the spatially independent events collected at step 1 and then go into the background seismicity (Figure 2.1).

2.2 Parameter dependency

This algorithm adopts two parameters to identify spatiotemporal sequences. Because the size of spatial cluster directly affects the size of the spatiotemporal sequences, the size of the spatial cluster plays a key role in this algorithm. We test this algorithm in the western part of Hokuriku region in Japan (Figure 2.3) with the different range of S (range from 0.01 to 0.1° with increment by 0.01°) and T (range from 20 to 210 with common ratio of 2). This test area includes six M ≥ 6.5 mainshocks (2004/10/23 M6.8 Niigata-Chuetsu earthquake, 2007/03/25 M6.9 Noto earthquake, 2007/07/16 M6.8 Chuetsu-Oki earthquake, 2011/03/12 M6.7 north-Nagano earthquake and 2014/11/22 M6.7 Nagano earthquake) and a large swarm sequence occurred under the Hida Mountains starting from 1998/08/07. Table 2.1 indicates the ratio of background seismicity to the input catalog. The number of background events decreases as the values of S and T increase. Comparison of the cumulative number of input earthquakes with the cumulative number of background events with different T and S is shown in Figure 2.13a, b, and c, respectively. Here we demonstrate an example of $S = 0.04°$ with various T values, and $T = 256$ days with various S values. From a visual inspection of background seismicity rate in the figures, background seismicity rate changes at the occurrence time of M ≥ 6.5 mainshocks in smaller S and T settings, and stays stable (Poissonian) with larger S and T values. Following a fundamental assumption that background seismicity rate should not change with time, the results should be approved with large S and T settings. However, we need to be careful of over-declustering process. Statistically, it is easy to have a Poisson distribution when a significant amount of data is removed. From the viewpoint of earthquake hazard estimation, if too many earthquakes are removed from the catalog, the number of forecasted aftershocks thus the rate of future mainshocks will be underestimated. Therefore, we need additional way to automatically find a proper combination for S and T to maximize the number of background events

keeping the Poisson distribution in the time series.

In order to find a proper combination of S and T values, we then adopt a variety of parameter sets used in step 1, with S from 0.01° to 0.1° and T from 1 day to 1024 days, which provides us 10x11 different results. For searching the best parameter from all the combinations, we develop a parameter filtering process. A schematic plot of the filtering process is shown in Figure 2.14, two sub-processes are included and are designed to search the proper parameter set from a variety of parameter sets.

2.2.1 Over-declustering assessment

Figures 2.13b and 2.13c display examples of resulted background seismicity which appears to nearly follow Poissonian behavior with larger S and T values. However, it might be a wrong judgment due to over-declustering. Thus, we first focus on excluding the parameters that result in over-declustering. In our new algorithm, one possible condition for over-declustering is associated with over-clustering, which stands for broad spatial coverage of a spatial cluster. When the areal coverage of a spatial cluster is large, a small number of the spatially independent events will be identified, which leads to reduce the total number of background events. Large areal coverage of spatial cluster also results in large spatial coverage of spatiotemporal sequence, which increases the risk of over-declustering. Figures 2.15a and 2.15b indicate spatial distribution of identifying spatial clusters with T = 64, and 1024 days, respectively. S is fixed at 0.04° in both analyses. In Figure 2.13b, the temporal change of seismicity is negligible in both T settings, but the spatial distribution of spatial clusters in T = 1024 days clearly shows over-clustering. Comparing Figure 2.15a with Figure 2.15b, each M ≥ 6.5 mainshock-aftershock rupture area, could be distinct in the case of T = 64 days. Instead, in the case of T = 1024 days, one spatial cluster embraces a wide mainshock-aftershock area. Figure 2.16a and Figure 2.17a indicate mapviews of two different spatial clusters that both include the 2004 M6.8 Niigata-Chuetsu earthquake from a fixed S = 0.04° and T = 64, and 1024 days, respectively. Spatial distribution of spatial clusters in smaller T clearly portrays the aftershock rupture area, while larger T setting, excepts for the 2004 M6.8 rupture area, there is also the 2007 M 6.9 Chuetsu-oki earthquake inside the cluster, which has a huge potential of over-clustering.

To exclude the over-clustering parameter sets, we here design another spatial distribution analysis. This analysis is to exclude the possible parameter sets that lead to over-clustering for the spatial cluster. It examines the relationship between the distance of multiple sub-spatial clusters and the spatial coverage of input earthquake catalog. First, we estimate the areal coverage of a spatial cluster, which is the distance between earthquakes and a reference location. The reference location is given by the mean location of earthquakes (α_x,α_y) in a spatial cluster which contained n events (i = 1,2,3,….n) corresponding to the epicenter of (x_i,y_i) :

$$\begin{cases} \alpha_x = \frac{1}{n}\sum_{i=1}^{n} x_i \\ \alpha_y = \frac{1}{n}\sum_{i=1}^{n} y_i \end{cases} . \quad (2.4)$$

Figure 2.16b and Figure 2.17b show the histogram of distances between earthquakes and mean location in a spatial cluster corresponding to Figure 2.16a and Figure 2.17a, respectively. Bin width is set to be 1 km. For a spatial cluster that earthquakes occurred concentrated in one area, the histogram shows a distribution similar to a normal distribution (Figure 2.16b), a typical bell-shape with a significant peak. On the contrary, for a spatial cluster that contained multiple dense seismicity areas, the histogram shows multimodal distribution (Figure 2.17b), and the number of significant peaks can roughly correspond to the number of dense seismicity areas. To avoid the "plateau" in the multimodal distribution that prevents from defining a significant peak, we then smooth the distribution by a following kernel density function

$$f_x(x) = \frac{1}{dh}\sum_{i=1}^{d} K\left(\frac{x - x_i}{h}\right), \quad (2.5)$$

where d indicates the number of samples and h indicates the kernel bandwidth. Note that we use the kernel bandwidth equals to 10% of the grid size (0.1 x S, km). The kernel density of two examples is shown in Figure 2.16c and Figure 2.17c. Like the histogram plot, the number of peaks could correspond to the number of sub-spatial clusters. Those peaks are automatically identified by each data sample that has a larger value than its two neighboring samples. The distances between peaks also can be presented as the distances between sub-spatial clusters. Multiple peaks are likely appeared when earthquakes in a spatial cluster occurred disconnected in space (Figure 2.17a). If a spatial cluster that contained several sub-spatial clusters, the maximum distance of peaks can represent as the length of spatial coverage of a spatial cluster. We then use the size of the spatial coverage to judge if a spatial cluster is over-declustering. Instead of using the earthquake magnitude to define the maximum spatial coverage of a spatial cluster, we defined a threshold (Dm) that is proportional to the study area, which yields

$$Dm = A^{0.5} \times C , \quad (2.6)$$

where A indicates a rectangle area (km^2) of input catalog and C represents a non-dimension weighting parameter corresponding to the size of the threshold (Dm). For a spatial cluster (Sc) contained multiple sub-spatial clusters (Sc_1,Sc_2,Sc_3,…Sc_n), the distance between sub-spatial clusters could be presented as ΔD_{ij} (i,j = 1,2,3…..,n). The coverage of spatial cluster can be represented by the maximum ΔD_{ij}, and if maximum $\Delta D_{ij} > Dm$, we judge the spatial cluster is over-declustered.

Using this criterion, we can rule out the first-order possible parameters that lead to over-declustering. An example is shown in Figure 2.17c, which indicates that maximum ΔD (70.8 km) is over Dm (Dm = 32.2 km) in T = 1024 days when we set C = 0.1, thus the case of T = 1024 will be eliminated from the process. Note that the parameter C controls the size of Dm. Here we set C ranging from 0.1 to 1. If no parameter passes through the first process, the program will increase the value of C by 0.01. However, aftershocks occurred concentrating on one side of the rupture zone, the histogram of distance between the mean location will be likely to have a multimodal distribution. Such situations will lead to

enlarging the value of ΔD and tends to mis-judge over-declustering. In such case, we then estimate the centroid location (C_x,C_y) of the area of spatial cluster (a, km^2) with counter clock wise boundary position (x_k,y_k) :

$$\begin{cases} C_x = \dfrac{1}{6a}\displaystyle\sum_{i=1}^{k}(x_{k-1}+x_k)(x_{k-1}y_k - x_k y_{k-1}) \\ C_y = \dfrac{1}{6a}\displaystyle\sum_{i=1}^{k}(y_{k-1}+y_k)(y_{k-1}x_k - y_k x_{k-1}) \\ a = \dfrac{1}{2}\displaystyle\sum_{i=1}^{k}(x_{k-1}y_k) - (x_k y_{k-1}) \end{cases} \quad \text{[Steger, 1996].} \quad (2.7)$$

The program will first define the boundary location in a spatial cluster, by choosing an extreme value in every 0.5° intervals of coordinated (x_k,y_k), then reshaping the vector (x_k,y_k) into counter clockwise order. The program will calculate the reference location as mean location and centroid location of a spatial cluster, then compare the estimated maximum ΔD under both reference locations, and then choose a minimum one as the final ΔD.

2.2.2 Poisson behavior assessment

After excluding the possible parameter sets that cause over-clustering, we then quantify the Poisson behavior for the remaining parameters. A time series data with independent events, representing Poisson behavior, gives a perfectly straight line with a positive slope. There are several methods to estimate if a time series can be fitted with a Poisson distribution, most common and standard process is to divide a time series data by N intervals with a constant bin length, and to use Chi-square test with a null hypothesis to test if input data matched with the Poisson distribution. The standard Poisson test requires a bandwidth parameter for generating the independent intervals. But choosing a reasonable bandwidth becomes crucial.

To reduce the number of parameters, we employ another process to quantify how closely the background seismicity follows the Poisson distribution. We here adopt the CURATE criterion (equation 1.20) for estimating Poisson behavior because the CURATE criterion can demonstrate as the residual between observed and expected numbers of earthquakes calculating a mean rate. If the observation data is close to Poisson distribution, which reproduces a straight line with a positive slope, the result of CURATE at each point will be equal to zero, and the time series of CURATE would be a flat line.

An example of CURATE in different background seismicity is shown in Figure 2.18. Figure 2.18a shows cumulative number of declustered earthquakes (background seismicity) as a function of time in the cases of T = 4 and 64 days. Figure 2.18b shows the CURATE as a function of time corresponding to Figure 2.18a. Comparing Figure 2.18a with Figure 2.18b, the time series of CURATE for the case of T=64 days shows less perturbation, suggesting closer to a Poisson distribution (red line in Figures 2.18a and b). Then we can quantify the Poisson behavior by

$$\begin{cases} CURATE(i) = N(t_s, t_i) - D(t_s, t_i) \\ c = \dfrac{1}{e}\sqrt{\displaystyle\sum_{i=1}^{e}(CURATE(i)^2)} \end{cases}, \tag{2.9}$$

where i indicates the i_{th} (i = 1,2,3,……e) earthquake in the background seismicity, $N(t_s,t_i)$ indicates the observed cumulative number of earthquakes occurred at t_i, and $D(t_i\text{-}t_s)$ indicates the expected cumulative number of earthquakes with a constant mean rate of background seismicity. The advantage of adopting CURATE criterion is that there is no need to use any additional parameter. For background seismicity that may be close to a Poisson distribution, the value of c would be close to zero. For each parameter combination that passed through the first process, we then estimate c for each combination and choose the smallest c value to be the suggested best combination of the parameters. Figures 2.20a, b, and c display the comparison of spatiotemporal distributions between input catalog, background seismicity and spatiotemporal clusters on the western Hokuriku region with a suggested combination of the parameter set of S = 0.02° and T = 512 days. A constant background rate of seismicity could be estimated by adopting this algorithm (Figure 2.20b), while the clustered seismicity is also distinct (Figure 2.20c). The background seismicity looks also homogeneous in spatial domain, while earthquakes occurred closely in space and time in visual inspection (Figure 2.20a) is taken over as the spatiotemporal clusters (Figure 2.20c). It indicates that this algorithm has a capability of selecting different types of earthquake clusters.

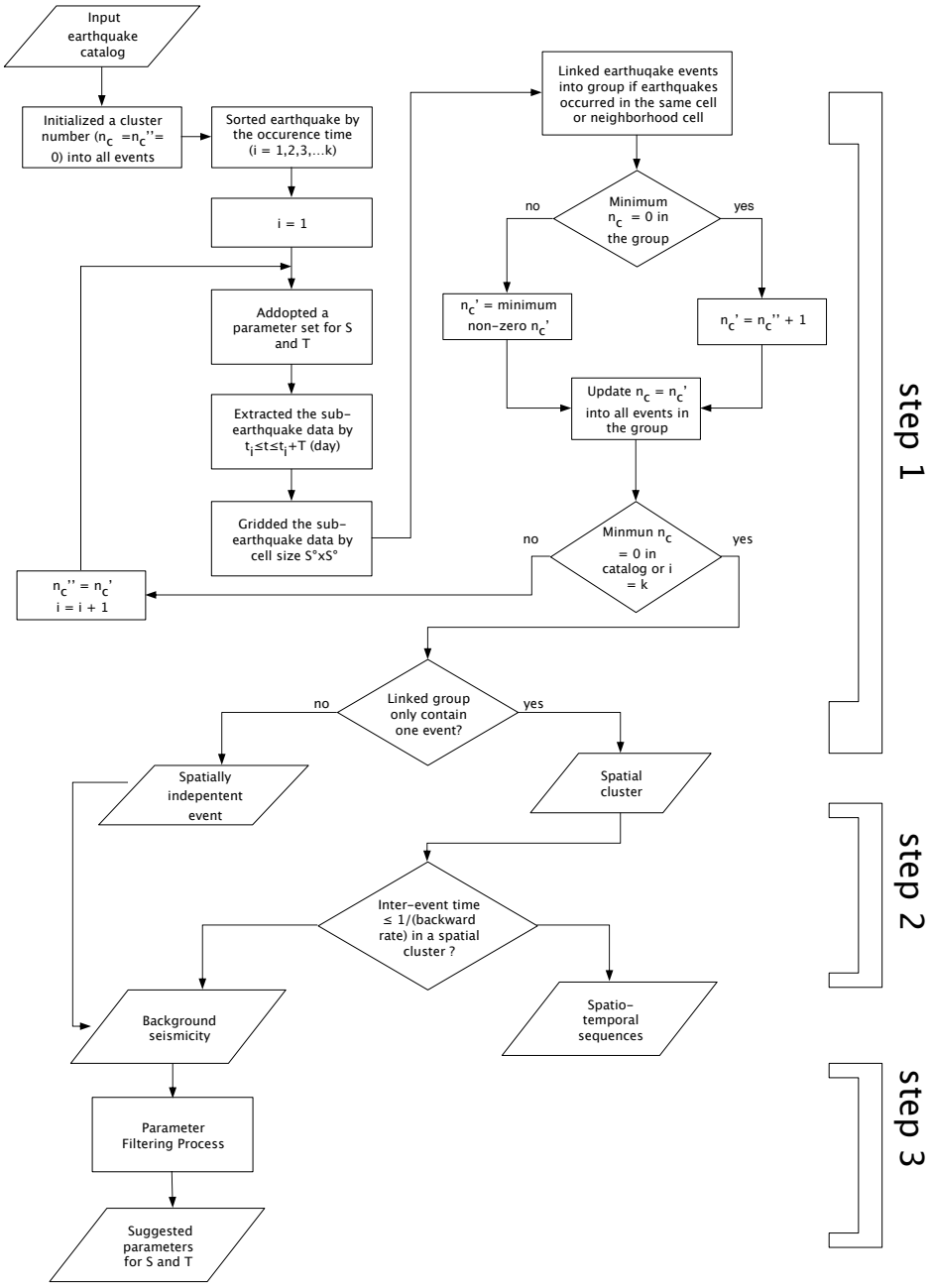

Figure 2.1 Flowchart of our newly developed algorithm.

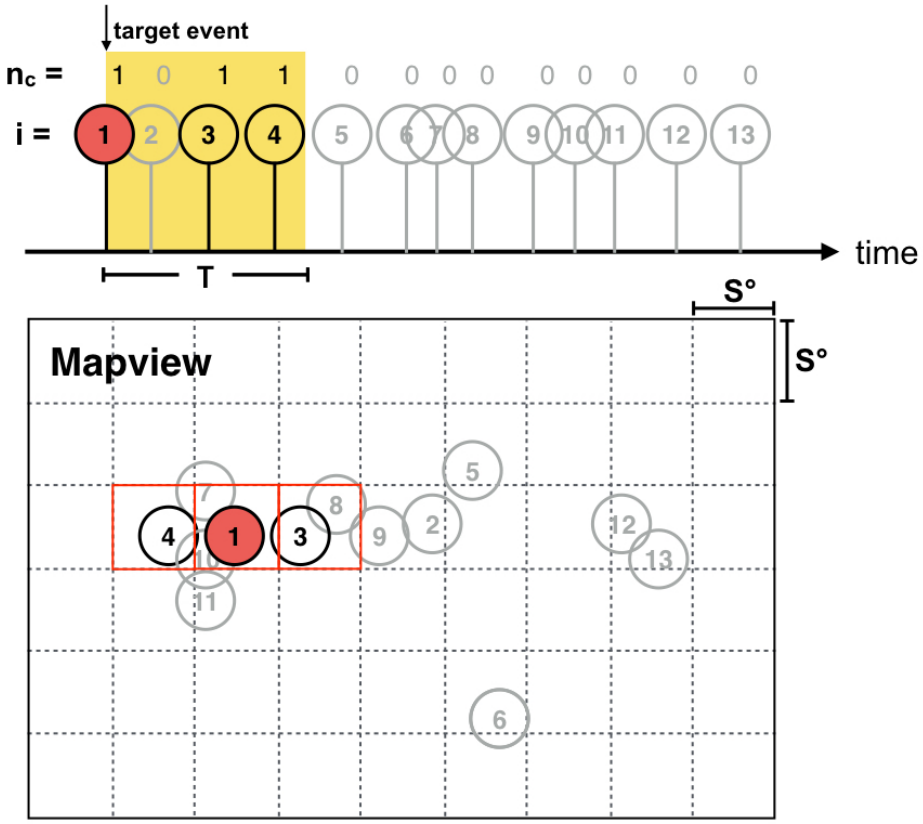

Figure 2.2a Schematic plot of case 1 of step 1. Upper and lower panels indicate time series and spatial distribution of seismicity in a spatial cluster, respectively. Back circles indicate selected events by parameter *T* (yellow box in upper panel) and *S* (cell bounded by dash lines in lower panel), and gray circles indicate remaining events. Numbers in circle indicates earthquake index *i,* and n_c indicates cluster number.

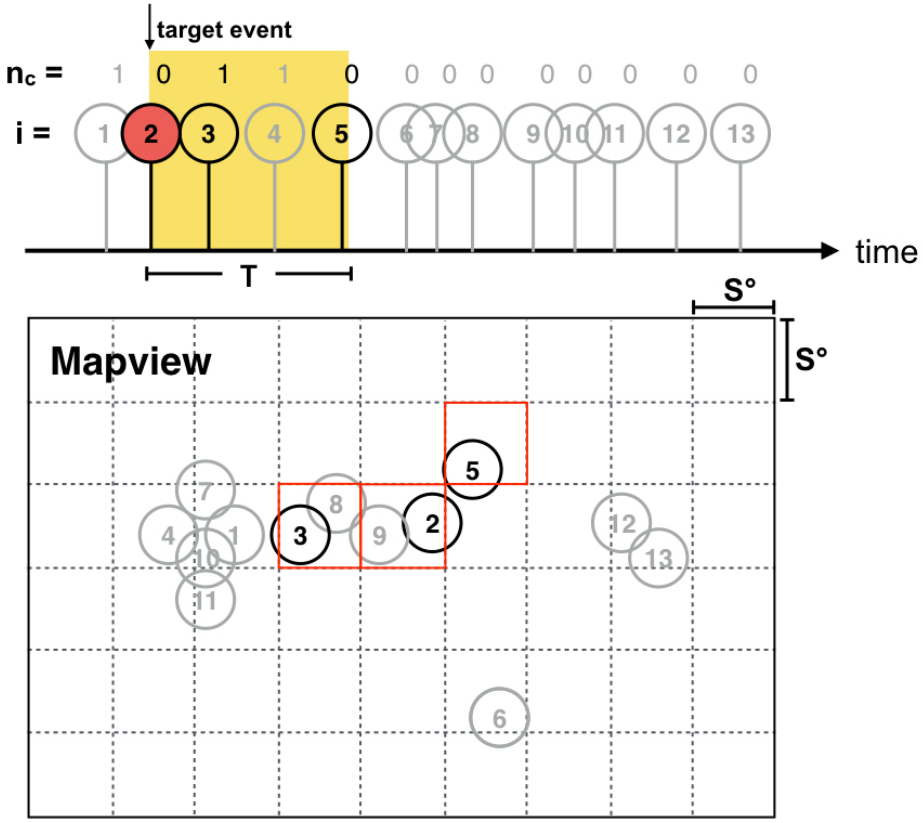

Figure 2.2b Schematic plot of case 2 of step 1. Upper and lower panels indicate time series and spatial distribution of seismicity in a spatial cluster, respectively. Back circles indicate selected events by parameter T (yellow box in upper panel) and S (cell bounded by dash lines in lower panel), and gray circles indicate remaining events. Numbers in circle indicates earthquake index i and n_c indicates cluster number. Noted that n_c'' updated from 0 to 1

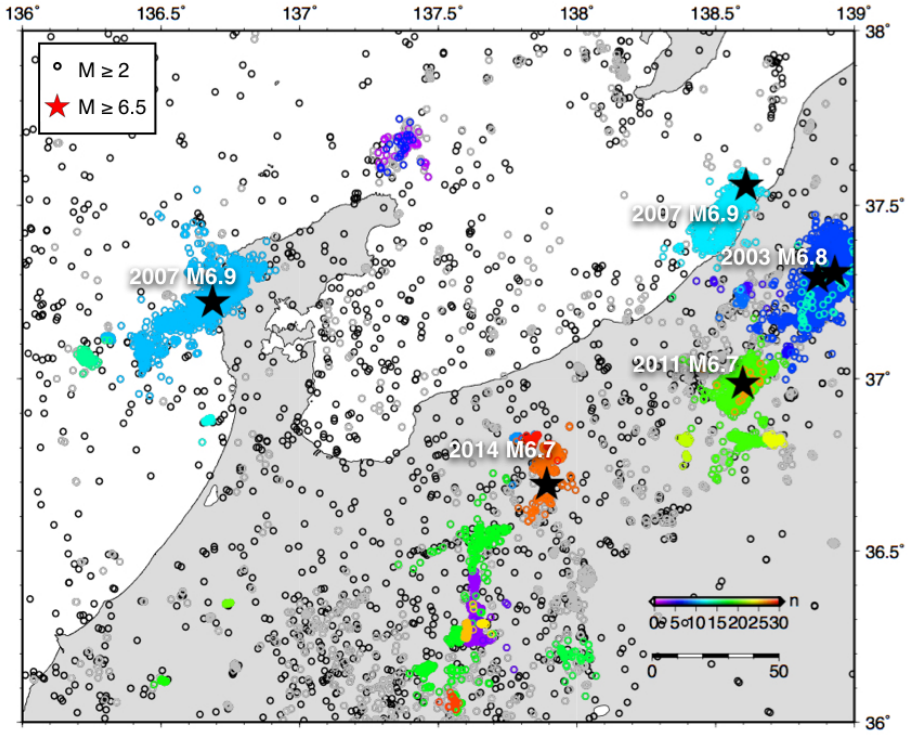

Figure 2.3 Mapview of seismicity in the western Hokuriku region, Japan. Colored circle indicates spatial cluster with the number of M ≥ 2.0 events larger than 20. Colored is coded by the cluster indices. Gray circle indicates spatial cluster events with number of events in a spatial cluster smaller than 20. Black circles are identified spatial independent events. Black star denotes M ≥ 6.5 event. Here we set $S = 0.05°$ and $T = 64$ days.

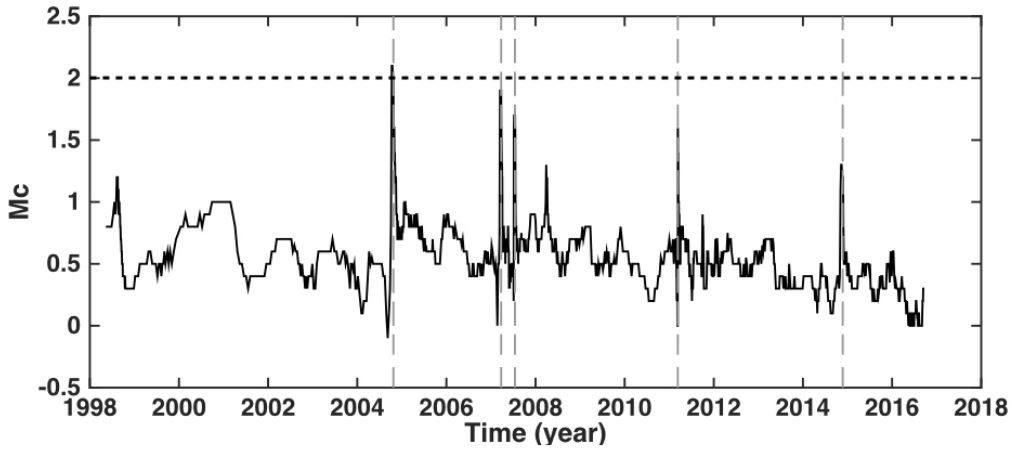

Figure 2.4 Temporal changes in *Mc* during the period of 1998/01/01-2016/09/16. *Mc* is computed by software ZMAP (Weimer, 2001). The calculation is approached by the maximum likelihood method with an equal earthquake counts of 1000, and minimum numbers of 100 earthquakes. The timing of each M ≥ 6.5 event is marked by a vertical gray dash line. The computed *Mc* values are mostly below 2.0, represented as the horizontal dash line, whereas several significant spikes of high Mc well correspond to the M ≥ 6.5 event.

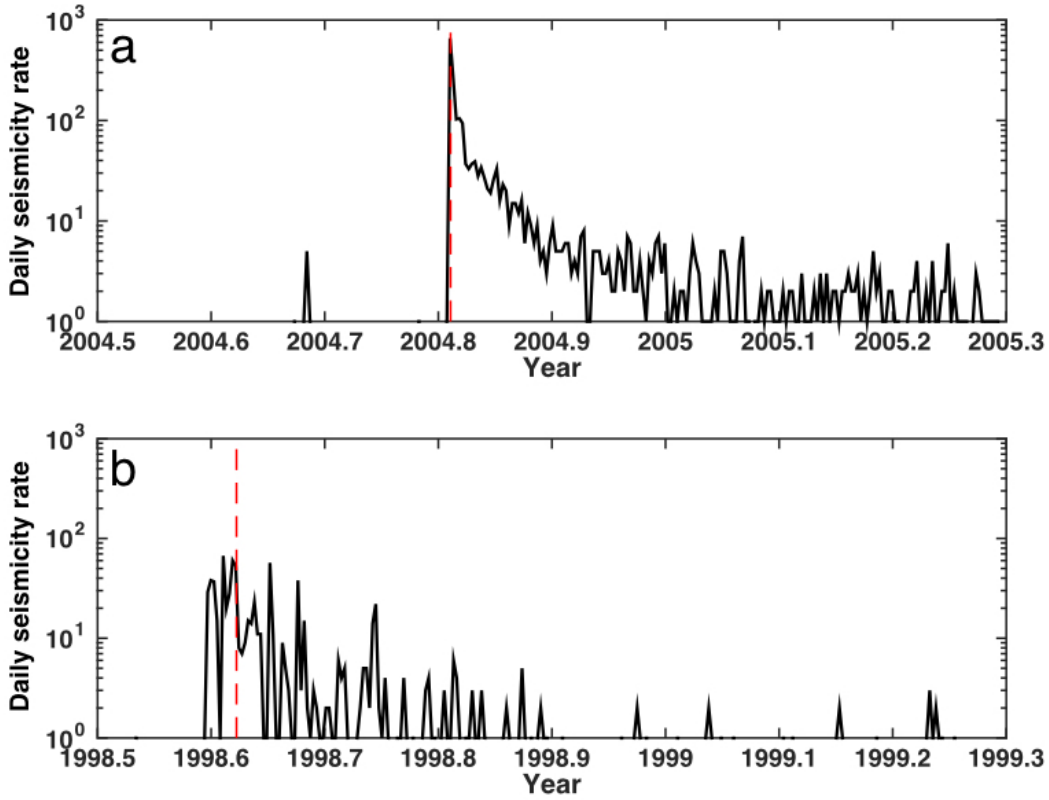

Figure 2.5 Two different types of spatial cluster based on the temporal distribution. (a) Mainshock-aftershock and (b) swarm like sequence. Horizontal axis indicates earthquake occurrence time and vertical axis indicates seismicity rate. Red dashed line denotes the occurrence time of the largest event in the spatial cluster.

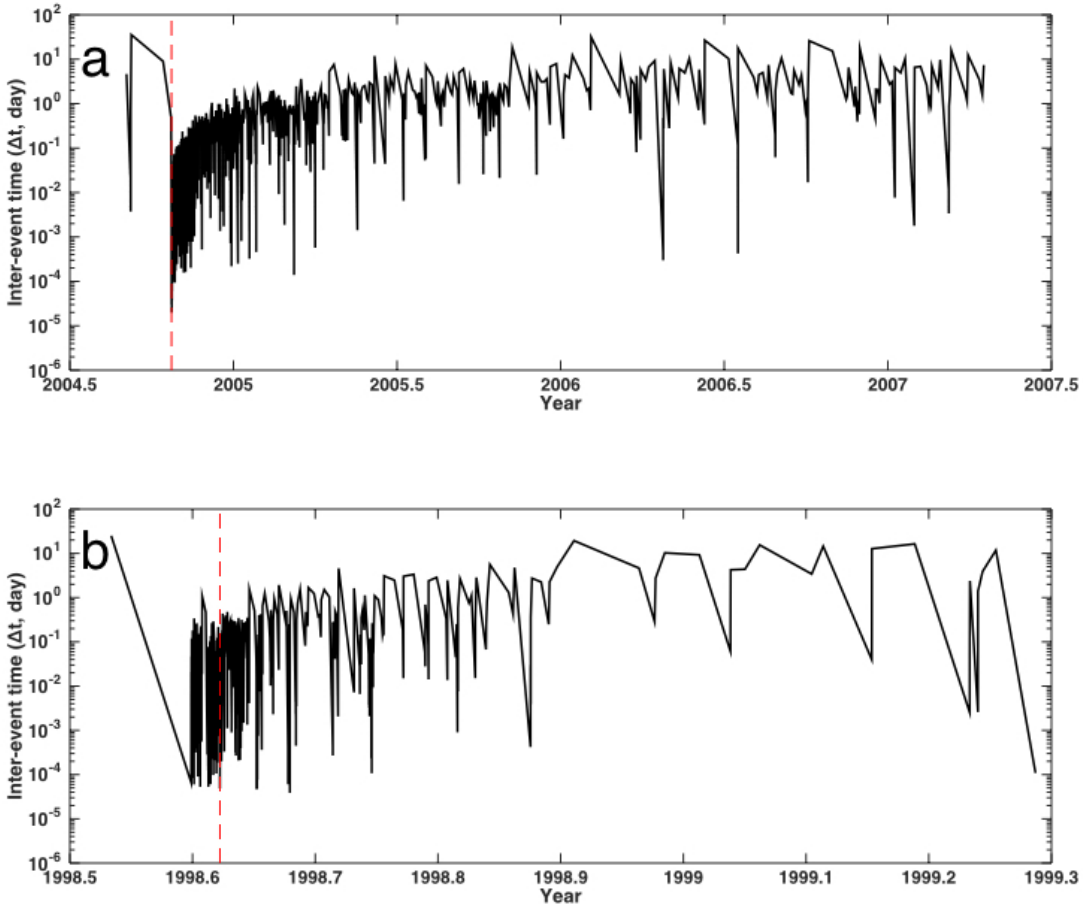

Figure 2.6 Temporal distribution of earthquake inter-event time in one spatial cluster. (a) Mainshock-aftershock and (b) swarm like sequences. The temporal distribution of seismicity corresponds to Figure 2.5. Horizontal axis is earthquake occurrence time and vertical axis is time difference between two continuous events. Red dashed line indicates the occurrence time of the largest event in the spatial cluster.

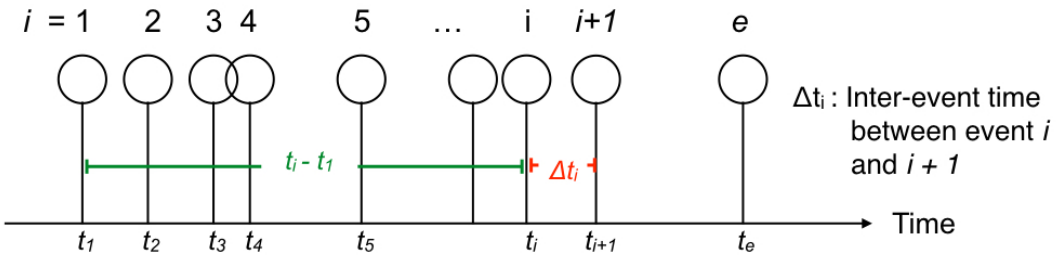

$$\overline{T_{f\mathrm{i}}} = \frac{t_i - t_1}{i - 1}, \quad t_1 < t_i < t_e$$

Figure 2.7 Schematic plot of how to calculate $\overline{T_f}$. Stem plot indicates time series of earthquakes in a spatial cluster, i indicates the earthquake index and t_i indicates that occurrence time. $\overline{T_f}$ in event i indicates the mean inter-event time before event.

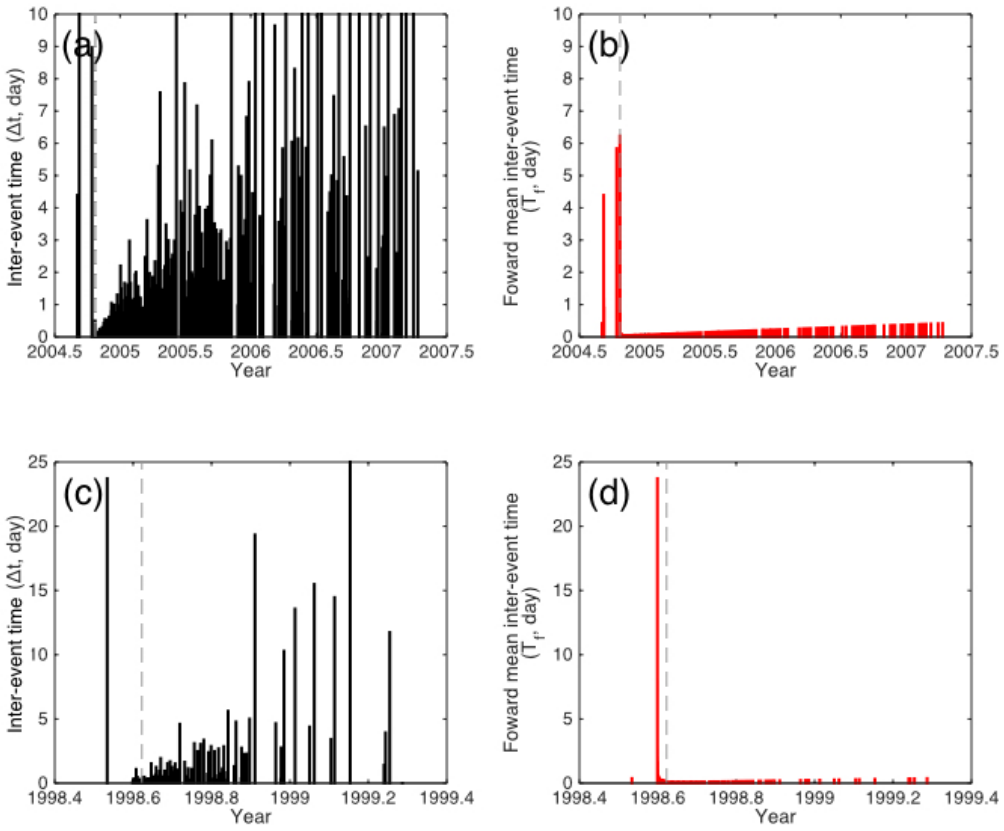

Figure 2.8 Temporal change of observed Δt and $\overline{T_f}$ in mainshock-aftershock type (a,b for Δt and $\overline{T_f}$, respectively) and swam type (c,d for Δt and $\overline{T_f}$, respectively) spatial cluster. The temporal distribution of seismicity corresponds to Figure 2.5. The Horizontal axis indicates earthquake occurrence time and vertical axis indicates the estimated forward mean inter-event time. Dashed line denotes the occurrence time of mainshock. It is clear that $\overline{T_f}$ is smaller after the mainshock and gradually increases with time.

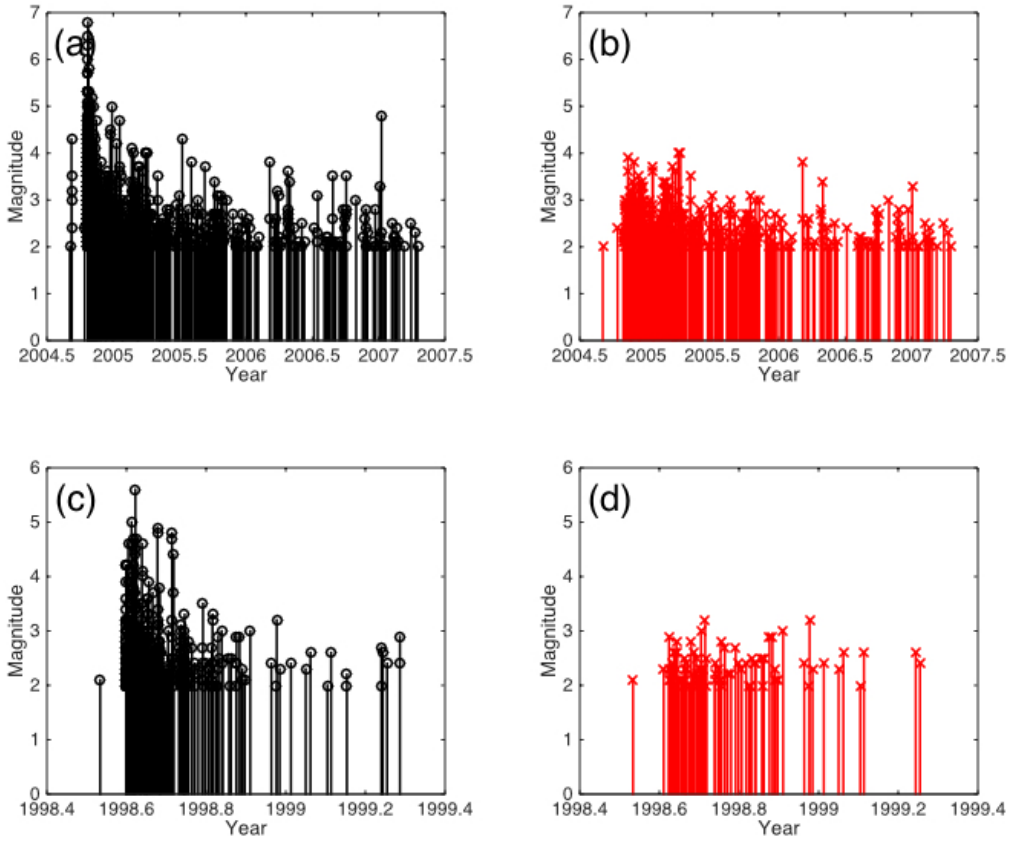

Figure 2.9 Magnitude-time plot from (a) observed mainshock-aftershock type spatial cluster, (b) identified temporally independent event, (c) observed swarm type spatial clusters and (d) identified temporally independent event. Temporally independent event is identified from equation 2.2.

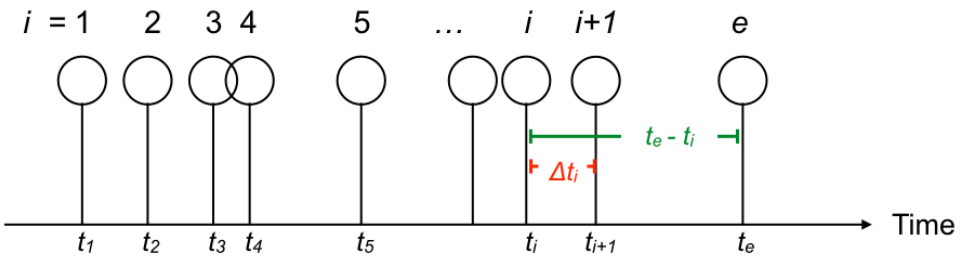

$$\overline{T_{bi}} = \frac{t_e - t_i}{e - i}, \quad t_1 < t_i < t_n$$

Figure 2.10 Schematic illustration of how to calculate $\overline{T_b}$. Stem plot indicates time series of earthquakes in a spatial cluster, i indicates the earthquake index and t_i indicates that occurrence time. $\overline{T_b}$ in event i indicates the mean inter-event time after event i.

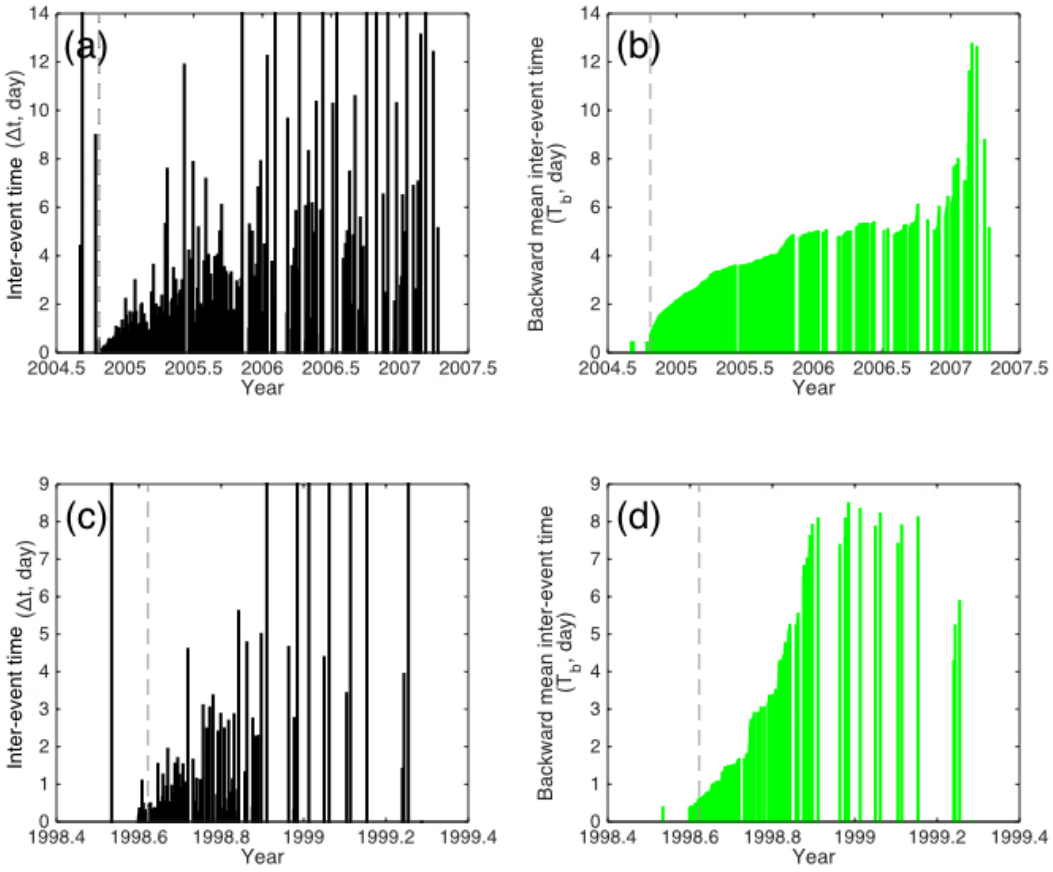

Figure 2.11 Temporal change of observed Δt and $\overline{T_b}$ in mainshock-aftershock type (a,b for Δt and $\overline{T_b}$, respectively) and swam type (c,d for Δt and $\overline{T_b}$, respectively) spatial clusters. The Horizontal axis indicates earthquake occurrence time and vertical axis indicates the estimated forward mean inter-event time. Dashed line indicates the occurrence time of mainshock.

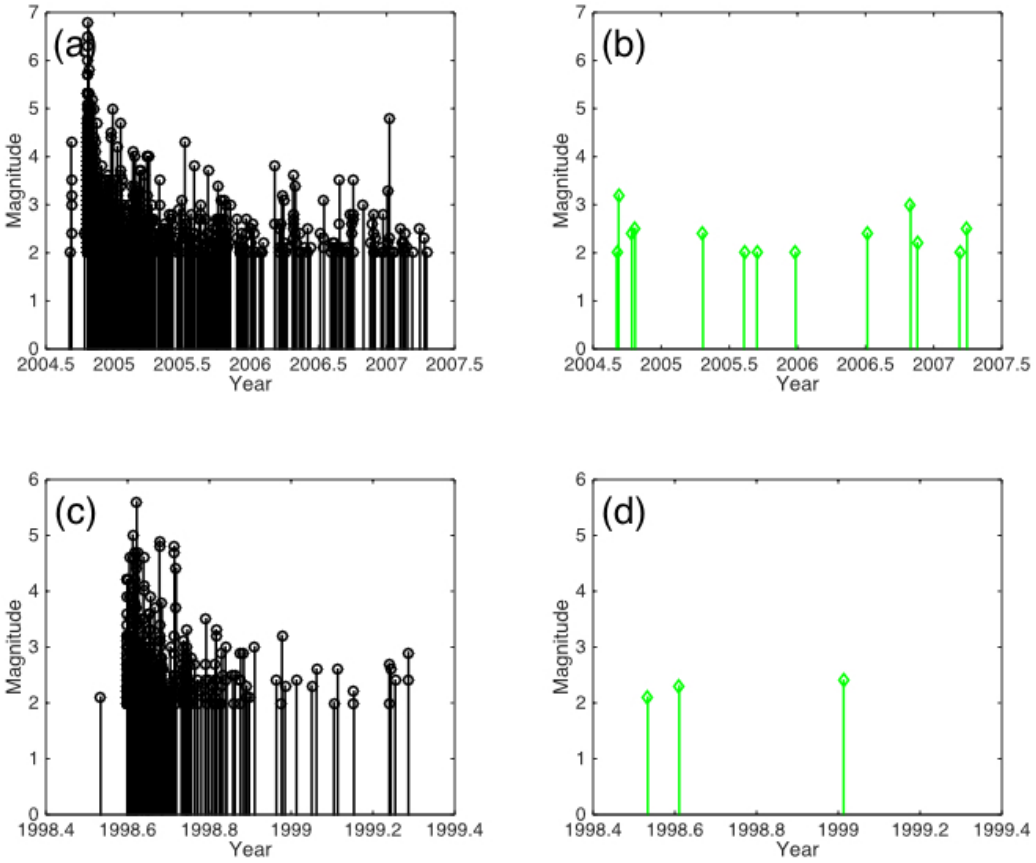

Figure 2.12 Magnitude-time plot from (a) observed mainshock-aftershock type spatial cluster, (b) identified temporally independent event, (c) observed swarm type spatial clusters and (d) identified temporally independent event. Temporally independent event is identified from equation 2.3.

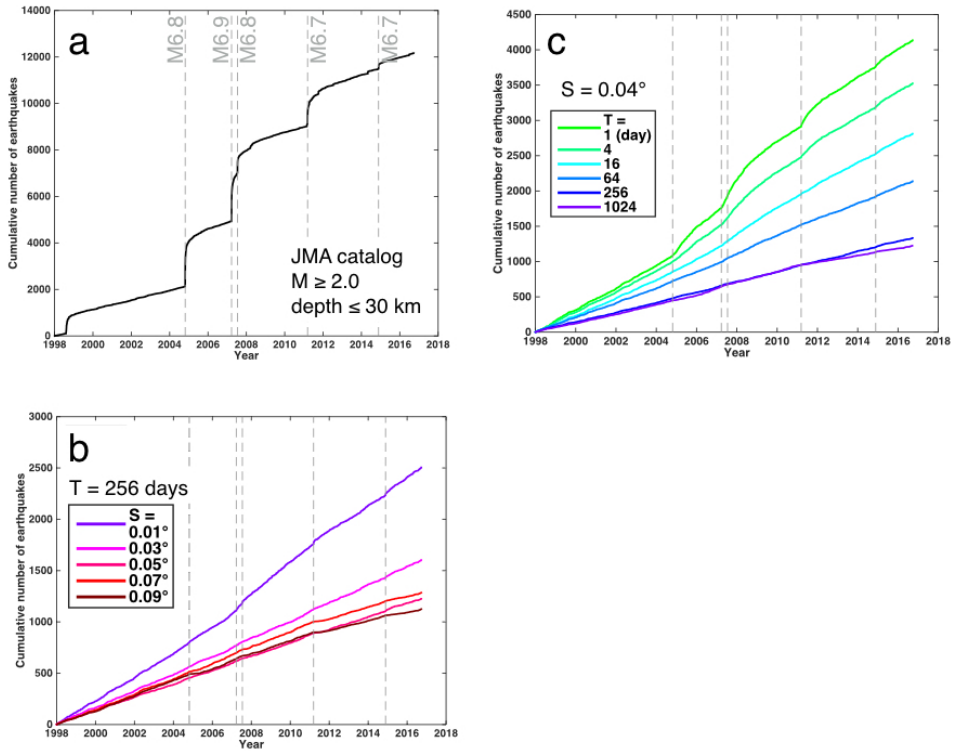

Figure 2.13 Comparison between cumulative number of raw data and cumulative number of background events with different parameter settings. (a) Raw data, (b) Fixed T = 256 days, colored is coded by different S settings and (c) Fixed S = 0.04°, colored is coded by different T settings. Dashed grey line indicates occurrence time of M ≥ 6.5 event.

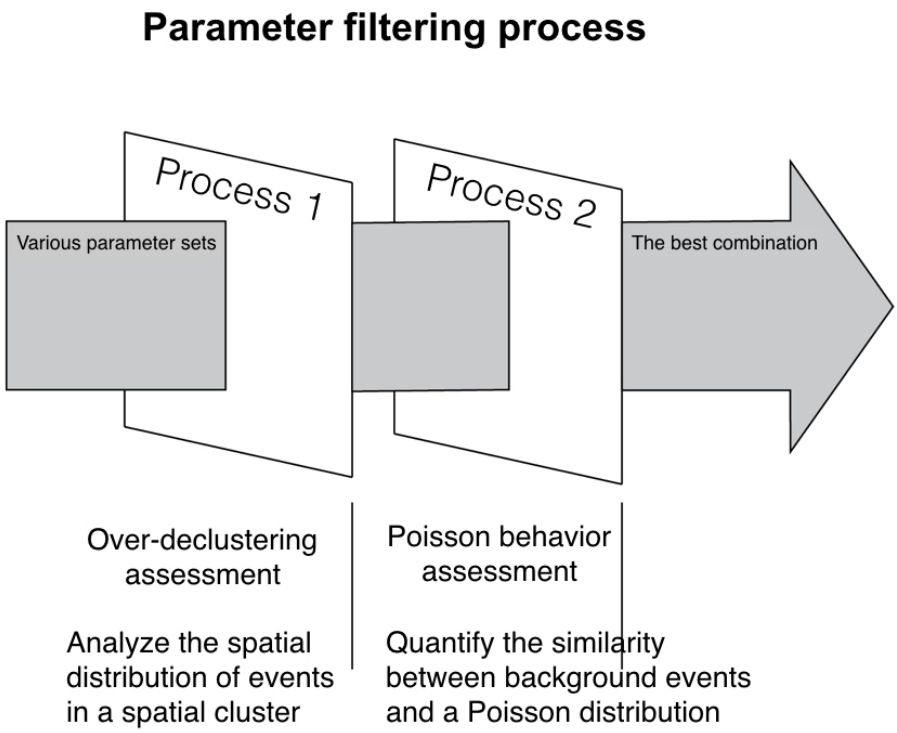

Figure 2.14 Schematic illustration for filtering process to find the best parameter combination.

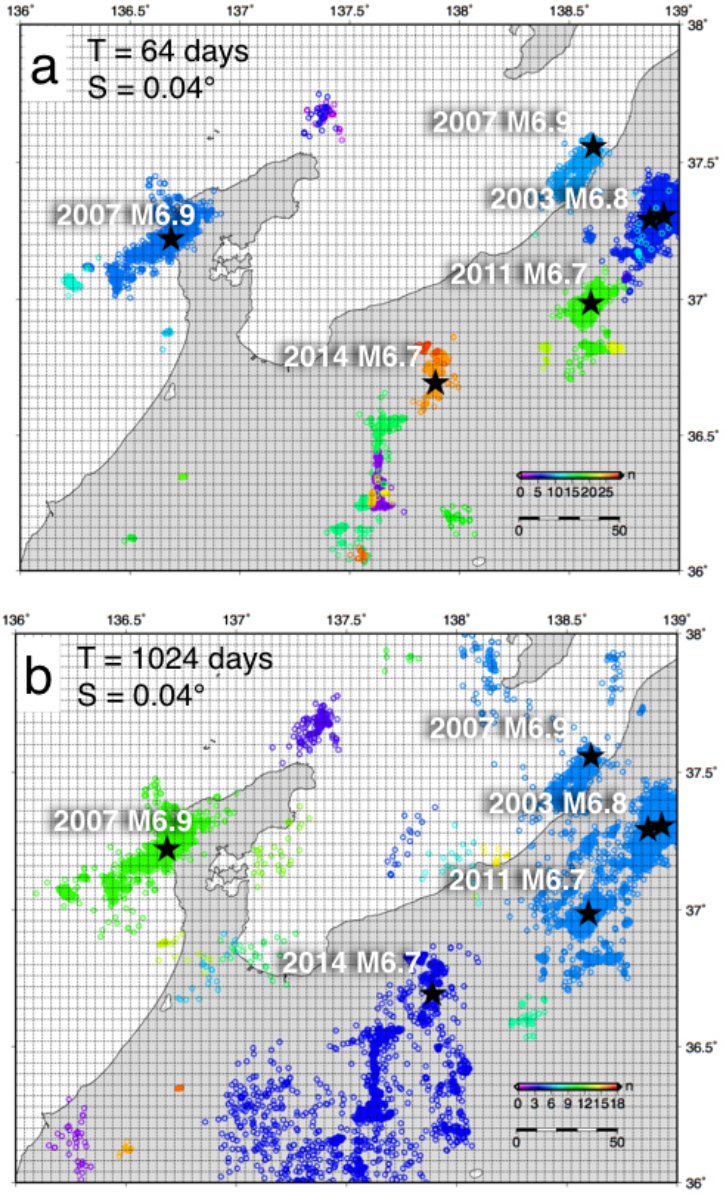

Figure 2.15 Spatial distribution of spatial cluster events with the parameter settings of (a) S = 0.04° and T = 64 days, and (b) S = 0.04° and T = 1024 days. Color circles indicate M ≥ 2 events. Color is coded by the cluster number. Black star indicates M ≥ 6.5 mainshock. Each mainshock-aftershock rupture area is well presented with smaller T.

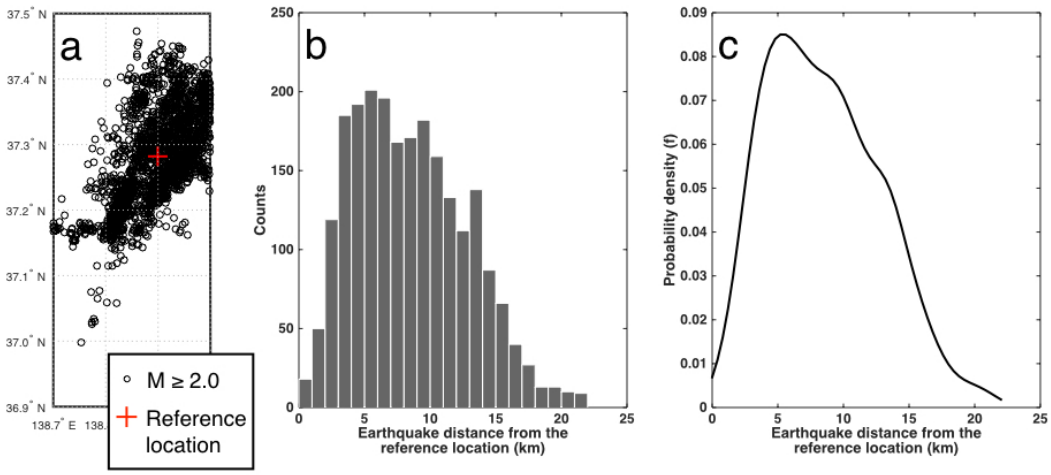

Figure 2.16 Space divergence in a spatial cluster contained the 2004 M6.8 Niigata-ken-Chuetsu earthquake with S = 0.04° and T = 64 days. (a) Spatial distribution. Black circle indicates M ≥ 2 event and red cross symbol indicates a reference location calculated by equation (2.4). (b) Histogram of distances between earthquakes and the reference location. Bin width is set to be 1 km. (c) Calculated kernel density plot by equation (2.5). Kernel bandwidth (h) is set to be 0.4 km.

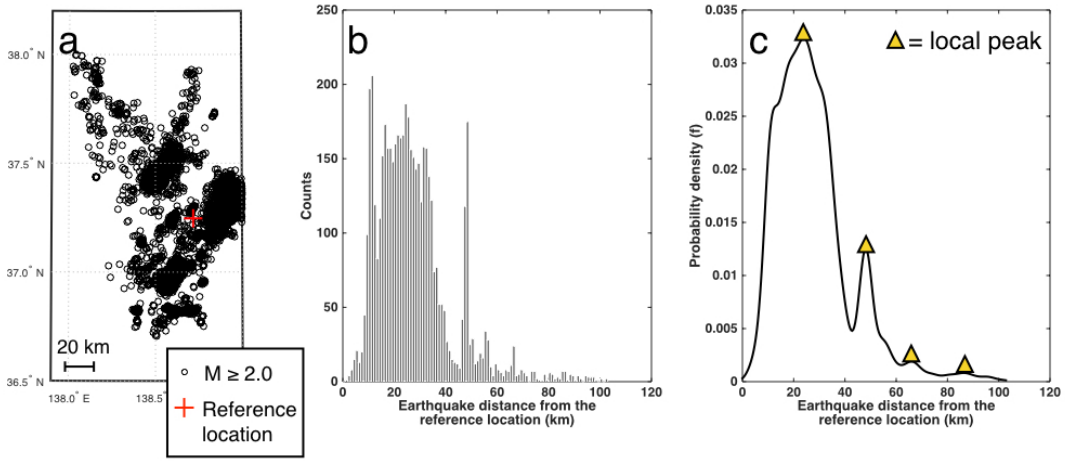

Figure 2.17 Space divergence in a spatial cluster contained 2004 M6.8 Niigata-Chuetsu earthquake with S = 0.04° and T = 1024 days. (a) Spatial distribution. Black circle indicate M ≥ 2 events and red cross symbol denotes a reference location calculated by equation (2.4). (b) Histogram of distances between earthquakes and reference location. Bin width is set to be 1 km. (c) Calculated kernel density plot by equation (2.5). Kernel bandwidth (h) is set to be 0.4 km. Yellow triangle marks local peaks (see text for details). Peaks, identified as high kernel density, are represented as sub-areas, and the distance between peaks also represents the distance between each sub-areas. Maximum distance of peaks in this case is 70.8 km.

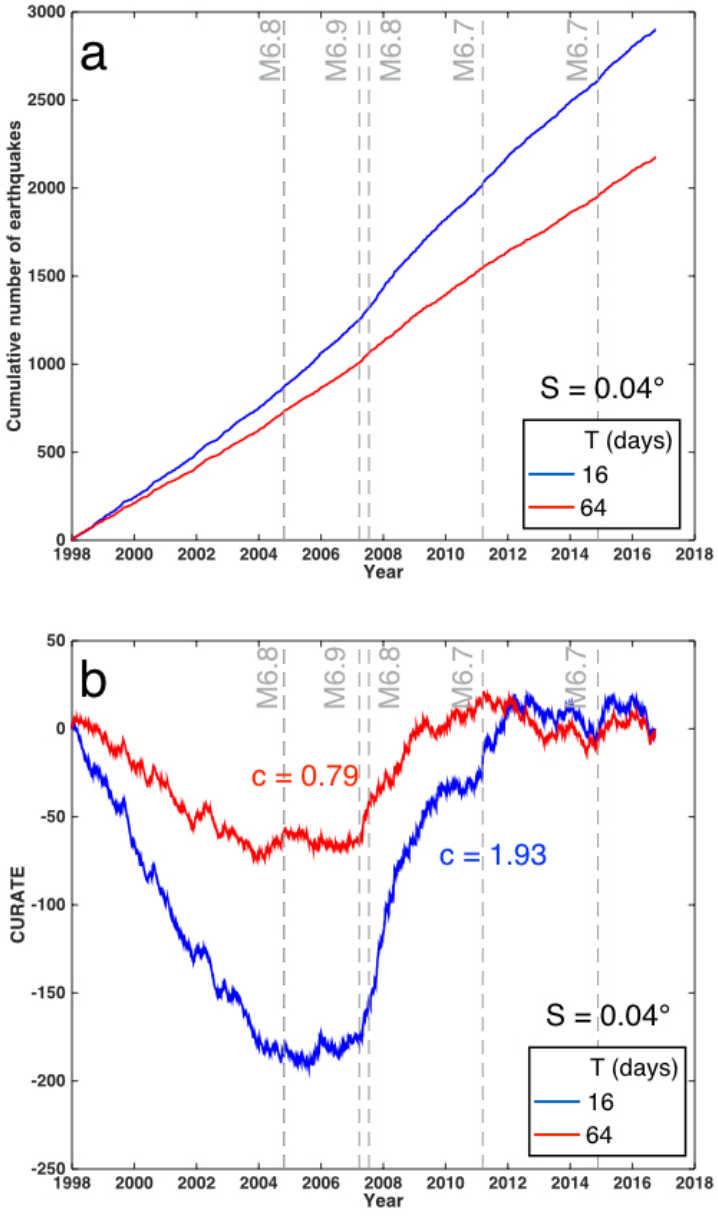

Figure 2.18 (a) Cumulative number of background seismicity with T = 16 days (blue line) and T = 64 days (red line). S is set to be 0.04°. (b) CURATE as a function of time with T = 16 days (blue line) and T = 64 days (red line). Vertical dashed grey line indicates the occurrence time of M ≥ 6.5 event. Temporal change in CURATE is sensitive to the seismicity rate change, background seismicity changes after the 2007 M6.8 event with T =16 days leads to an acceleration of CURATE, while background seismicity performed more stable with T = 64 days leads to CURATE with less perturbation. The estimated c values from equation (2.9) for T = 16 and T = 64 days are 1.93 and 0.79, respectively.

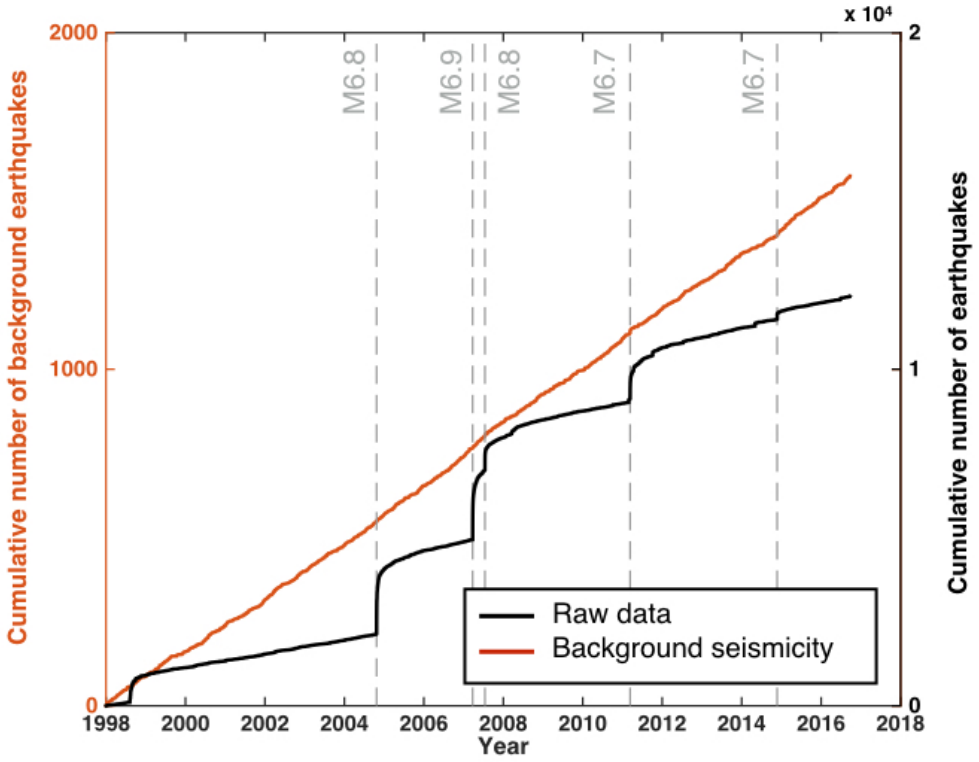

Figure 2.19 Temporal distribution of estimated background seismicity and input data. The best combination of parameters is S = 0.02° and T = 512 days. The spatial distribution of input data is shown in Figure 2.3. Back line indicates the input data, red line indicates the estimated background seismicity. Vertical grey line denotes occurrence time of M ≥ 6.5 event. A constant background seismicity rate is found by this new algorithm.

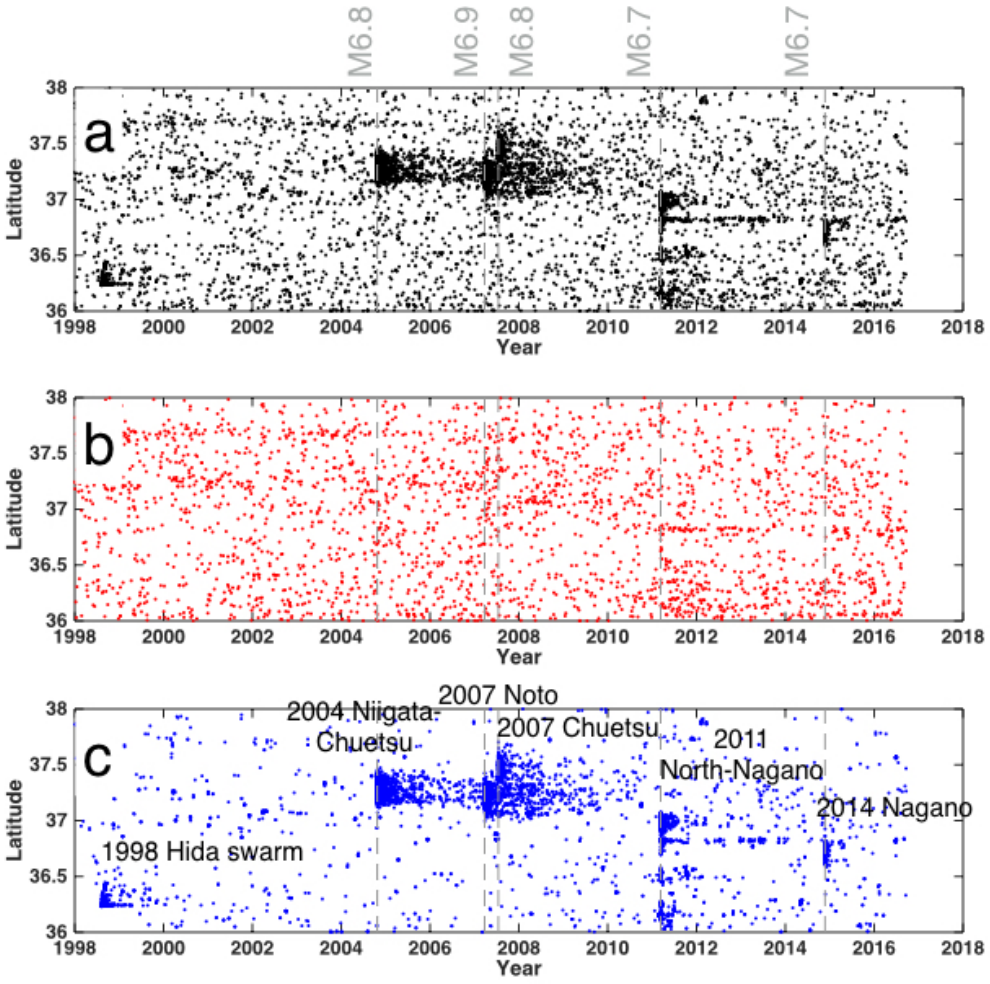

Figure 2.20 Space-time plot in the western Hokuriku region. (a) Input catalog. (b) Background seismicity. (c) Spatiotemporal seismicity. Horizontal axis represents occurrence time and vertical axis represent earthquake latitude. Dashed grey line indicates the occurrence time of M ≥ 6 event. A homogenous condition also shown on the background seismicity and this algorithm has a capability to select earthquake clusters.

Table 2.1 Ratios of the number of background events to total number of events with various parameter sets.

	S = 0.01 (°)	0.02	0.03	0.04	0.05	0.06	0.07	0.08	0.09	0.10
T = 1 (day)	0.44	0.40	0.38	0.37	0.36	0.35	0.34	0.34	0.33	0.33
2	0.40	0.37	0.35	0.33	0.33	0.32	0.31	0.31	0.30	0.30
4	0.37	0.33	0.31	0.30	0.29	0.29	0.28	0.27	0.27	0.26
8	0.34	0.30	0.28	0.27	0.26	0.25	0.24	0.24	0.23	0.22
16	0.31	0.27	0.25	0.24	0.23	0.22	0.21	0.20	0.19	0.19
32	0.28	0.24	0.22	0.21	0.19	0.18	0.17	0.16	0.15	0.14
64	0.26	0.22	0.20	0.18	0.16	0.15	0.14	0.13	0.12	0.11
128	0.23	0.19	0.17	0.14	0.13	0.11	0.10	0.10	0.10	0.11
256	0.21	0.16	0.13	0.11	0.10	0.10	0.11	0.11	0.11	0.12
512	0.18	0.13	0.11	0.11	0.11	0.11	0.11	0.12	0.12	0.12
1024	0.16	0.11	0.11	0.10	0.10	0.11	0.12	0.12	0.12	0.12

Chapter 3 Application to areas in and around the Japanese Islands

3.1 Earthquake data and completeness

Here we apply this algorithm to several areas in and around the Japanese Islands. The areas are intentionally chosen to test if this algorithm is suited for any types of seismo-tectonic environments. We use earthquakes in the JMA (Japan Meteorological Agency) catalog whose recorded time period is from 1998/01/01 to 2016/09/22. Prior to the catalog analysis, we first assess the minimum magnitude of completeness (*Mc*). *Mc* is sought from addressing a smallest magnitude threshold above which the frequency magnitude distribution follows the Gutenberg-Richter relationship [e.g., Habermann, 1983, 1987; Woessner et al., 2005; Gutenberg et al., 1944]. *Mc* also depends on area and time, is often reflected from the seismic station coverages or transient changes by mainshocks [Kagan, 2003]. To obtain a stable earthquake catalog throughout the study period, we employed a cutoff magnitude that is larger than Mc. We estimate the value of *Mc* for each selected area before running the algorithm and address its own magnitude cutoff above *Mc* for the input earthquake catalog.

3.2 Northern Kyushu region

Northern Kyushu region (Figure 3.1a) was characterized as low seismicity before the 2005 M7.3 Fukuoka-ken-seiho-oki earthquake [hereinafter Fukuoka earthquake, GSI,1987]. The hypocenter depth distribution (Figure 3.1b) indicates the down-dip limit of seismogenic layer is up to 20 km in this region. The temporal distribution of *Mc* (Figure 3.1c) by using the maximum likelihood approach [Wiemer and Wyss, 2000] shows a small constant value around 0.5 to 1 but sudden jump to 2.8 is seen after the 2005 M7 Fukuoka event. To analysis the seismicity in this region, we selected earthquakes with magnitude larger than 1 (Mcutoff = 1) and focal depth shallower than or equal to 20 km. Map view of seismicity displays three major spatial clusters occurred in this area, from southeast to northwest, corresponding to the northern flank of Mount Aso volcano and Oita area where aftershocks triggered by the 2016 M7.3 Kumamoto earthquake [Uchide et al., 2016; Miyazawa, 2016]. There are an earthquake cluster occurred in 2009 in the central area with a mainshock magnitude 4.7, and aftershocks associated with the 2005 M7.3 Fukuoka earthquake, respectively. The suggested combination of S and T for estimating background seismicity is 0.02° and 64 days.

A comparison of temporal distribution between seismicity, estimated background seismicity and spatiotemporal sequence is shown in Figure 3.2. The smoothed pattern of temporal distribution of background seismicity (Figure 3.2a) indicates that estimated background seismicity is homogenous, while temporal distributions between seismicity (Figure 3.2a) and spatiotemporal sequence (Figure 3.2c) are identical, which suggests the background earthquake productivity is extremely low. Homogenous in temporal distribution is also accompanied by homogenous spatial distribution. Figure 3.3 shows the comparison of space-time distribution between seismicity (Figure 3.3a), background seismicity (Figure 3.3b) and spatiotemporal cluster (Figure 3.3c). It is evident that earthquakes occurred closely in space and time are identified as the spatiotemporal sequences in this area.

3.3 Central Kyushu region

We selected earthquakes in a rectangle box from 32.25° N to 33.5° N, and 130° E to 131.5° E. Note that a part of the study region is overlapped by northern Kyushu region (section 3.2). Regarding regional geologic features, a large scale right-lateral shear zone (Oita–Kumamoto Tectonic Line, Yabe, 1925), running through the central part of Kyushu Island, bisects the island. The shear zone is thought to be a southwest extension of the Median Tectonic Line which extended from the Kii Peninsula through the Shikoku Island. There are several major active volcanos along the shear zone. In a recent geodetic measurement, the Oita–Kumamoto Tectonic Line has a lateral-strike slip behavior which produces strike-slip and normal faulting earthquakes [Nishimura and Hashimoto, 2006; Loveless and Meade, 2010; Matsumoto et al. 2015]. The spatial distribution of seismicity (Figure 3.4a) shows seismicity at Central Kyushu region concentrated on three areas, from southwest to northeast, corresponding to the main rupture area of 2016 Kumamoto event, the northern part of Aso volcano, and Oita, respectively. Before the 2016 Kumamoto earthquake, only one M > 5 event occurred during the study period, and volcanic type earthquakes occurred frequently. Hypocenter depth distribution provides the seismogenic layer is about 20 km (Figure 3.4b). The temporal distribution of minimum magnitude of completeness (Mc) by using the maximum likelihood approach [Wiemer and Wyss, 2000] shows a small constant value around 0.3-0.5 before the 2016 Kumamoto earthquake, but it jumped to 3 immediately after the mainshock (Figure 3.4c). The estimation of b-value by Maximum Likelihood (ML) estimation [Aki, 1965; Utsu, 1965] is 0.86±0.13 for the pre-Kumamoto earthquake period, which is lower than the average b-value (0.9-1.1). It suggests that this area is characterized by a structural and stress heterogeneity [Mogi, 1962; Mori and Abercrombie, 1997]. To analyze the aftershocks of the Kumamoto earthquake, we used magnitude cutoff, Mcutoff = 2 and hypocenter depth shallower than or equal to 20 km. The best combination of S and T is 0.01° and 256 days. Temporal distribution (Figure 3.5a) and spatial distribution of seismicity (Figure 3.5a) indicate that the seismicity is dominated by the aftershocks following the Kumamoto earthquake. Temporal distribution of estimated background seismicity indicates a general stable seismicity with a constant rate during the pre-Kumamoto earthquake period, but a sudden rate increase appeared immediately after 2016 Kumamoto earthquake (Figure 3.5b). Space-time plot of the estimated background seismicity also displays homogenous distribution during the pre-Kumamoto earthquake period. But a high density of seismicity remains after the 2016 Kumamoto earthquake (Figure 3.6b). The increased seismicity occurred on the mainshock rupture zone and the northern part of the Aso volcano (Figure 3.6b). We found that this result is due to the limitation of backward rate method. More details are discussed in section 4.1.3

3.4 Geiyo area

The 2001 Geiyo earthquake (M6.7) occurred in the Philippine Sea slab beneath the Seto Inland Sea of Japan, at a depth of 46 km. To analyze the seismicity around the mainshock, we selected earthquakes in a rectangle box from 34.5° N to 36° N and 132.5° E to 134° E (Figure 3.7a). The hypocenter depth distribution indicates that earthquakes concentrate on two depth ranges, one is shallower than 20 km which associated with the seismogenic zone in the upper crust, the other is a depth range between 30 and 60 km that represented the interplate and intra-slab seismicity in the subduction zone. (Figure 3.7b) The

temporal distribution of Mc by using the maximum likelihood approach shows a constant small *Mc* around 0.3-0.5 but sudden jump to 1 occurred immediately after the Geiyo earthquake (Figure 3.7c). To analyze the seismicity and aftershocks occurred in the Geiyo area, we used Mcutoff = 1 and hypocenter depth shallower than 60 km. The spatial distribution shows that there are two clustered sequences occurred in the surrounding area from the Geiyo mainshock even except the aftershocks of the Geiyo earthquake (Figure 3.7a). The only earthquakes associated with Geiyo mainshock are seen on the temporal distribution plot (Figure 3.8a). The best combination of parameters is $S = 0.01°$ and $T = 256$ days. A Poisson like-behavior is identified on both temporal and space-time distribution (Figure 3.8b and Figure 3.9b, respectively), it is also worth suggesting that a relatively high background seismicity is observed on the latitude between 34.2° N to 34.4° N. The temporal distribution of spatiotemporal clusters indicates that expect the 2001 Geiyo aftershocks, a slight rate increase of seismicity occurred in 1999 and 2004 (donated as arrows in Figure 3.8c) also provided, while those small increase corresponding to the dense seismic area on the space-time plot (Figure 3.9c)..

3.5 Kinki region

Kinki region is characterized by several local high rates of small earthquakes in the shallow depth (≤ 20 km). The western part of the Kii Peninsula is also marked as one of the most intensive non-volcanic high background rate of seismicity in Japan [e.g., Mizoue et al. 1983; Kato et al. 2010, 2014; Yoshida et al. 2011]. We selected earthquakes in a rectangle box from 33° N to 36° N and 134° E to 136° E, which covers the western part of the Kii Peninsula and Kinki region (Figure 3.10a). Figure 3.10b indicates the thickness of seismogenic layer is about 20 km. The temporal distribution of *Mc* shows a small value from 0 to 0.5 and a spike of 2 associated with a M5.6 mainshock occurred in the northern part of the Kinki region in 2001 (Figure 3.10c). Spatial distribution (Figure 3.10a) shows that rate of small earthquakes is high in the entire region, six M ≥ 5 events occurred during the study period. The temporal distribution also demonstrates that seismicity in this area is high, while most temporal aftershocks were brought from the 2001 M5.6 event (Figure 3.11a). The suggested best combination for *S* and *T* is $S = 0.01°$ and $T =$ 256 days. Temporal distribution of estimated background seismicity (Figure 3.12b) shows Poisson-like behavior and the space-time distribution (Figure 3.12b) is mostly homogenous. Temporal distribution (Figure 3.11c) and space-time distribution (Figure 3.12c) of spatiotemporal clusters are identical with the input catalog, while most spatiotemporal clusters occurred on the western part of the Kii Peninsula.

3.6 Izu area

We selected earthquakes in a rectangle box from 34° N to 36° N and 138° E to 140° E, where seismicity is dominated by the 2000 Izu swarm sequence (Figure 3.13a). The Izu swarm sequence is one of the largest swarm sequences occurred in Japan, which produced nearly 4000 M ≥ two events during the first week of the sequence and was associated with eruptions of the Miyakejima volcano [Ukawa et al., 2000; Toda et al., 2002]. Spatial distribution of seismicity (Figure 3.13a) shows there are five larger earthquake clusters occurred in this area, three occurred offshore and two occurred on the landside. Clusters occurred offshore are associated with the 2009 M6.4 Shizuoka earthquake, the 2000 Izu swarm sequence, and rapid swarm activity in the eastern side of the Izu Peninsula [Okada et al., 2000; Morita et al., 2006; Ueno et al., 2012]. Clusters in the inland area are mostly around Mt. Fuji and one M ≥ 6

mainshock triggered by the 2011 Tohoku earthquake on the Shizuoka Prefecture [Toda et al., 2011a, 2011b]. Here we adopted earthquakes occurred at depths shallower than 50 km based on the depth distribution (Figure 3.13b). Temporal distribution of *Mc* shows a value below 1.5 but a sudden jump to 2.5 immediately after the 2000 Izu swarm sequence (Figure 3.13c). We used cutoff magnitude 2 for the input catalog.

The best combination for *S* and *T* in this region is $S = 0.01°$ and $T = 512$ days, which resulted in a constant background seismicity rate throughout the study period (Figure 3.14b). The spatial distribution (Figure 3.15b) also displays homogenous locations compared to the input catalog (Figure 3.15a). For the spatiotemporal clusters, it is clear that this algorithm successfully selected the seismic bursts associated with seismic swarms (Figure 3.14c), which also corresponds to the dense seismicity in the space-time plot (Figure 3.15c). Several spatiotemporal sequences are also observed in the entire study area associated with the 2011 M9.0 event.

3.7 Tottori prefecture

On October 6, 2000, a M7.3 earthquake stroke the western Tottori Prefecture. Hypocenter depth distribution of the aftershocks indicates the thickness of the seismogenic layer is about 20 km [Ohmi et al., 2002]. Two clusters occurred off-fault area after the M7.3 Tottori mainshock, which suggested that seismicity in those surrounding areas might have been triggered by the Tottori mainshock. We selected earthquakes in a rectangle box from 34.5° N to 36° N and 132.5° E to 134° E (Figure 3.16a), the temporal change of *Mc* shows a low range from 0.2 to 0.8, but a sudden jump to 2.5 occurred immediately after the Tottori mainshock (Figure 3.16c). Hypocenter depths of earthquakes with magnitude above *Mc* are shallower than 25 km (Figure 3.16b). Therefore, we use cutoff magnitude 2.0 and depth $\leq$ 25 km for the clustering analysis. Seismicity rate for $M \geq 2.0$ and depth $\leq$ 25 km shows a smoothed pattern (Figure 3.17a), which only changes during the aftershock period of the Tottori mainshock. The best parameter found for this area is $S = 0.03°$ and $T = 64$ days. Background seismicity shows a homogenous pattern throughout the entire study period temporally and spatially (Figure 3.17b and Figure 3.18b, respectively), which suggests that the aftershocks triggered by the Tottori mainshock are successfully captured with the parameters.

3.8 Iwate region

To analyze background seismicity in the Iwate region, we select earthquakes in rectangle box from 34.5° N to 36° N and 132.5° E to 134° E, avoiding the aftershocks associated with the 2011 M9.0 Tohoku mainshock (Figure 3.19a). Three $M \geq 6$ mainshocks occurred at shallow depth (< 15 km) during the study period. Hypocenter depth distribution of earthquakes indicates that earthquakes occurred in this area can be divided into shallow part (0 - 40 km) and deeper part (60 - 150 km). Temporal distribution of *Mc* (Figure 3.19b) shows a general low *Mc* close to 1 but a sudden jump to 2.45 after the 2008 Iwate-Miyagi-nairiku earthquake (hereinafter Iwate earthquake). There is another increase of *Mc* occurred after the 2011 M9.0 Tohoku earthquake, which might be due to the larger number of aftershocks caused by the M9.0 mainshock. We used earthquakes occurred at depth shallower than 40 km and cutoff magnitude 2.0 for estimating background seismicity. Despite the seismicity increase associated with $M \geq 6$ mainshocks, both temporal distribution (Figure 3.20) and spatial distribution (Figure 3.21) indicate that this entire

study area has been suffered from the triggered seismicity after the 2011 Tohoku-oki earthquake. We found a seismicity rate increase in the period of 2011/03/11 to 2011/06/26. The best combination of the parameters for this area is S = 0.02° and T = 512 days. Temporal distribution of background seismicity shows a homogenous pattern except an apparent increase in the period of 2011/03/11 to 2011/06/26. Space-time distribution also indicates that background seismicity (Figure 3.21b) occurred during this period is different from the clustered seismicity (Figure 3.21c). We will discuss this issue in the next chapter.

3.9 2011 M9.0 Tohoku-Oki rupture area

2011 M9.0 Tohoku earthquake stroke east Honshu Island, with enormous aftershocks and the ensuing tsunami near east coast of Honshu took nearly 20,000 lives, marked as one of the most natural disasters ever recorded [Geller, 2011; Hayes et al., 2011; Simons et al., 2011; Stein et al., 2011]. The Tohoku earthquake indeed triggered the seismicity on the entire Japan Islands, which provided us the best example for studying the earthquake triggering behavior [e.g., Ruff and Kanamori,1980; Minoura et al., 2001; Sugawara et al., 2013]. We selected earthquake occurred in a rectangle box from 34° N to 41° N and 139° E to 136° E and chose cutoff magnitude 4.0 according to the temporal change of Mc (Figure 3.22a and Figure 3.22b). Earthquakes occurred in this area could be divided into two groups based on their hypocenter depths (Figure 3.22c). Most of the earthquakes occurred at depths shallower than 20 km, the others occurred at a deeper depth range that are related to the subduction processes. Here we chose hypocenter depth shallower than 50 km for estimating the background seismicity.

Figures 3.23a, b, and c indicate the comparison between the input catalog, background seismicity, and spatiotemporal sequence. The best combination of the parameters is S = 0.09° and T = 512 days. Computed background seismicity shows a seismicity rate decreased after the M9.0 mainshock. Annual seismicity rate of 60.6 earthquakes per year dropped to 58.2 earthquakes per year. The comparison of between space-time distribution input catalog (Figure 3.24a), background seismicity (Figure 3.24b) and spatiotemporal cluster (Figure 3.24c) also shows that most of the events are identified as spatiotemporal sequences associated with the 2011 Tohoku earthquake. We will also discuss this issue in the next chapter.

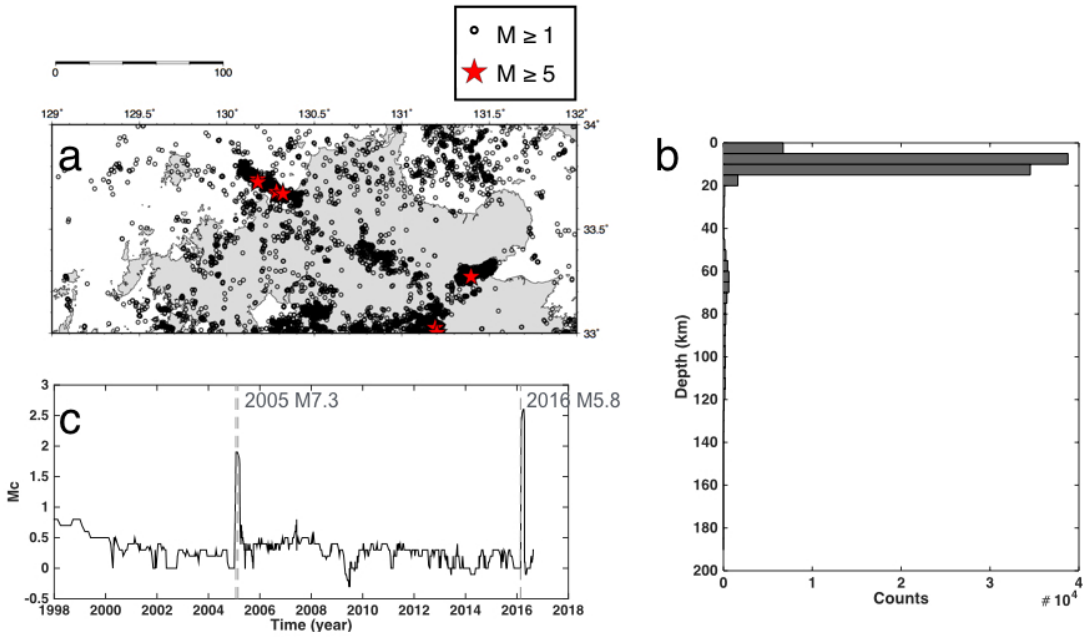

Figure 3.1 Seismicity of Northern Kyushu. (a) Spatial distribution. Black circle indicates M ≥ 1 event, red stars denote M ≥ 5 events. (b) Focal depth distribution. (c) Temporal change of *Mc*. *Mc* is computed by software Zmap (Weimer, 2001). The calculation is approached by the maximum likelihood method with minimum numbers of 100 earthquakes. The timing of each M ≥ 5.5 event is marked by a vertical gray line. Here we use cut off Magnitude = 1 and depth below 20 km for the analysis.

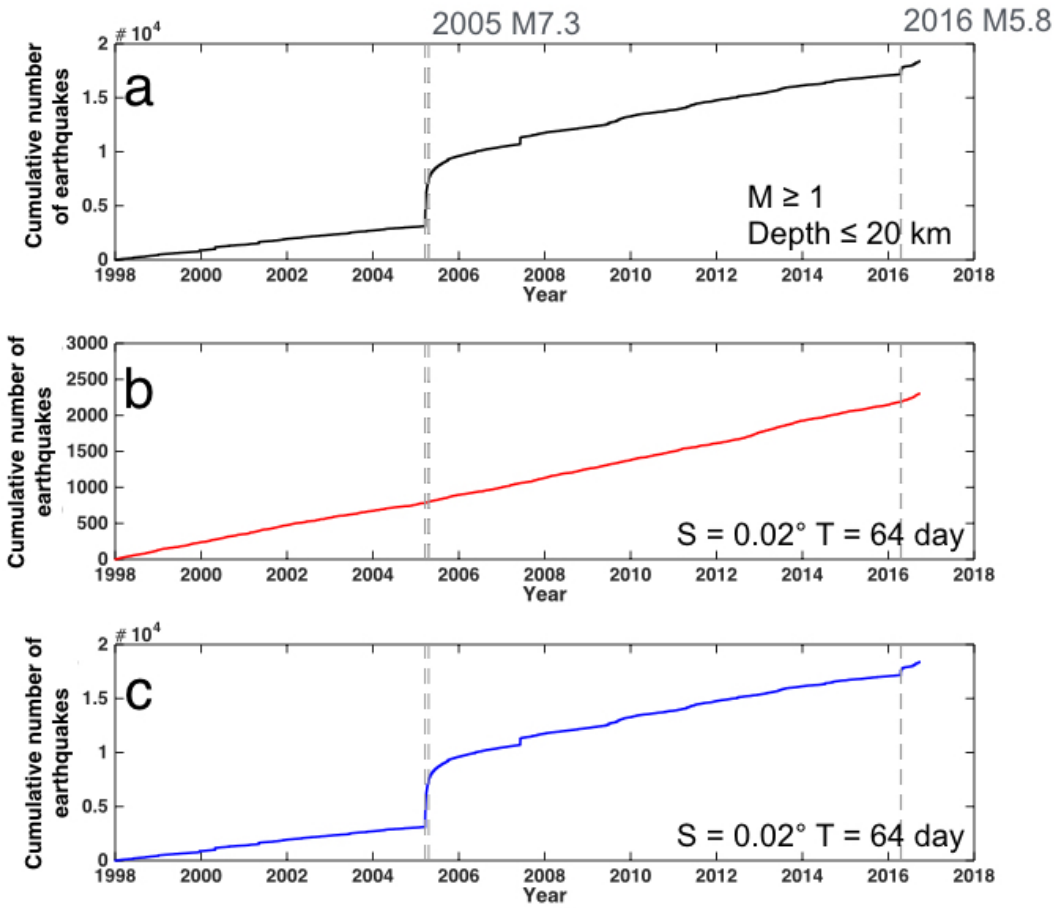

Figure 3.2 Temporal distribution of seismicity in Northern Kyushu region of (a) input catalog, (b) background seismicity and (c) spatiotemporal seismicity. Dashed grey line indicates the occurrence time of M ≥ 5.5 event. The suggested combination of S and T for seismicity Northern Kyushu are S = 0.02° and T = 64 days.

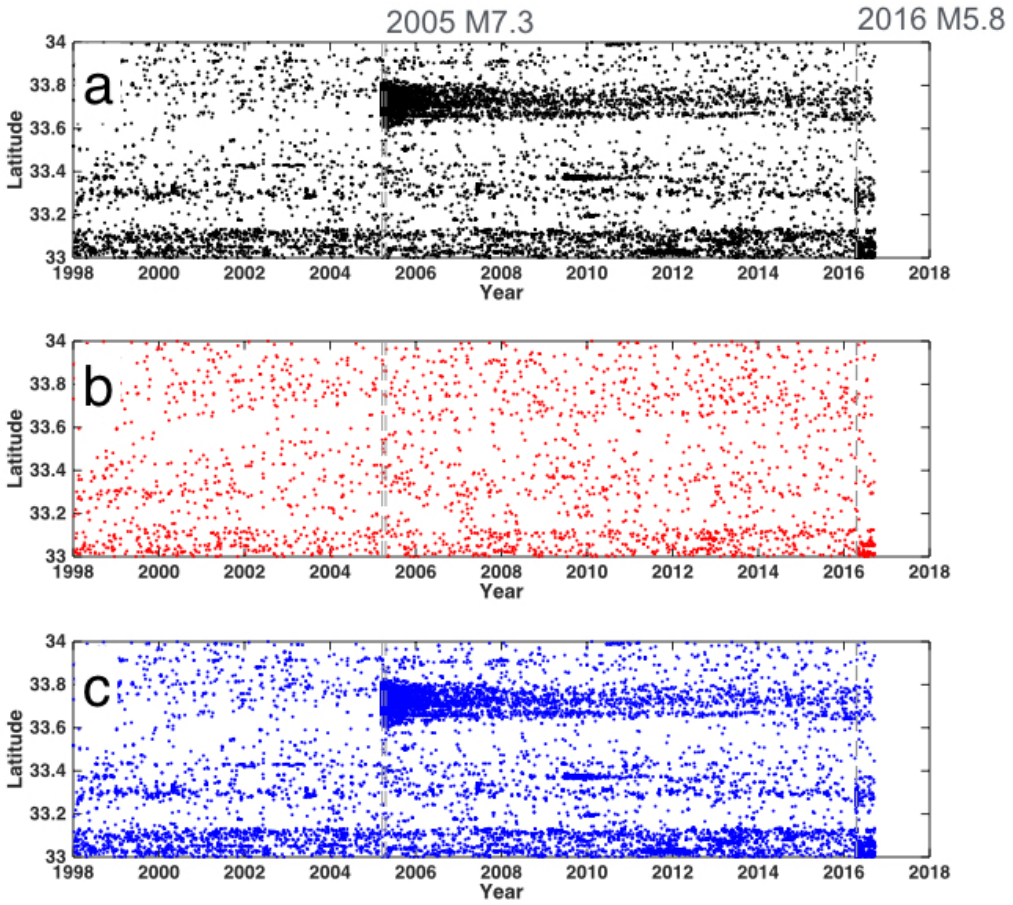

Figure 3.3 Space-time distribution in Northern Kyushu region. (a) Input catalog. (b) Background seismicity. (c) Spatiotemporal seismicity. Horizontal line represents occurrence time and vertical line represents latitude. Dashed grey line indicates the occurrence time of M ≥ 5.5 event. Space-time distribution of input catalog and spatiotemporal seismicity are identical, the spatial distribution of background seismicity shows a homogeneous throughout time, expect there is a high density appeared on the southern part of the study area, which might be related to the 2016 Kumamoto earthquake.

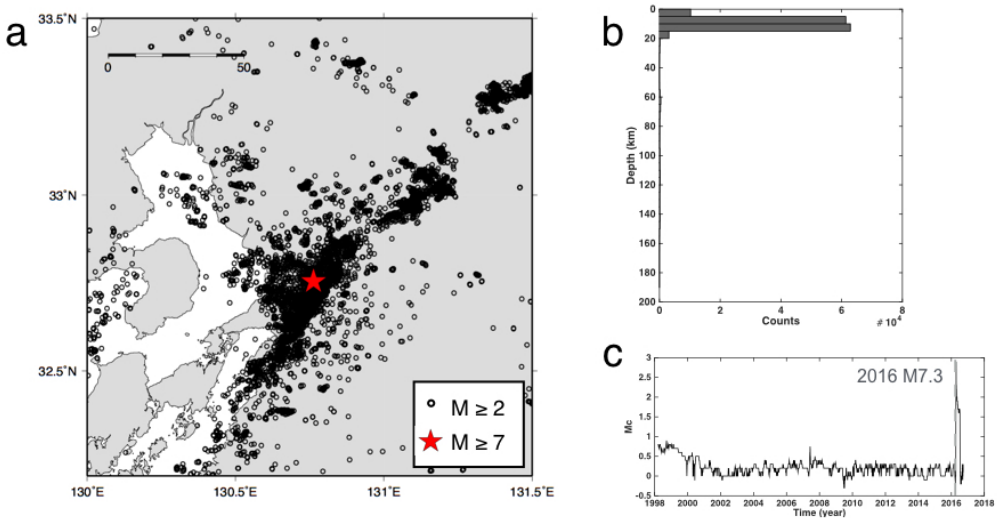

Figure 3.4 Seismicity of Central Kyushu. (a) Spatial distribution. Black circles indicate M ≥ 2 earthquakes, red stars denote M ≥ 6 events. (b) Focal depth distribution. (c) Temporal change of *Mc*. *Mc* is computed by software Zmap (Weimer, 2001). The calculation is approached by the maximum likelihood method with minimum numbers of 100 earthquakes. The timing of each M ≥ 6 event is marked by a vertical gray line. Here we use cut off Magnitude = 2 and depth below 20 km for the analysis.

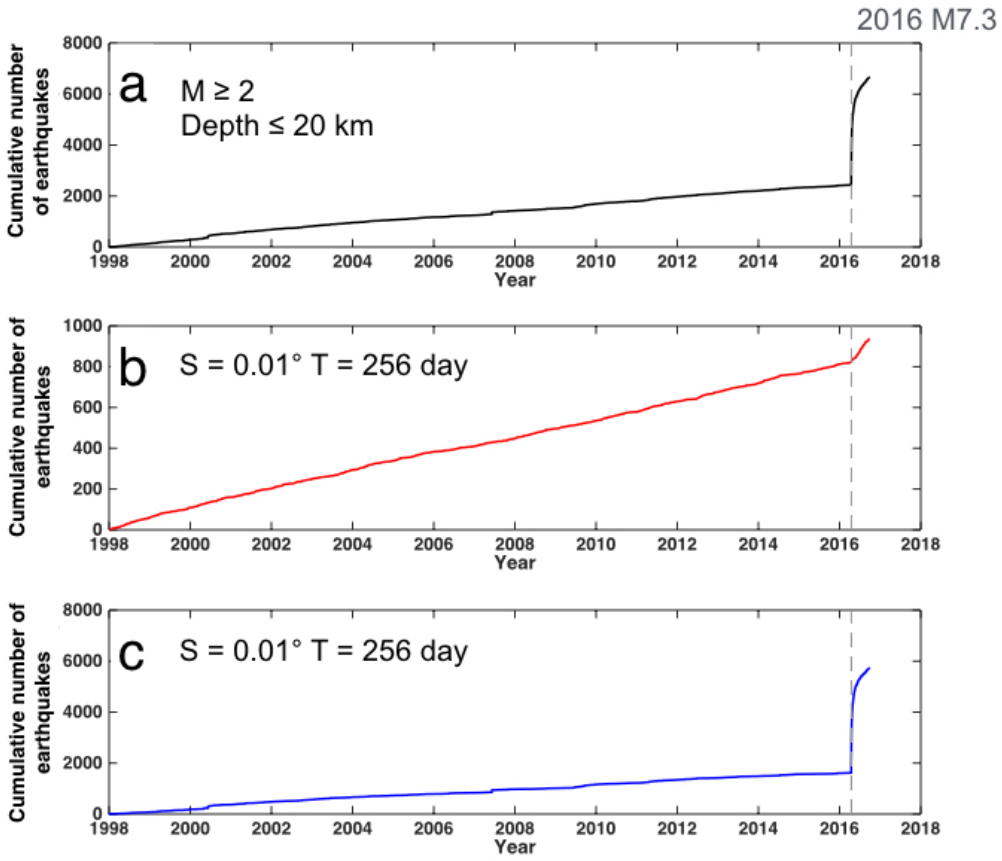

Figure 3.5 Temporal distribution of seismicity in Central Kyushu region of (a) input catalog, (b) background seismicity and (c) spatiotemporal seismicity. Dashed grey line indicates the occurrence time of M ≥ 6 event. The suggested combination of S and T for seismicity Central Kyushu are $S = 0.01°$ and $T = 256$ days. A constant background seismicity is estimated within this algorithm. It is worth notice that background seismicity rate increase after the 2016 Kumamoto earthquake.

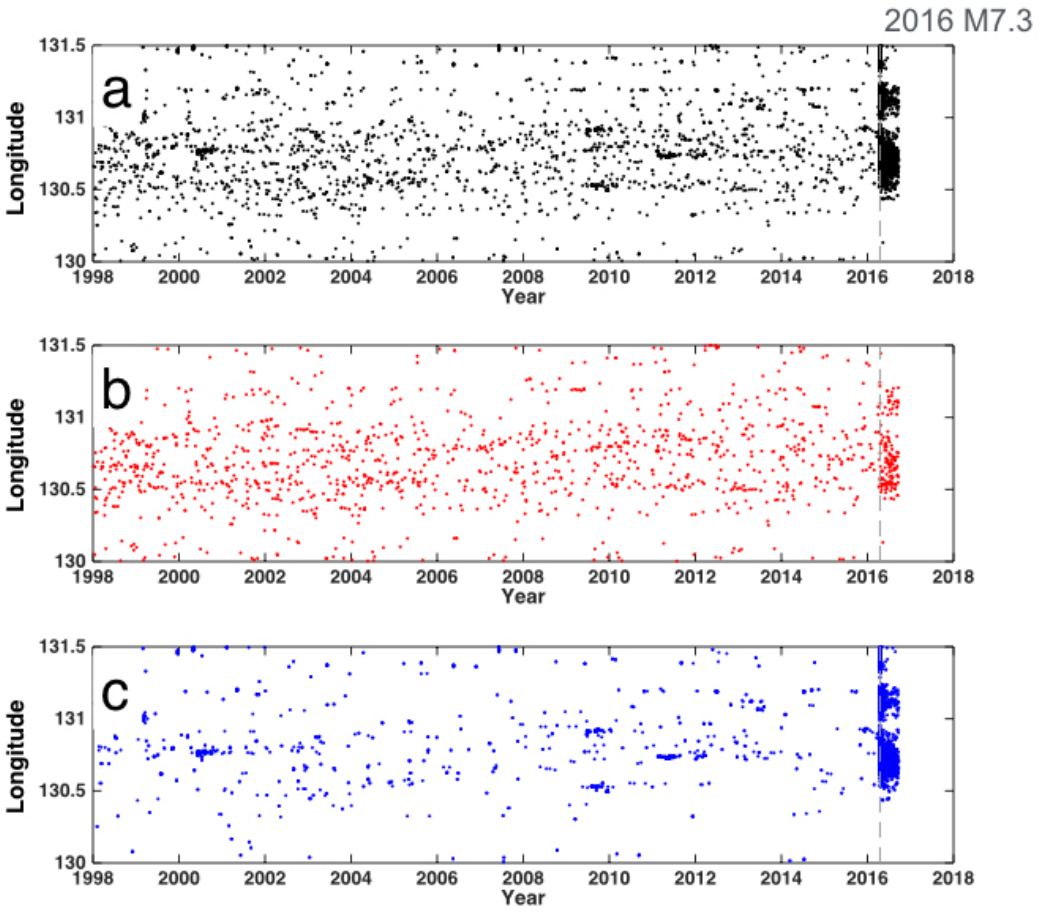

Figure 3.6 Space-time distribution in Central Kyushu region. (a) Input catalog. (b) Background seismicity. (c) Spatiotemporal seismicity. Horizontal line represents occurrence time and vertical line represents longitude. Dashed grey line indicates the occurrence time of M ≥ 6 events. Temporal and spatial distribution of input catalog and spatiotemporal seismicity are identical. It is worth noticed that a clearly seismicity rate increase occurred right after Kumamoto earthquake on the Kumamoto aftershock area.

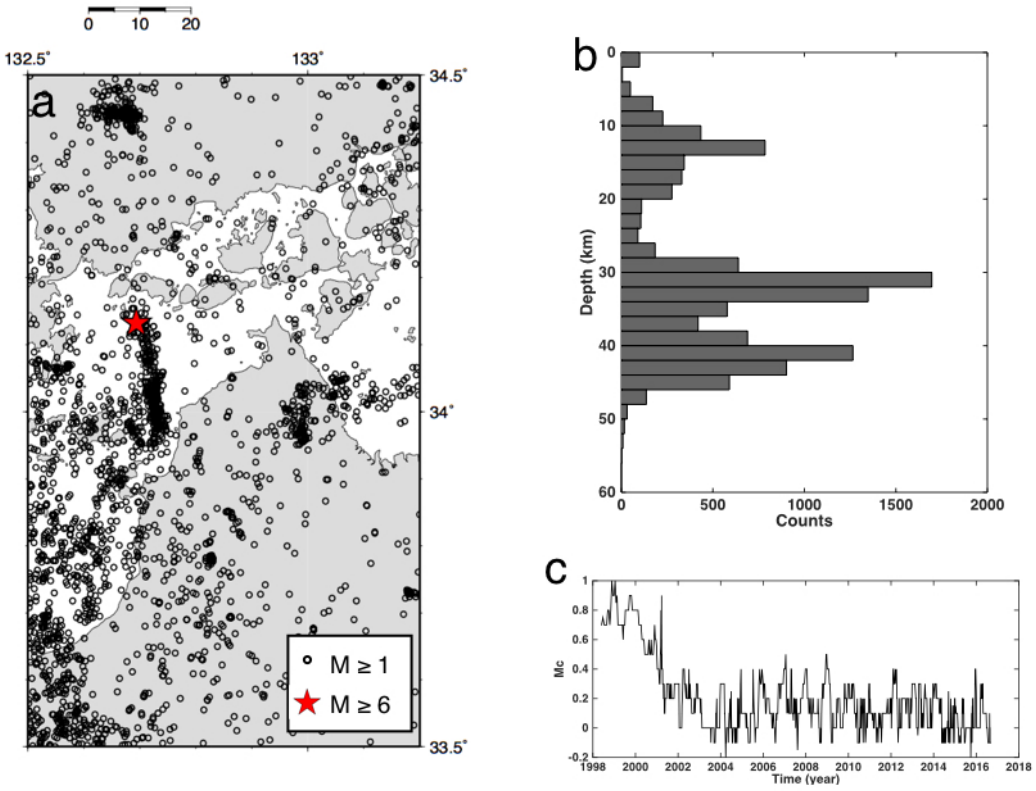

Figure 3.7 Seismicity of Geiyo area. (a) Spatial distribution. Black circle indicates M ≥ 1 event, red stars denote M ≥ 6 events. (b) Focal depth distribution. (c) Temporal change of *Mc*. *Mc* is computed by software Zmap (Weimer, 2001). The calculation is approached by the maximum likelihood method with minimum numbers of 100 earthquakes. The timing of each M ≥ 6 event is marked by a vertical gray line. Here we use cut off Magnitude = 1 and depth below 40 km for the analysis.

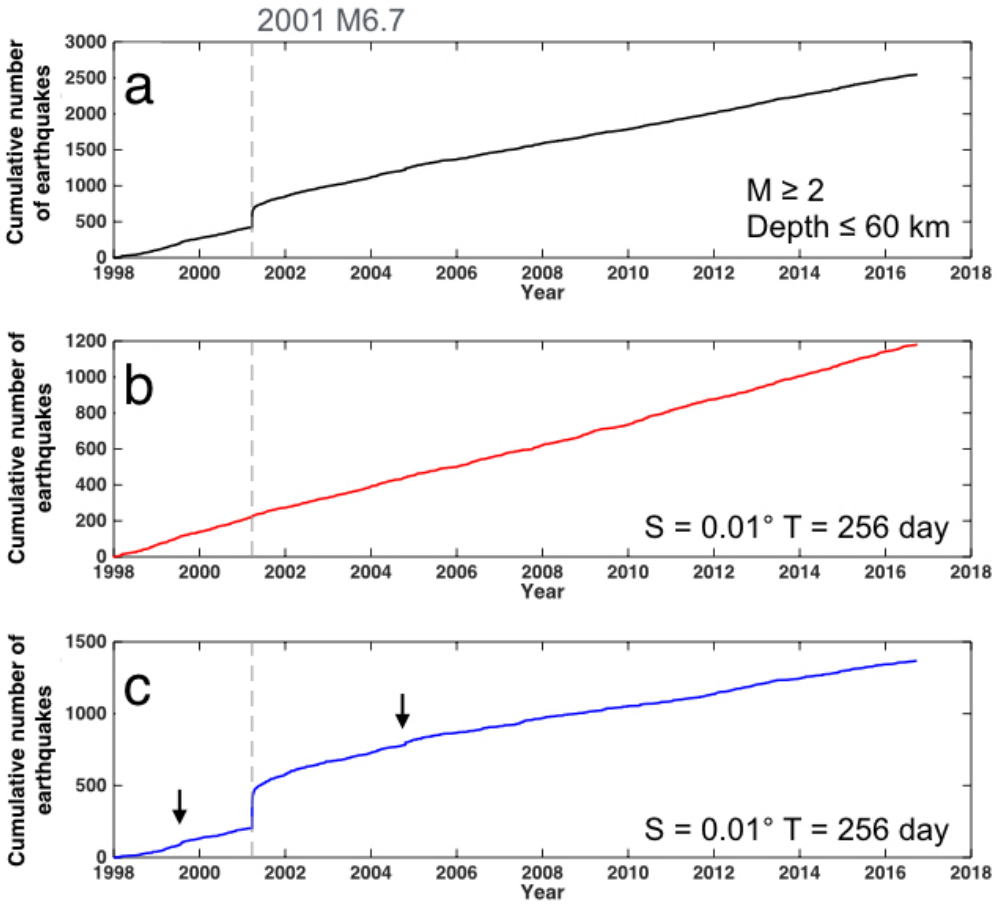

Figure 3.8 Temporal distribution of seismicity in Geiyo area of (a) input catalog, (b) background seismicity and (c) spatiotemporal seismicity. Dashed grey line indicates the occurrence time of M ≥ 6 event. The suggested combination of *S* and *T* for seismicity Geiyo area are *S* = 0.01° and *T* = 256 days.

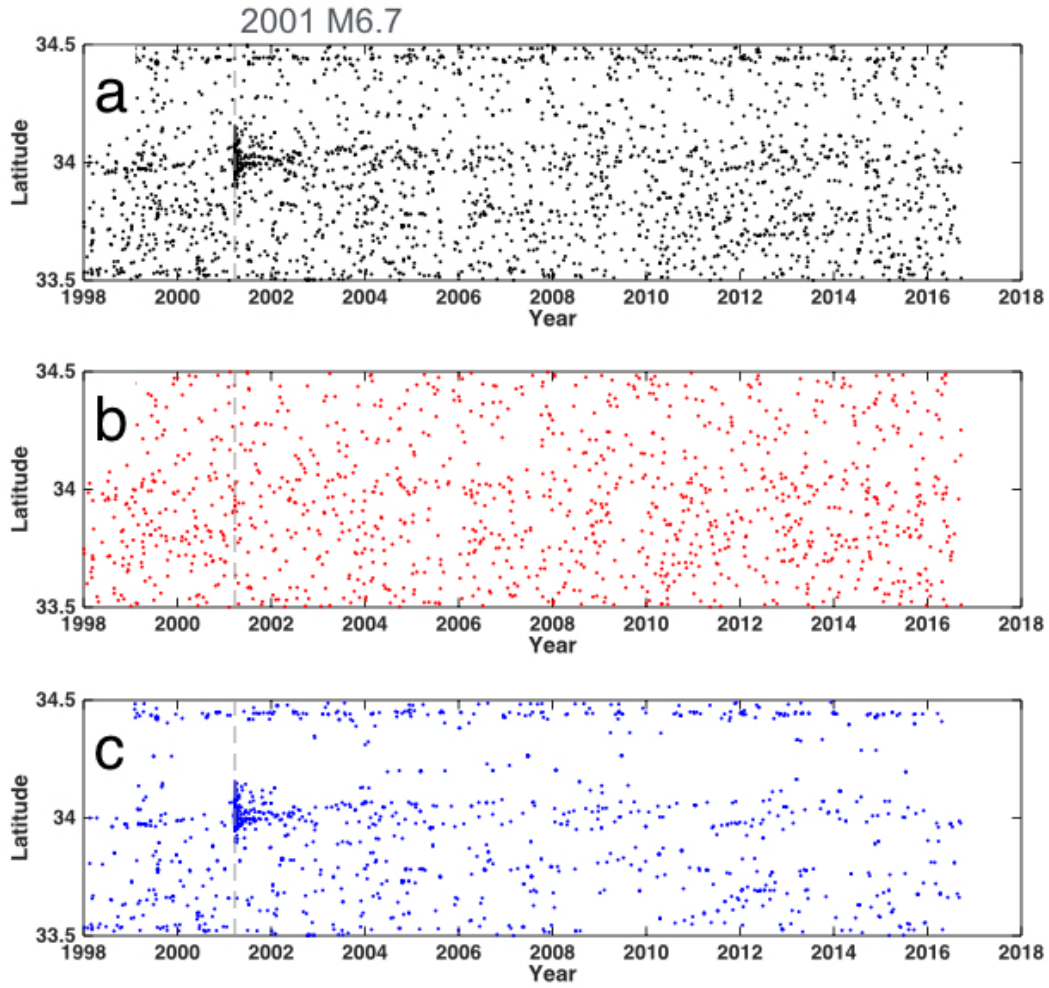

Figure 3.9 Space-time distribution in Geiyo area. (a) Input catalog. (b) Background seismicity. (c) Spatiotemporal seismicity. Horizontal line represents occurrence time and vertical line represent earthquake latitude. Dashed grey line indicates the occurrence time of $M \geq 6$ event. Temporal and spatial distribution of input catalog and spatiotemporal seismicity are identical.

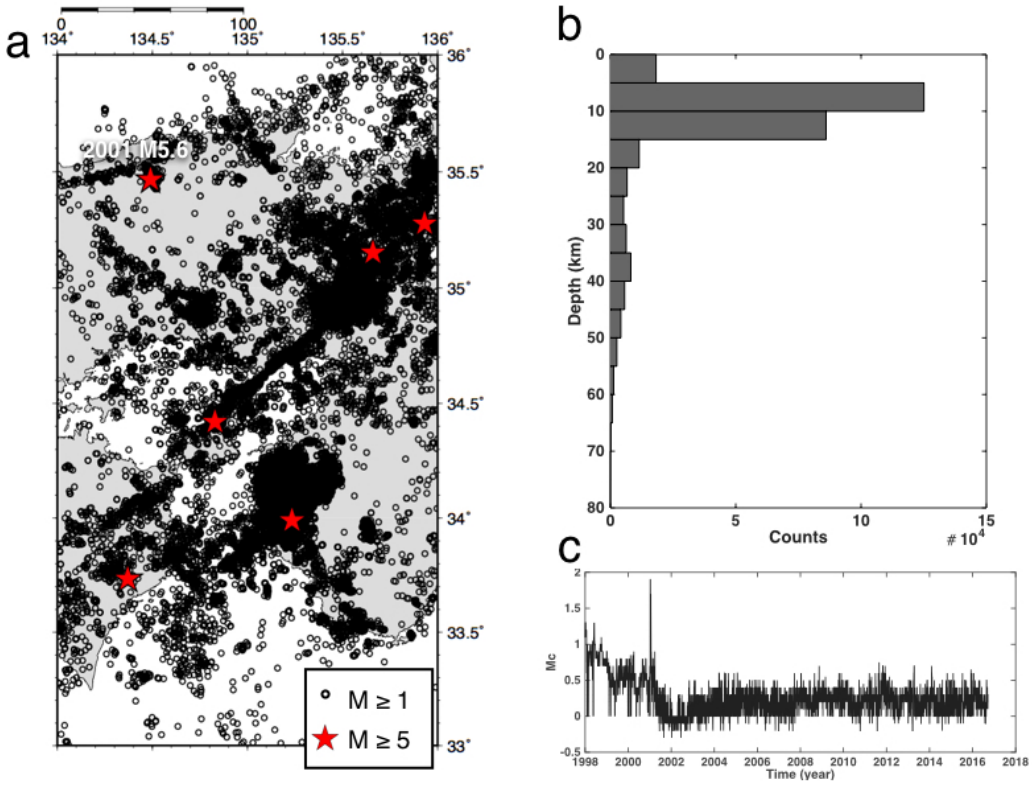

Figure 3.10 Seismicity of Kinki region. (a) Spatial distribution. Black circle indicates M ≥ 1 event, red stars denote M ≥ 5 events. (b) Focal depth distribution. (c) Temporal change of *Mc*. *Mc* is computed by software Zmap (Weimer, 2001). The calculation is approached by the maximum likelihood method with minimum numbers of 100 earthquakes. The timing of each M ≥ 6 event is marked by a vertical gray line. Here we use cut off Magnitude = 1 and depth below 20 km for the analysis.

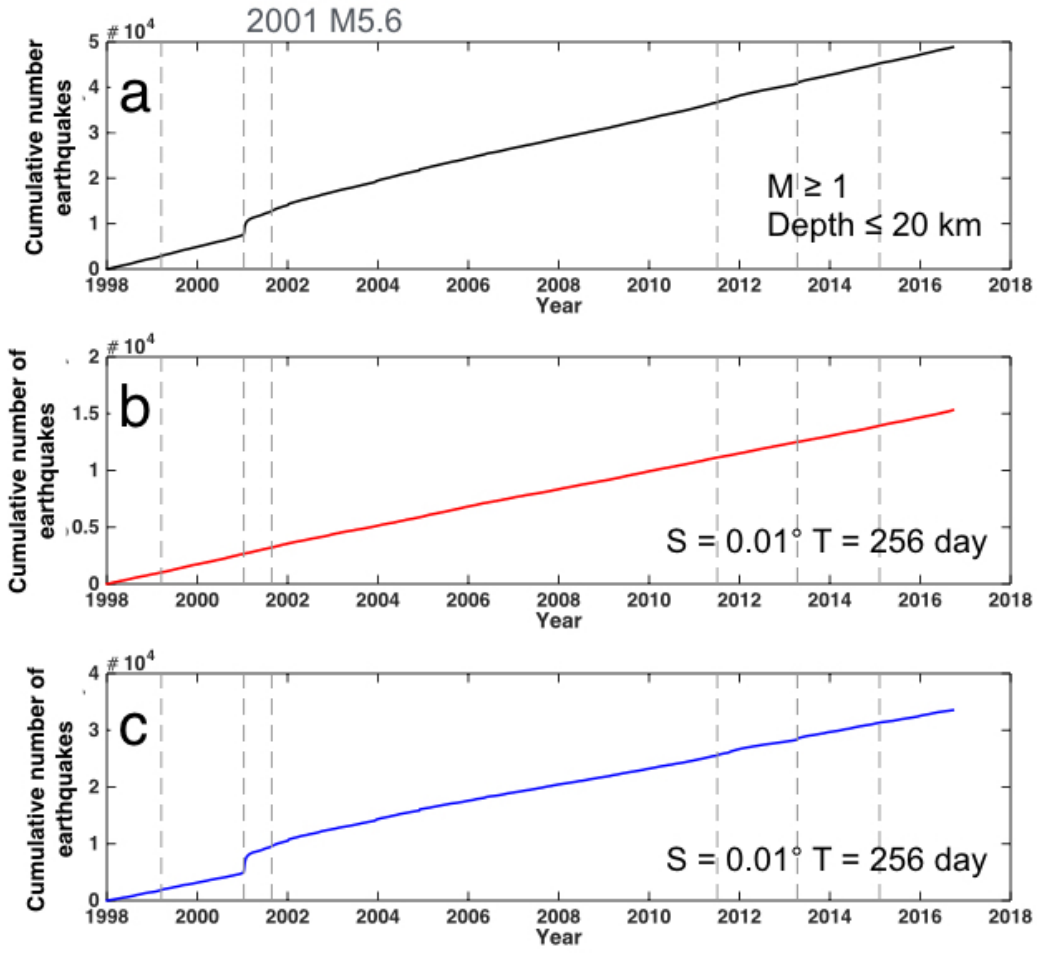

Figure 3.11 Temporal distribution of seismicity in Kinki region. (a) Input catalog, (b) background seismicity and (c) spatiotemporal seismicity. Dashed grey line indicates the occurrence time of M ≥ 6 events. The suggested combination of *S* and *T* for seismicity in the Kinki region are S = 0.01° and T = 256 days.

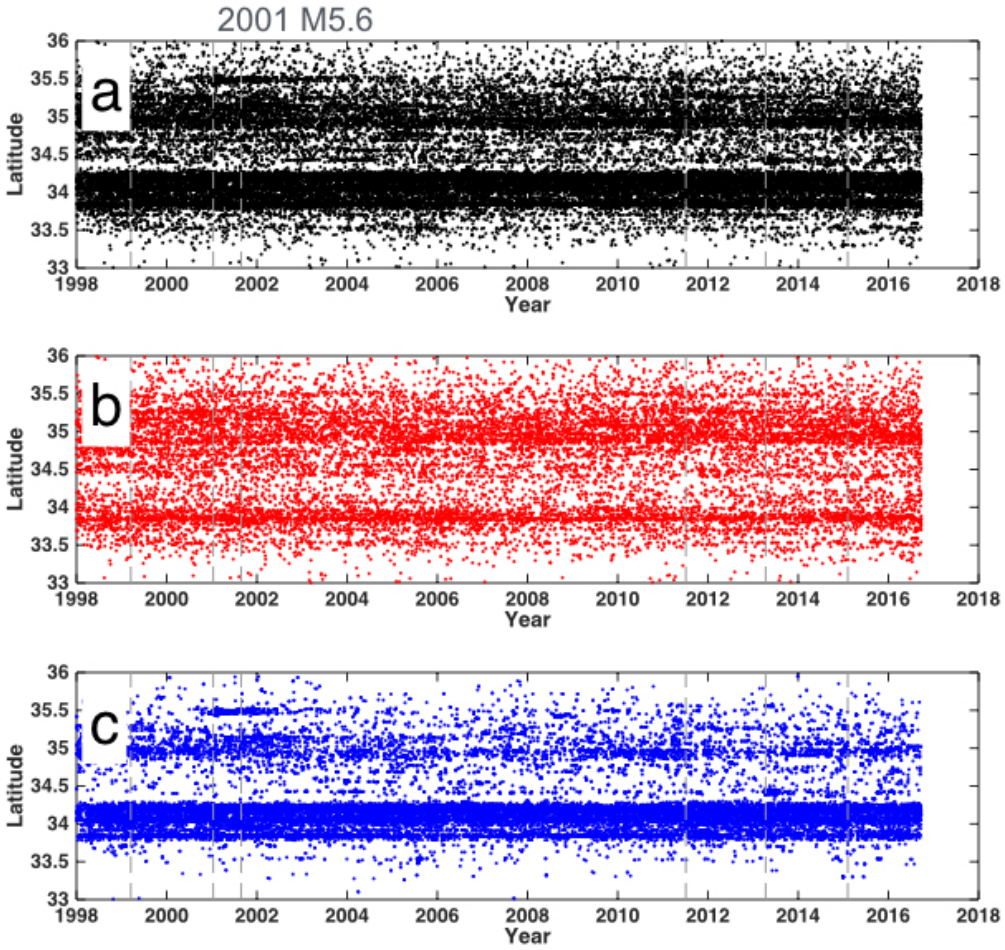

Figure 3.12 Space-time distribution in the Kinki region. (a) Input catalog. (b) Background seismicity. (c) Spatiotemporal seismicity. Horizontal line represents occurrence time and vertical line represents latitude. Dashed grey line indicates the occurrence time of M ≥ 6 event.

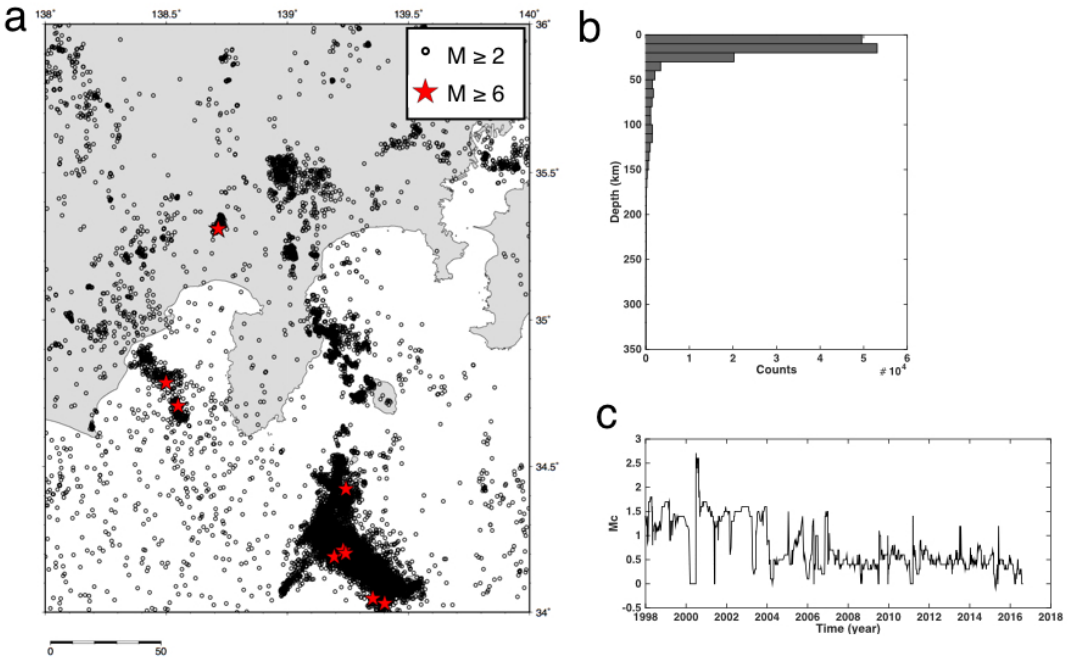

Figure 3.13 Seismicity in the Izu area. (a) Spatial distribution. Black circle indicates M ≥ 2 seismicity, red stars denote M ≥ 6 events. (b) Focal depth distribution. (c) Temporal change of *Mc*. *Mc* is computed by software Zmap (Weimer, 2001). The calculation is approached by the maximum likelihood method with minimum numbers of 100 earthquakes. The timing of each M ≥ 6 event is marked by a vertical gray line. Here we use cutoff magnitude = 2 and depth below 50 km for the analysis.

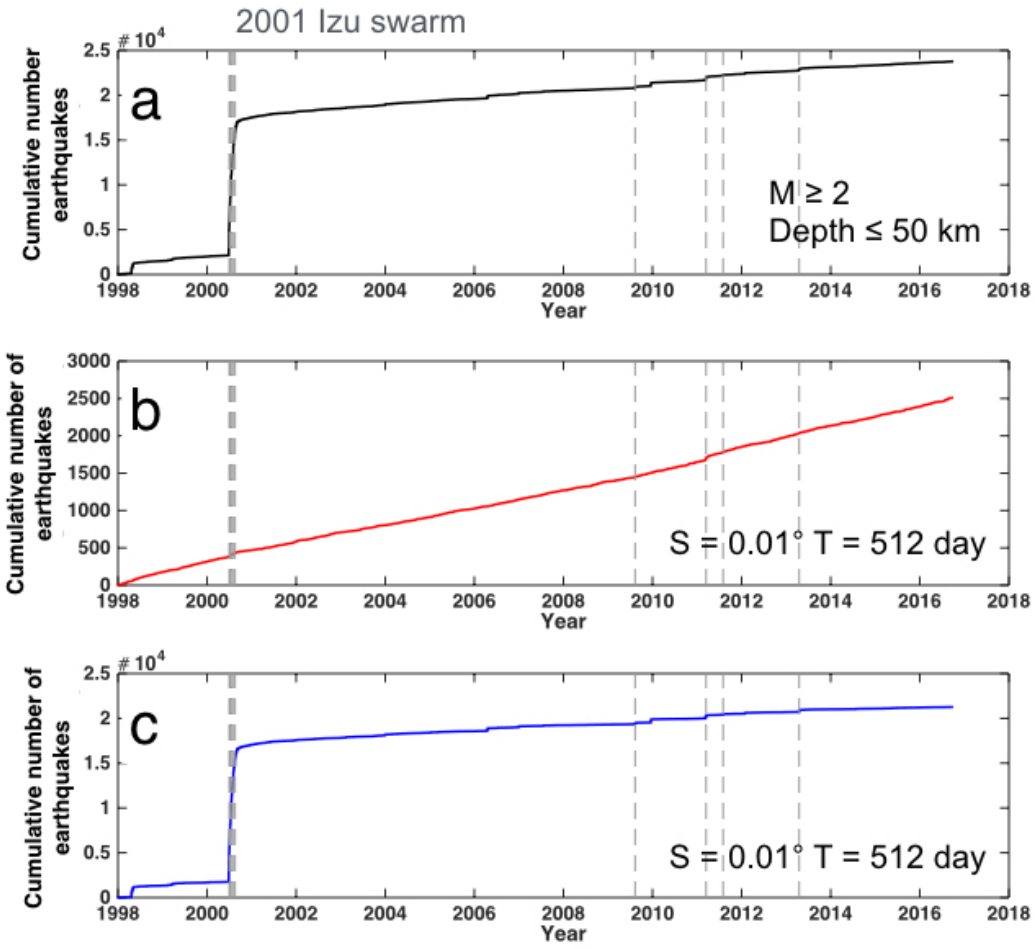

Figure 3.14 Temporal distribution of seismicity in Izu area. (a) Input catalog, (b) background seismicity and (c) spatiotemporal seismicity. Dashed grey line indicates the occurrence time of M ≥ 6 event. The suggested combination of S and T for seismicity are $S = 0.01°$ and $T = 256$ days.

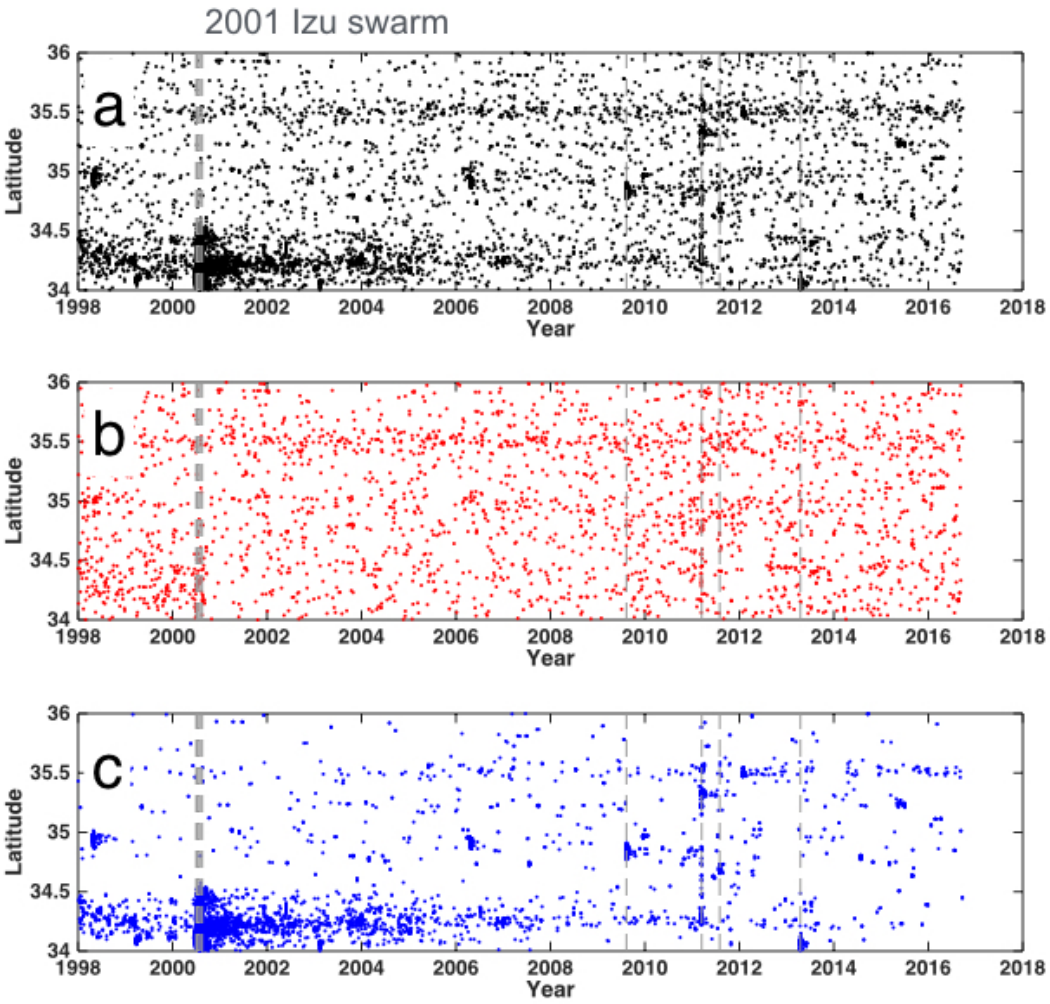

Figure 3.15 Space-time plot in Izu area. (a) Input catalog. (b) Background seismicity. (c) Spatiotemporal seismicity. Horizontal axes represent occurrence time and vertical axes represents latitude. Dashed grey line indicates the occurrence time of $M \geq 6$ event.

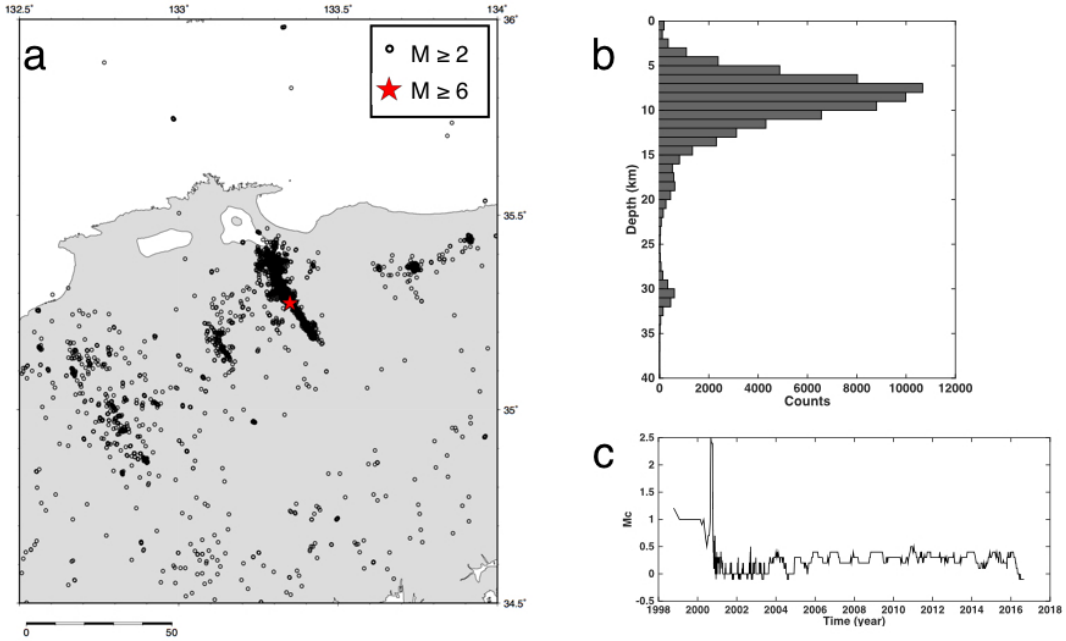

Figure 3.16 Seismicity of Tottori prefecture. (a) Spatial distribution. Black circle indicates M ≥ 2 seismicity, red stars denote M ≥ 6 events. (b) Focal depth distribution. (c) Temporal change of *Mc*. *Mc* is computed by software Zmap (Weimer, 2001). The calculation is approached by the maximum likelihood method with minimum numbers of 100 earthquakes. The timing of each M ≥ 6 event is marked by a vertical gray line. Here we use cut off Magnitude = 2 and depth below 40 km for the analysis.

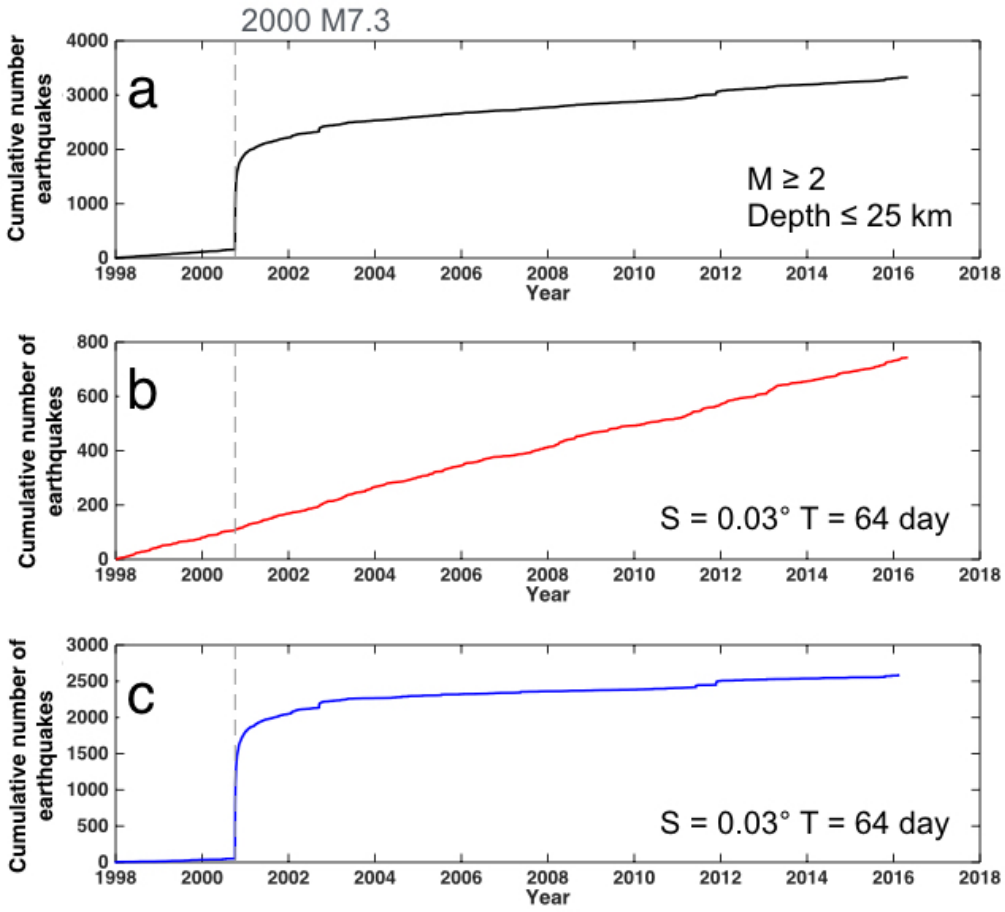

Figure 3.17 Temporal distribution of seismicity occurred in Tottori prefecture. (a) Input catalog, (b) background seismicity and (c) spatiotemporal seismicity. Dashed grey line indicates the occurrence time of M ≥ 6 event. The suggested combination of *S* and *T* for seismicity are *S* = 0.03° and *T* = 64 days.

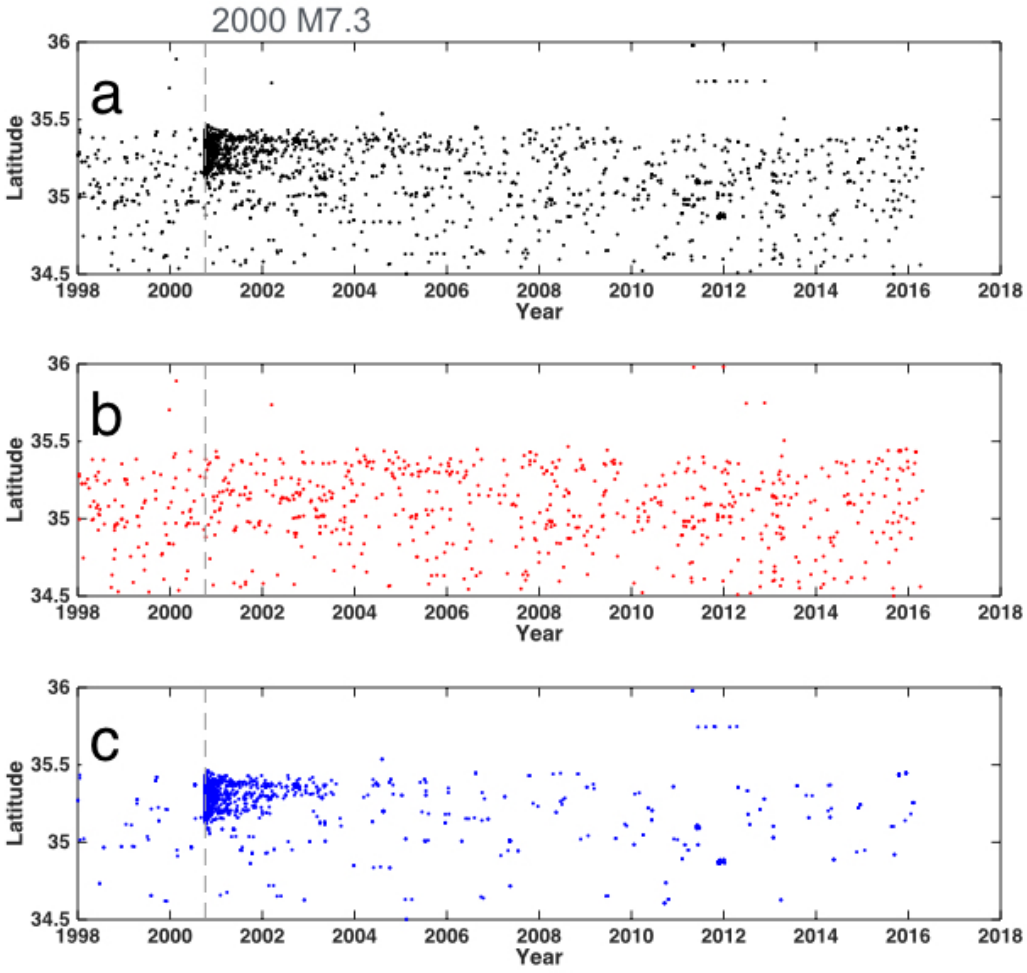

Figure 3.18 Space-time plot in Izu area. (a) Input catalog. (b) Background seismicity. (c) Spatiotemporal seismicity. Horizontal axes represent occurrence time and vertical axes represents latitude. Dashed grey line indicates the occurrence time of $M \geq 6$ event.

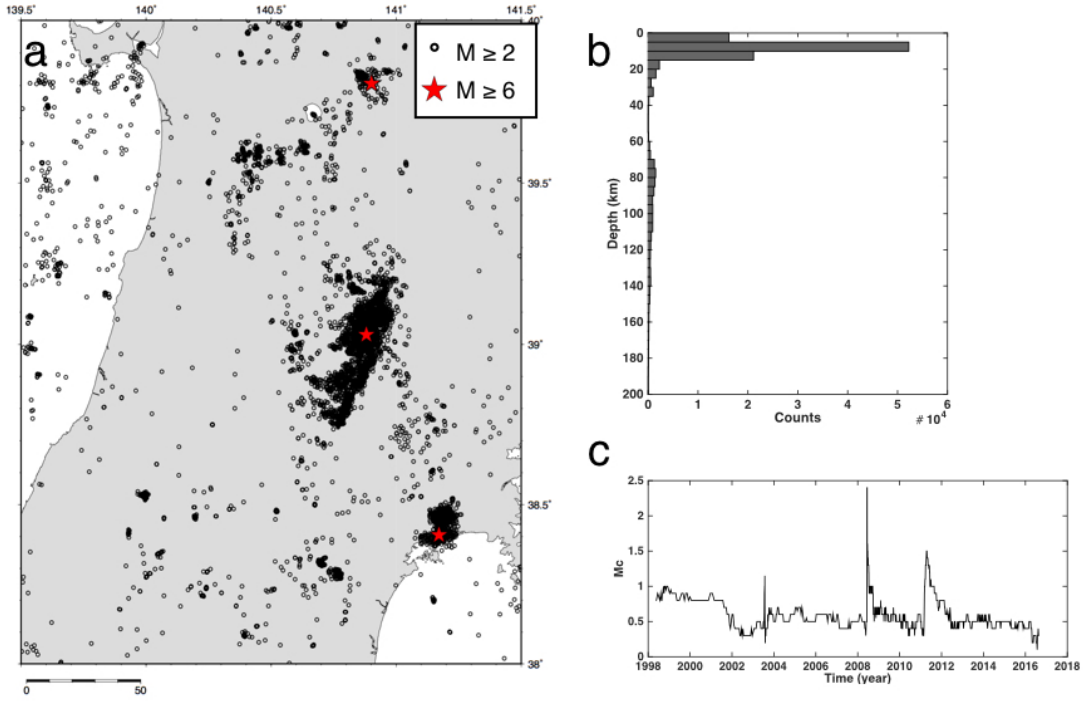

Figure 3.19 Seismicity of Iwate area. (a) Spatial distribution. Black circle indicates M ≥ 2 seismicity, red stars denote M ≥ 6 events. (b) Focal depth distribution. (c) Temporal change of *Mc*. *Mc* is computed by software Zmap (Weimer, 2001). The calculation is approached by the maximum likelihood method with minimum numbers of 100 earthquakes. The timing of each M ≥ 6 event is marked by a vertical gray line. Here we use cut off Magnitude = 2 and depth below 20 km for the analysis.

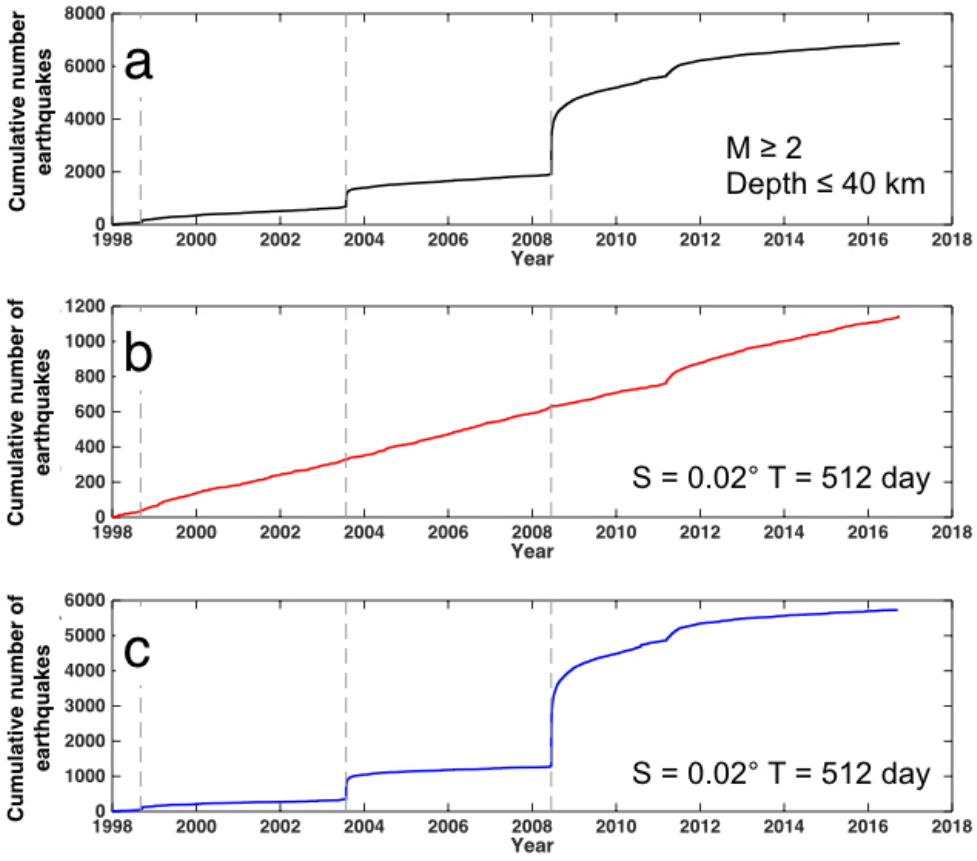

Figure 3.20 Temporal distribution of seismicity occurred in Iwate area. (a) Input catalog, (b) background seismicity and (c) spatiotemporal seismicity. Dashed grey line indicates the occurrence time of M ≥ 6 event. The suggested combination of *S* and *T* for seismicity are *S* = 0.02° and *T* = 512 days. It is worth noting that background seismicity increased during three months after 2011 Tohoku earthquake.

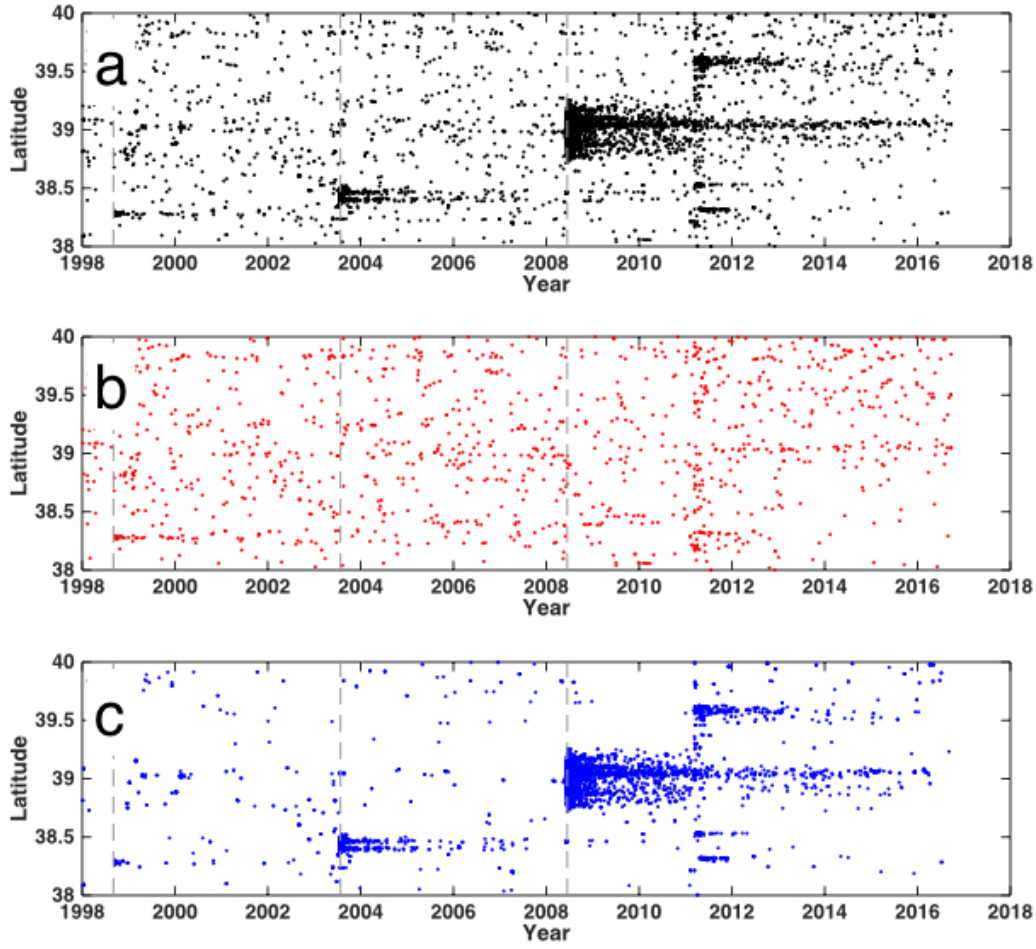

Figure 3.21 Space-time distirbution in Iwate area. (a) Input catalog. (b) Background seismicity. (c) Spatiotemporal seismicity. Dashed grey line indicates the occurrence time of M ≥ 6 event.

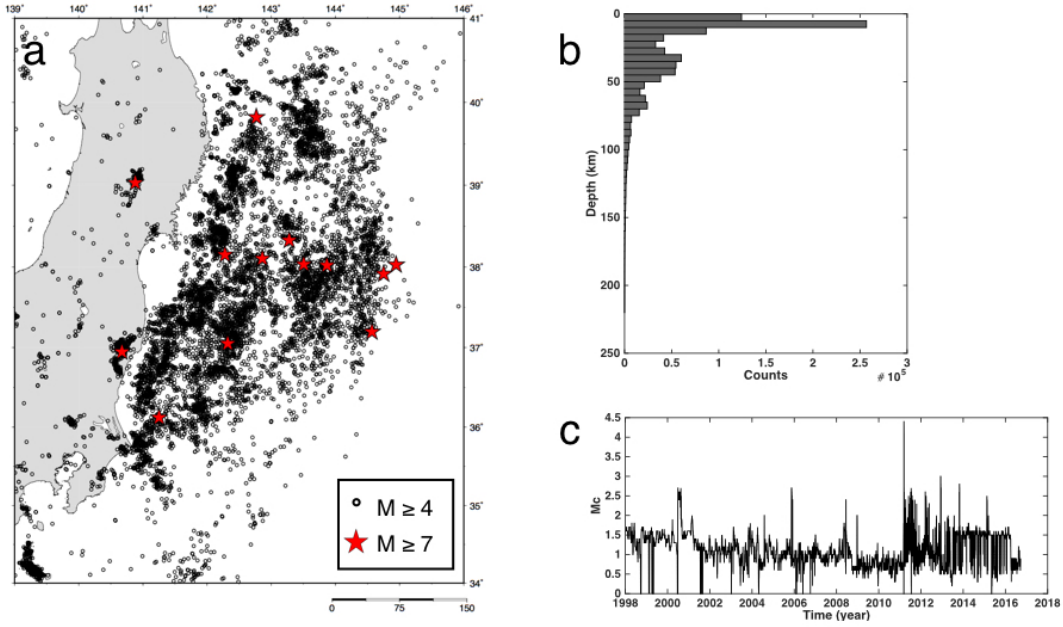

Figure 3.22 Seismicity of Tohoku area. (a) Spatial distribution. Black circle indicates M ≥ 4 seismicity, red stars denote M ≥ 6 events. (b) Focal depth distribution. (c) Temporal change of *Mc*. *Mc* is computed by software Zmap (Weimer, 2001). The calculation is approached by the maximum likelihood method with minimum numbers of 100 earthquakes. The timing of each M ≥ 6 event is marked by a vertical gray line. Here we use cut off Magnitude = 4 and depth below 50 km for the analysis.

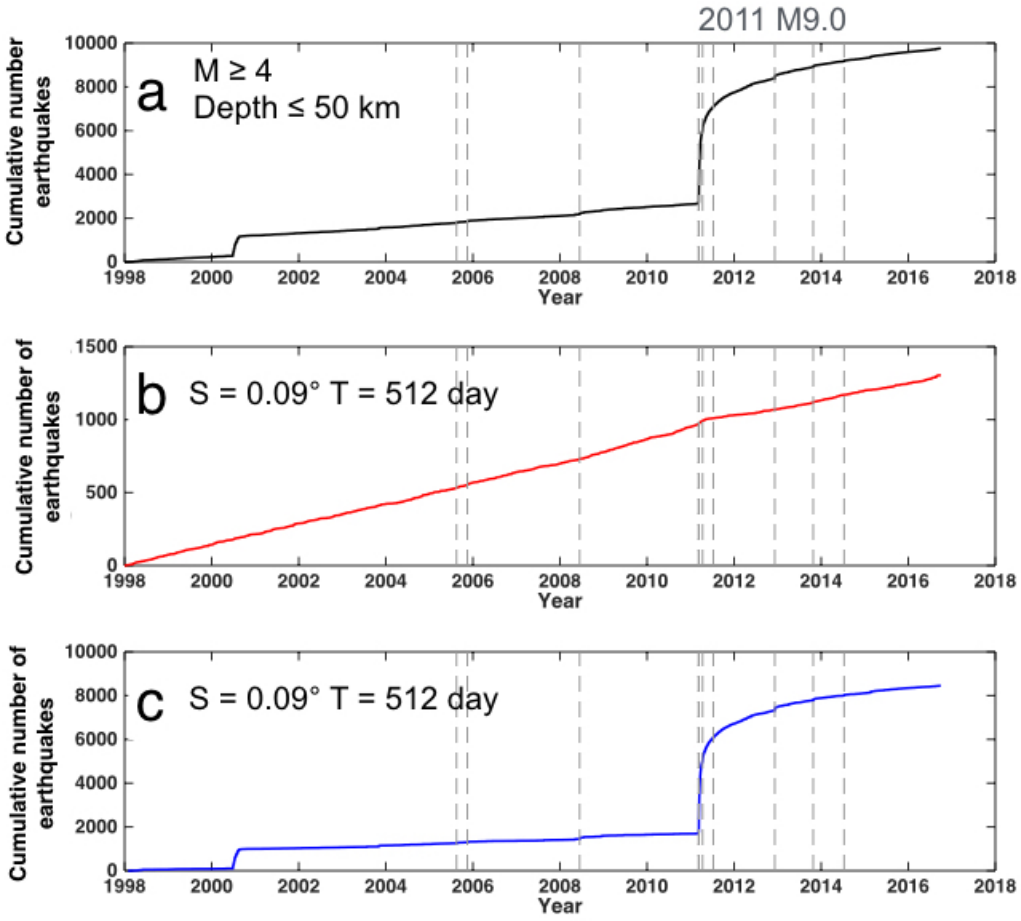

Figure 3.23 Temporal distribution of seismicity occurred in Tohoku area. (a) Input catalog, (b) background seismicity and (c) spatiotemporal seismicity. Dashed grey line indicates the occurrence time of M ≥ 6 events. The suggested combination of S and T for seismicity are $S = 0.02°$ and $T = 512$ days. It is worth noting that background seismicity decreased after the 2011 Tohoku earthquake.

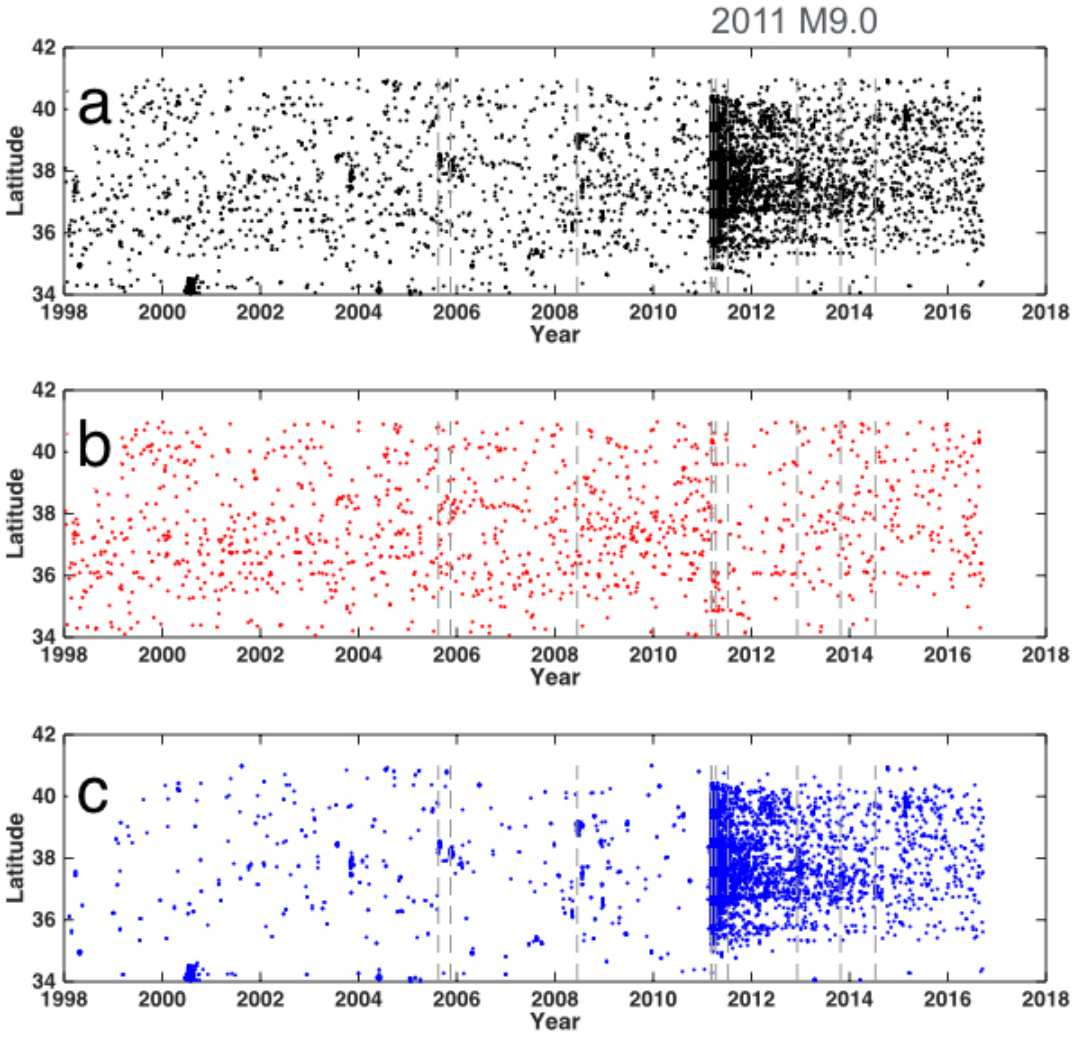

Figure 3.24 Space-time plot in Tohoku area. (a) Input catalog. (b) Background seismicity. (c) Spatiotemporal seismicity. Dashed grey line indicates the occurrence time of M ≥ 6 event.

Chapter 4 Discussion

4.1 Non-Stationary estimated background seismicity

4.1.1 Case of Iwate region

Figure 3.20 indicates a sudden increase of background seismicity associated with the 2011 M9.0 Tohoku earthquake. A question is that if this result is a true or false detection due to fundamental limitation of the algorithm. One common flaw for any declustering algorithms is that they often fail to decluster earthquake catalog if the source fault of a large earthquake is located out of the study area. It is because these algorithms define their spatial parameters either with the mainshock magnitude (e.g., equation 1.10) or with a smoothed distance by a kernel function (e.g., equation 1.18). Those assumptions lead to a general limitation of declustering earthquakes occurred very far away from the mainshock or source area, which tends to regard them as background seismicity. Our new algorithm, instead, does not include any parameter directly associated with earthquake magnitude. Therefore, it should have worked to decluster the input catalog properly. However, we observed the sudden increase of background seismicity after the 2011 M9.0 event. So far, we do not know which factor brought such a significant rate change in background seismicity.

In our algorithm, background seismicity is computed from two parts, one is the spatially independent events isolated with spatial range confined by S° and temporal range confined by T day, the other is the temporally independent events with backward rate threshold to split a spatial cluster into temporal clusters. During the period sustaining high rate of seismicity, from 2011/03/11 to 2011/06/20, these background events are mostly identified as spatially independent events. Figure 4.1a shows the temporal distribution of spatially independent events after step 1. A remarkable seismicity rate increase appears in the time period from 2011/03/11 to 2011/06/20. Furthermore, the space-time distribution (Figure 4.1b) indicates that those spatially independent events occurred pervasively in the study area, which suggests that sudden increase of background seismicity rate after the 2011 Tohoku-oki earthquake might be real and thus the 2011 Tohoku earthquake has changed the local stress field and activated the background seismicity.

4.1.2 Case of Tohoku area

Figure 3.23b indicates an apparent rate decrease in background seismicity right after the 2011 M9.0 Tohoku-oki earthquake, annual seismicity rate dropped from 60.6 per year to 58.2 per year. Space-time distribution shows a comparable seismicity rate change between 1.5 years before and after Tohoku earthquake (Figure 3.24b). However, we found that this seismicity rate decrease is a false detection due to over-declustering associated with a 2-Dimension grid. Figure 4.2 shows a schematic plot that two earthquakes occurred at a wide range of hypocenter depths, in which these events are normally linked as one spatial cluster in the 2D grid system. Seismicity in this area includes onshore crustal earthquakes shallower than 20 km and events deeper than 50 km associated with the subduction process. Therefore,

it is likely that one spatial cluster has a wide variation of hypocenter depths. Figure 4.3 shows an example that a spatiotemporal sequence detected in 2D system contains earthquakes occurred in a range of 0-40 km deep, which suggests that using 2D grid has a possibility to perform over-declustering, leading to a false detection. To avoid such a situation, we then developed a 3-Dimension grid with two different types of coordinates: Cube and spheres. For cube grid, an additional depth parameter Z is applied, here we set Z is roughly equal to cell size in 2D to reduce the degree of freedom of parameters (e.g., for S = 0.01° x 0.01°, Z will be 1 km). For sphere system, we adopted a radius parameter r (km) for estimating the spatial coverage of spatiotemporal clusters.

4.1.2.1 Cube coordination

We first modified the 2-Dimension grid into the 3-Dimension grid. Additional depth parameter Z, height of a cube, is added into the algorithm. Figure 4.4 shows a comparison of computed background seismicity with 2-D case (blue) and 3-D case (red). The best parameter screened by the filtering process is S = 0.1°, Z = 10 km and T = 256 days. In Figure 4.4, using 3-Dimension grid has successfully reduced the over-declustering effect that observed with the 2-Dimension grid system. Instead, background seismicity shows a slight increase immediately after the 2011 M9.0 Tohoku-oki earthquake, by about 25% of the rate before the 2011 M9.0 event. Spatial distribution of background seismicity before and after the Tohoku-oki event (Figure 4.5a) reveals a seismicity rate increased in a small area from 36.5° N to 37.5° N and 140.3° E to 141° N. Figure 4.5b presents the temporal change of seismicity in the small area showing clear rate increase after the Tohoku-oki earthquake. This area is also the area that numerous normal faulting events were triggered by the 2011 Tohoku-oki event [e.g., Kato et al., 2011; Okada et al., 2011; Imanishi et al., 2012]. It suggests that this algorithm is sufficiently useful for detecting a change in local stress field.

4.1.2.2 Radius coordination

Another extension in 3-Dimension coordinates is to apply spheres with a radius parameter (r) to search neighboring earthquakes for linkages. Here we use parameter sets with r from 10 km to 100 km incremented by 10 km, and T from 1 to 1024 days for searching the proper parameter combination. The computation provided us the best parameter within r = 50 km and T = 256 days. Since the cutoff depth of the hypocenters in the input catalog is 50 km, r = 50 km means that the range of radius meets the bottom depth, which also suggests that an earthquake occurred at 0 km will be linked with other earthquakes occurred at depth 50km. Temporal distribution (Figure 4.6) of background seismicity with the sphere 3D grid is almost identical with the 2-D result, which suggests that this approach does not have any power to reduce the effect of over-declustering.

4.1.3 Case of Central Kyushu region

As shown in the chapter 3, we found that this algorithm did not completely select spatiotemporal clusters associated with the 2016 Kumamoto earthquake of M7.3. To seek the reason why the apparent background rate increase occurred after the Kumamoto earthquake, we first look at the two outputs

(spatial clusters, spatially independent events) from the first step of the algorithm. If we were to find that this background seismicity increase is dominated by the spatially independent events, we would conclude that the rate increase is true. Figure 4.7 shows the temporal distribution of spatially independent events. The temporal change of spatially independent events is smoothed compared to the final output (e.g., Figure 3.5b), which suggests the rate increase is derived from the second step of the algorithm.

We used the backward rate analysis for quantifying the temporal relationship between two continuous events, which is expected to be well described an earthquake inter-event time in each spatial cluster. However, we found that the backward rate analysis becomes a flaw in this case that the aftershock activity is still on-going. Figure 4.8 shows the estimated backward mean inter-event time (e.g., equation 2.3) for a spatial cluster including the Kumamoto mainshock. A sudden drop of $\overline{T_b}$ is observed after the Kumamoto event, we found that it is because the aftershock activity is still continuing. The backward rate will eventually increase and shorten the expected earthquake inter-event time ($\overline{T_b}$), which will be higher than the temporal threshold for extracting the temporal sequences. To check if the aftershock period influences the backward rate analysis, we selected the spatial clusters that are associated with the aftershock activity of the 2016 Kumamoto earthquake. There are two spatial clusters associated with the 2016 Kumamoto earthquake. We first calculated p-value for each spatial clusters and then simulated seismicity to the end of 2018 following the Omori-Utsu law. We then computed the algorithm for estimating the background seismicity. Figure 4.9a shows an example from a spatial cluster associated with the 2016 Kumamoto earthquake, whereas the synthetic seismicity is shown in Figure 4.9b. The computed background seismicity (Figure 4.9c) reproduced a more smoothed curve with the synthetic earthquake catalog. This test revealed one weakness of this algorithm that the real-time operation cannot be applicable for estimating the change in background seismicity during the on-going aftershock period. A hope would be that a real-time spatial cluster still can be selected from the first step of the algorithm.

4.1.4 Application for other cases using 3-Dimension grid

4.1.4.1 Kanto area

Previous studies suggested that stress loading (secure stressing rate) in Kanto area has changed by the 2011 Tohoku-oki mainshock [e.g., Toda and Stein, 2013; Uchida and Matsuzawa, 2013; Gardonio et al., 2015]. If the background stress level has changed since 2011, the background seismicity rate is also likely to have changed. Here we applied the 3-Dimension algorithm to estimate the background seismicity rate as a function of time in the Kanto region. We used earthquakes with their hypocenter depths shallower than 100 km and magnitudes larger than 2.5 for the input catalog. The temporal distribution (Figure 4.10a) for the background seismicity with the best parameter set also indicates the seismicity rate has increased since the 2011 Tohoku event. Figure 4.10b displays the depth-time plot for the background seismicity. Before the 2011 Tohoku event, background seismicity occurred mostly at depths of 40 to 50 km. But, since the Tohoku event, seismicity in a wide range of depths has become active. Figure 4.11 shows the comparison between seismicity shallower than 50 km (red line) and seismicity at depths of 50 to 100 km (blue line). We estimated background seismicity rate during two

years before and after the Tohoku-oki earthquake (note that the starting time for estimated background seismicity rate after the Tohoku-oki earthquake is from 2012/03/11). Background seismicity rate occurred at shallower depth only changes during a very short period and returned to the pre-Tohoku level. However, seismicity rate at depth deeper than 50 km has been lasting longer (at shortest until the end of 2016), keeping an ~130% increased rate of the pre-Tohoku level. The long-term high rate of background seismicity in the deeper part might suggest that Kanto area is still in the postseismic relaxation process of the Tohoku-oki event.

4.2 Parameter dependency for study area

Another important issue for the parameter dependency is that if the parameter is sensitive to the size of the study area. If a study area is arbitrarily truncated and affects the estimated background seismicity, we then need to be very careful of selecting the study area. Otherwise it might lose the subjective perspective. Here we applied one simple case to test the area size dependency, by dividing the study area into small sub-areas. We tested the area dependency in the western Hokuriku, Japan (Figure 4.12), for which we obtained the best combination of the parameters is $S = 0.02°$ and $T = 512$ days for the entire area. We here divided the study area into four rectangle sub-areas and computed the algorithm with the same parameter set of $S = 0.02°$ and $T = 512$ days. According to the temporal distribution of background seismicity in all areas (Figure 4.14), we found the following conclusion: 1) Background seismicity computed from the entire western Hokuriku area performed to have been closer to Poisson behavior. (2) Background seismicity rate differs from sub-area to sub-area, which also indicates the stress heterogeneity between those areas in the upper crust. The smoothed background seismicity also indicates earthquakes occurred closely in space and time that are automatically identified as spatiotemporal clusters without changing the parameter. This simple test shows that this algorithm is insensitive to the size of the study area. Once we find the best parameter set from the large area, we can adopt the same parameter set for the smaller area to estimate the background seismicity on the local or regional scale.

4.3 Compare to other models

We compared our result for the western Hokuriku region with the space-time ETAS and CURATE analyses. Figure 4.15 demonstrates the background seismicity in different algorithms, the space-time ETAS within R-package [open source from https://github.com/jalilian/ETAS] was used to reproduce the time series of declustered seismicity. Note that we used $M \geq 2.5$ for the comparison. Background seismicity estimated by the CURATE analysis shows a range of fixed day rule equal to seven days and a range of distance rule from 50 - 70 km. The background seismicity rates from our algorithms and the space-ETAS results are stable, whereas the one from the CURATE analysis is largely fluctuated. A clear increased rate of background declustered earthquakes occurred after the 2007 Chuetsu-Oki earthquake in the CURATE curves, indicating that the CURATE analysis cannot sufficiently select spatiotemporal earthquake clusters and they are sensitive to the parameter choice. In order to test the temporal Poisson behavior with other algorithms, we performed a simple dispersion test by estimating the ratio of mean and variance. In a time series with Poisson distribution, the mean rate should be equal to the variance [Dixon and Massey, 1968]. Dispersion ≥ 1 indicates some degree of clustering, while dispersion < 1 indicates more regular occurrence than a Poisson distribution [Vere-Jones, 1970]. We calculated the mean

and variance for each background seismicity by choosing a one-day bin width and counting the earthquakes occurred in each bin. The dispersion value for our result is 1.09, while ETAS is 1.03 and CURATE is a range from 1.13 - 1.36 depending on the different distance rule. This simple dispersion test proves that our algorithm is competitive with other pervasive declustering algorithms.

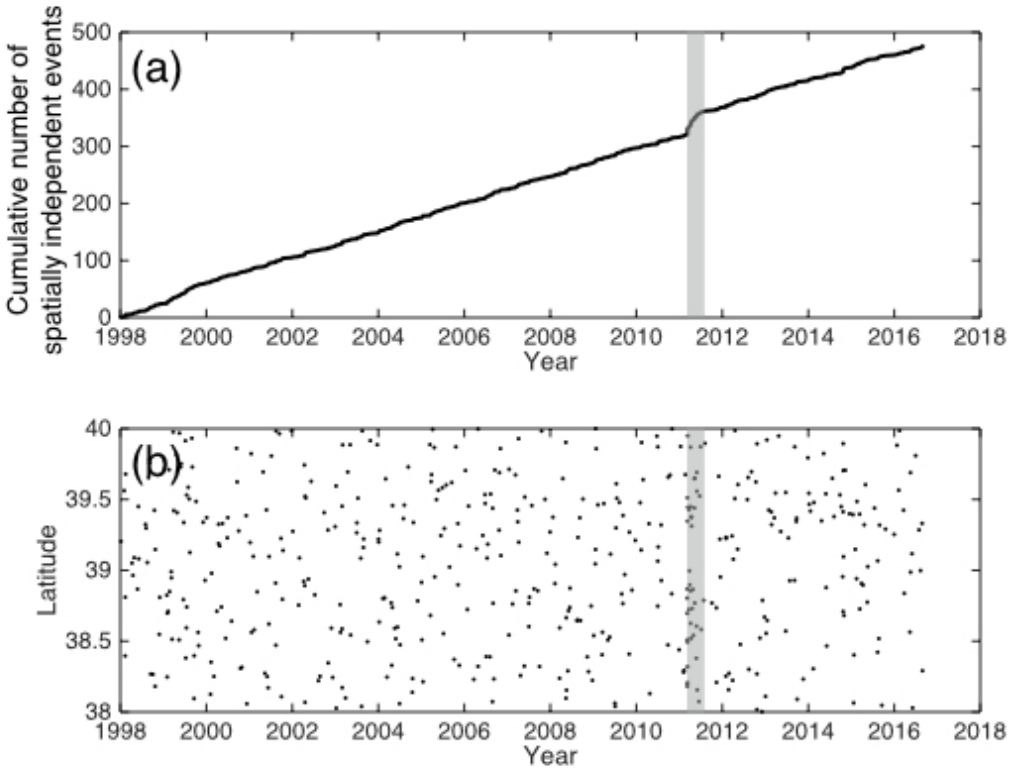

Figure 4.1 Space-time distribution of independent events in Iwate region. (a) Temporal distribution. (b) Space time distribution of latitude as a function of earthquake occurrence time. Seismicity rate increase period is marked by a gray box.

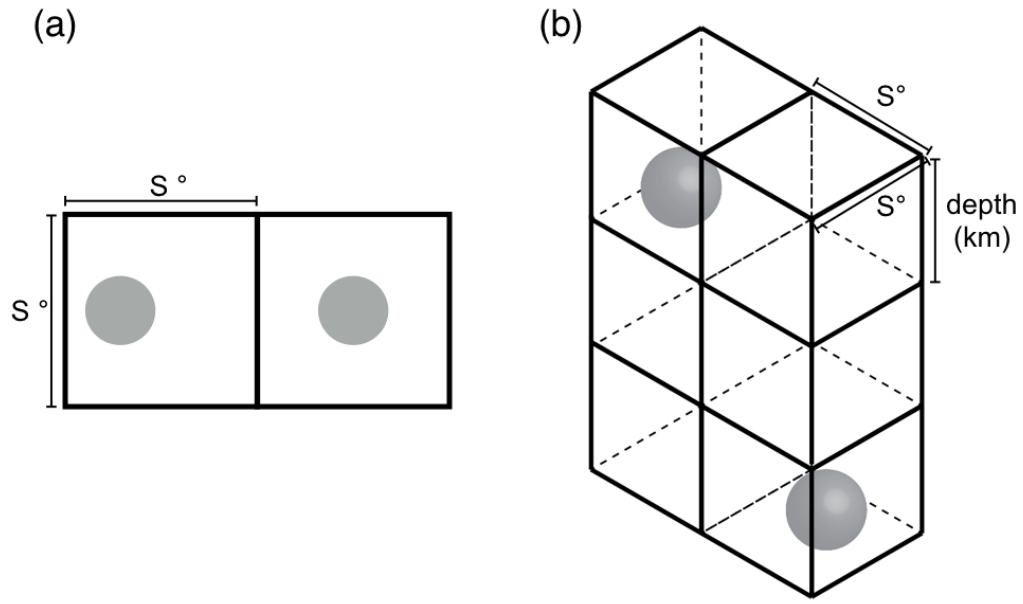

Figure 4.2 A schematic plot of (a) 2-Dimension grid and (b) 3-Dimension grid. It is clear that earthquakes occurred over a distance of a cell in depth will be linked into one spatial cluster in the 2-Dimension grid system.

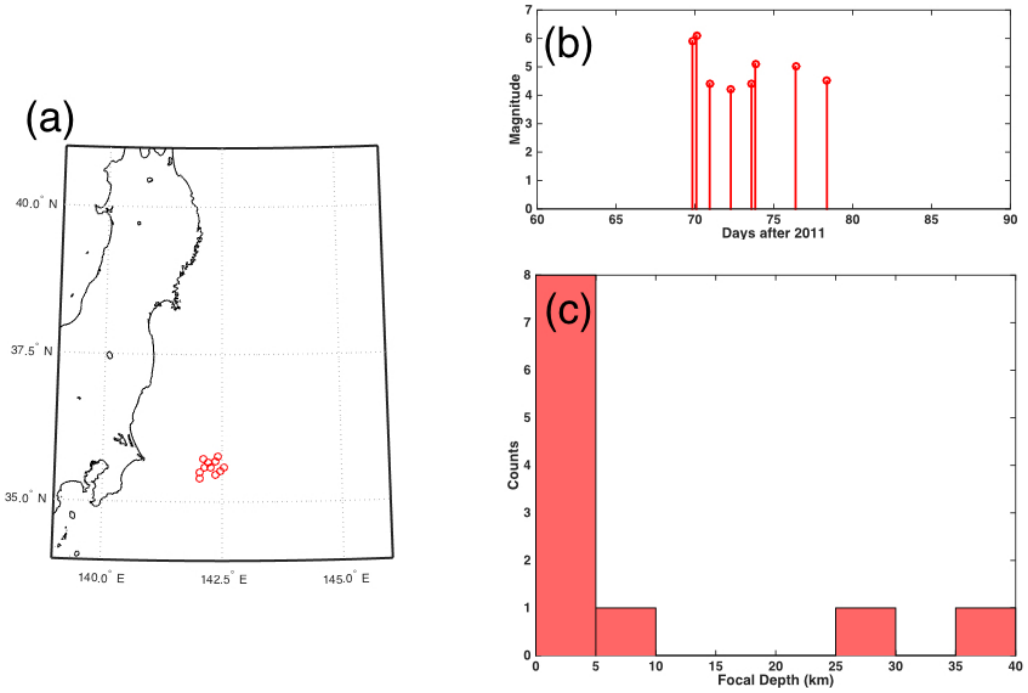

Figure 4.3 Example of one spatiotemporal sequence causing over-declustering. (a) Spatial distribution. (b) Temporal distribution. (c) Depth distribution. The depth distribution indicates that there is a 15 km hypocenter depth gap in the sequence.

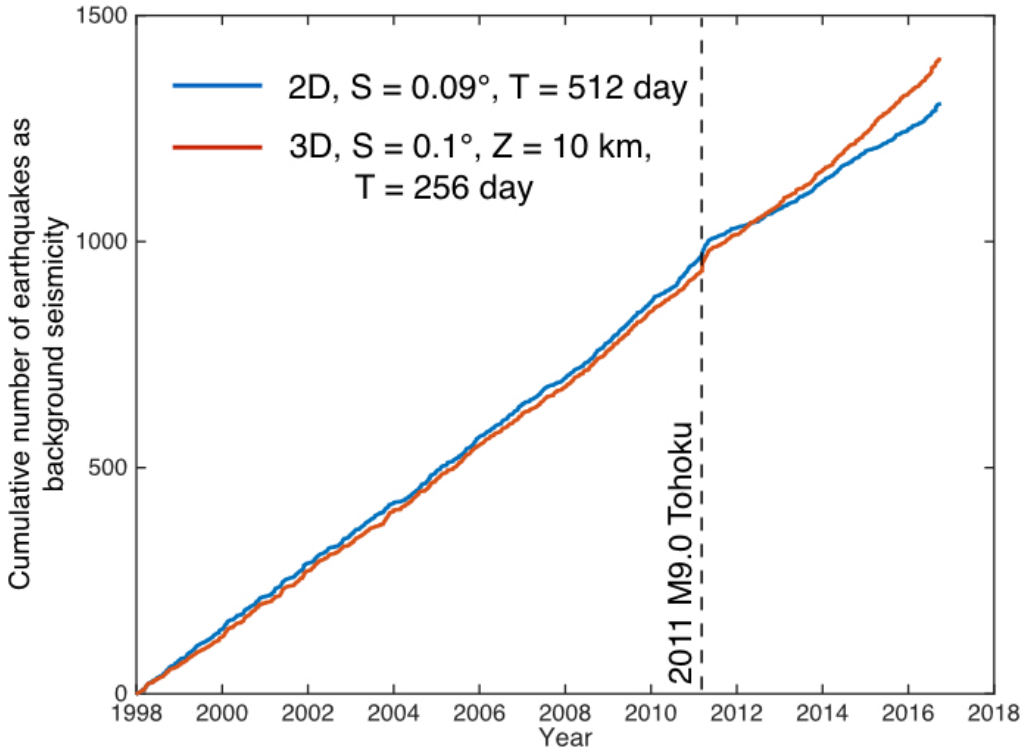

Figure 4.4 Cumulative number of background rate of seismicity from 2-D grid and 3-D grid calculations. Blue line indicates 2-D result and red line indicates 3-D result. Black dash line marks the occurrence time of the 2011 M9.0 Tohoku mainshock. The over-declustering pattern is disappeared on the 3-D result, while a sudden seismicity rate increase associated with the 2011 M9.0 Tohoku event is seen in the 2-D case.

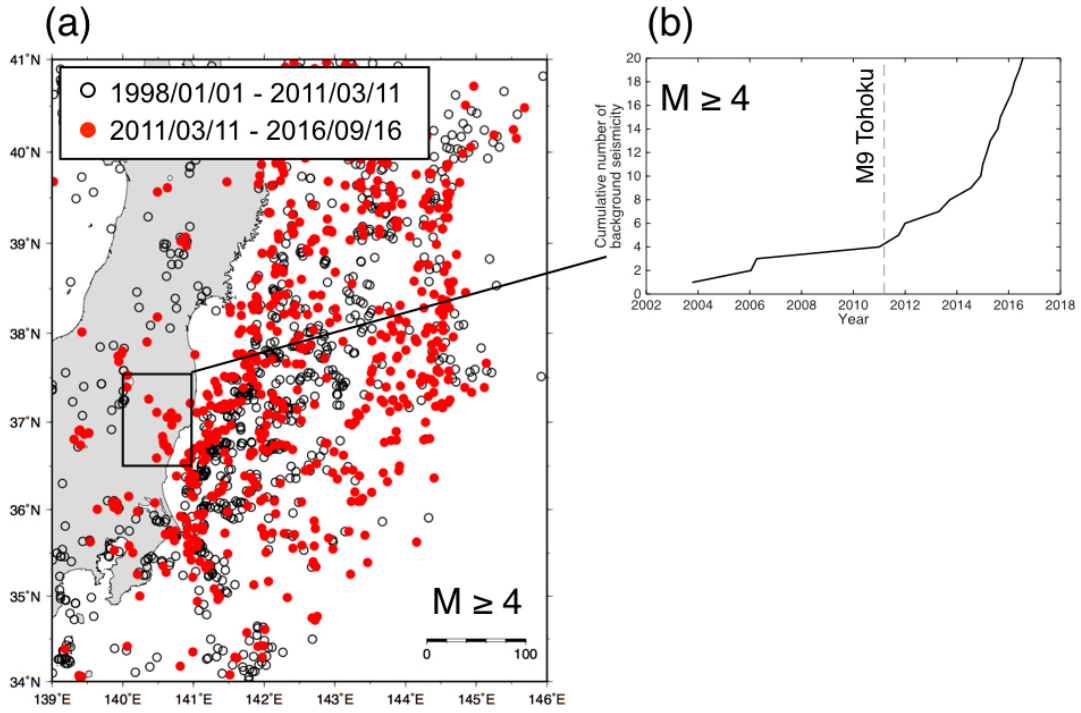

Figure 4.5 Spatial comparison of background seismicity before and after the 2011 Tohoku-oki earthquake. (a) Spatial distribution of earthquakes before and after the 2011 Tohoku earthquake. Red solid circle indicates background seismicity occurred after the Tohoku earthquake and black open circle indicates background seismicity occurred before the 2011 Tohoku earthquake. A small area of enhanced seismicity is shown in a rectangle area from 36.5° N to 37.5° N and 140.3° E to 141° N. (b) Temporal distribution of background seismicity in the rectangle area. It is evident that the background rate has changed to a new level after the Tohoku earthquake.

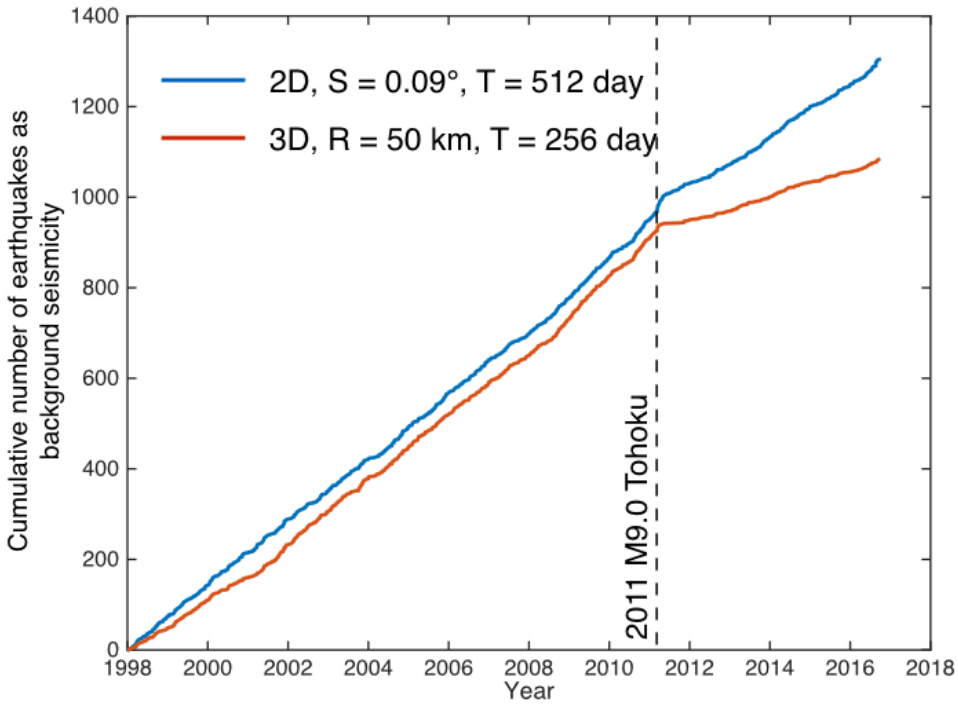

Figure 4.6 Temporal distribution of background seismicity calculated from 2-D grid and 3-D radius sphere grid. Blue line indicates 2-D result and red line indicates 3-D result. Black dash line marks the occurrence time of the 2011 M9.0 Tohoku mainshock. It is clear that background seismicity estimated from the 3-D radius is more likely to over-decluster.

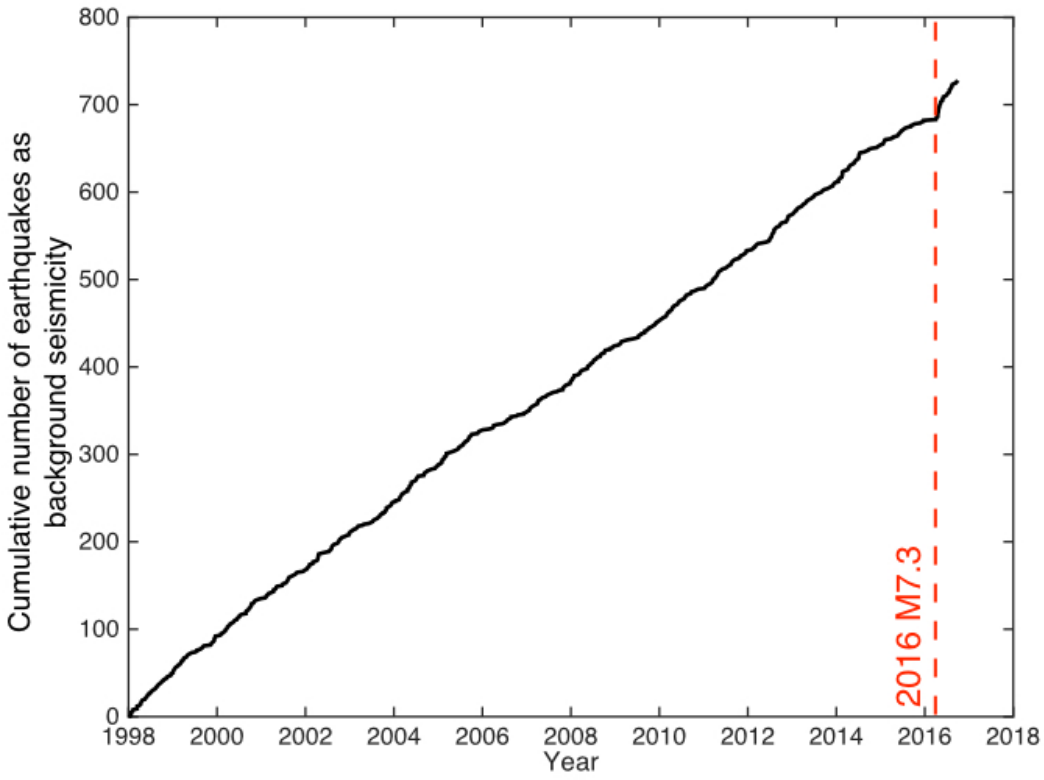

Figure 4.7 Cumulative number of spatially independent events in Central Kyushu region. Red dash line indicates the occurrence time of the 2016 Kumamoto earthquake.

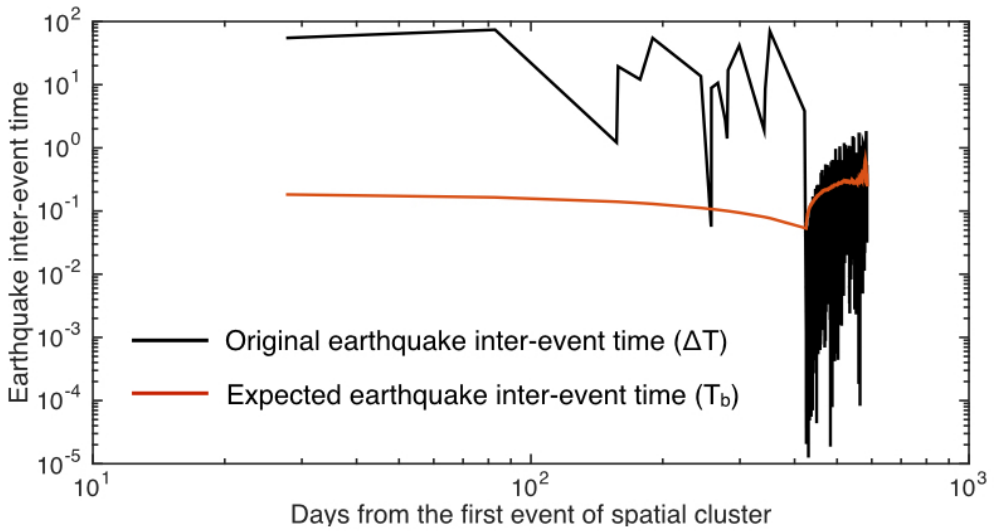

Figure 4.8 Comparison of temporal distribution of earthquake inter-event times and T_b in one spatial cluster. Black line indicates the earthquake inter-event times and red line indicates the T_b estimated from equation (2.3).

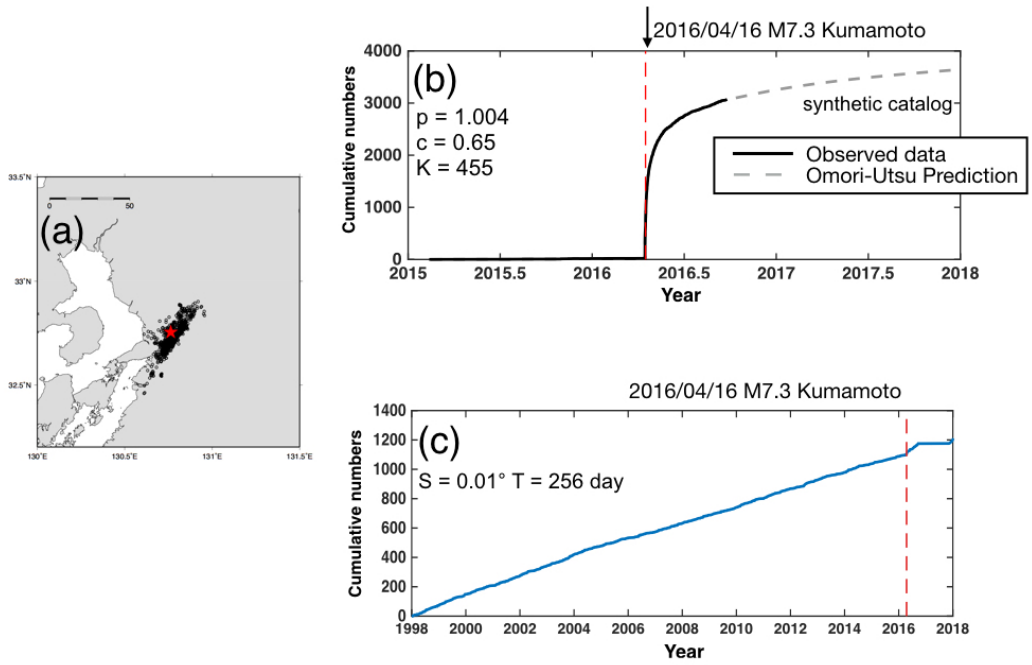

Figure 4.9 Example of synthetic earthquake catalog for one spatial cluster. (a) Spatial distribution. Black dots are M ≥ 2 events and the red star indicates epicenter of the 2016 Kumamoto mainshock. (b) Temporal distribution of seismicity. Black line is the original observed data and grey dash line indicates the synthetic data. (c) Temporal distribution of background seismicity in Central Kyushu with synthetic catalog. A more smoothed background seismicity is reproduced.

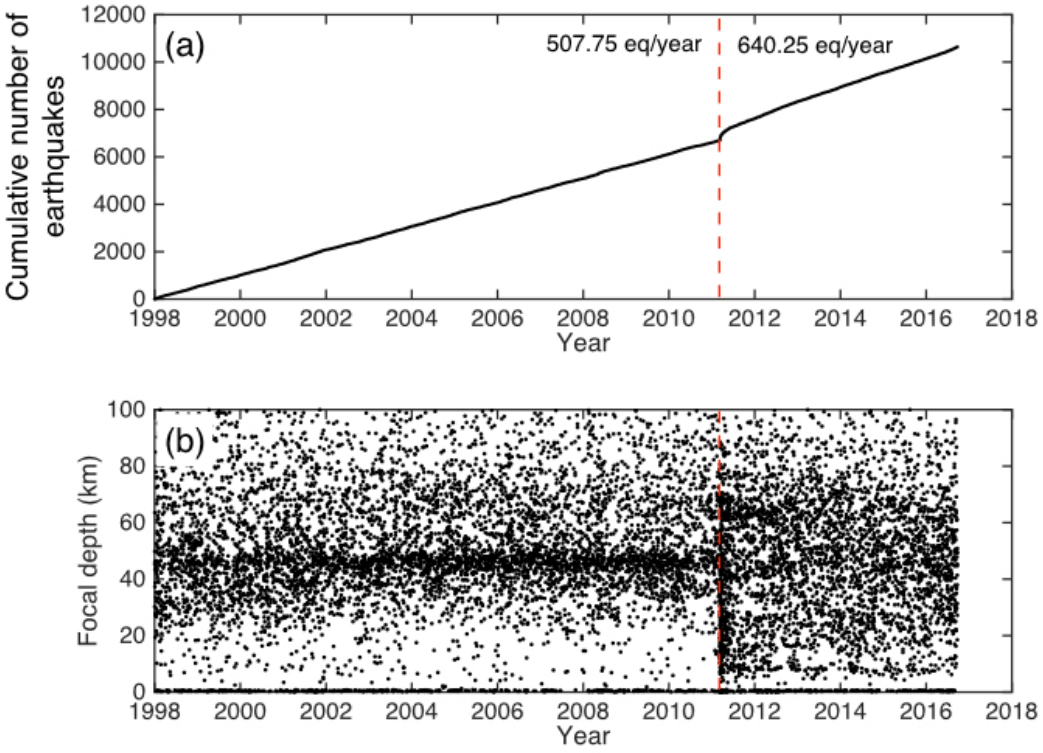

Figure 4.10 Background seismicity completed with 3-Dimension grid for Kanto region. (a) Temporal distribution. Red dash line indicates the occurrence time of the 2011 Tohoku earthquake. (b) Depth distribution of focal depth against earthquake occurrence time. A remarkable seismicity rate increase after the 2011 Tohoku earthquake is observed. The depth distribution also shows a concentration of earthquakes at depths of 60 - 80 km after the Tohoku earthquake.

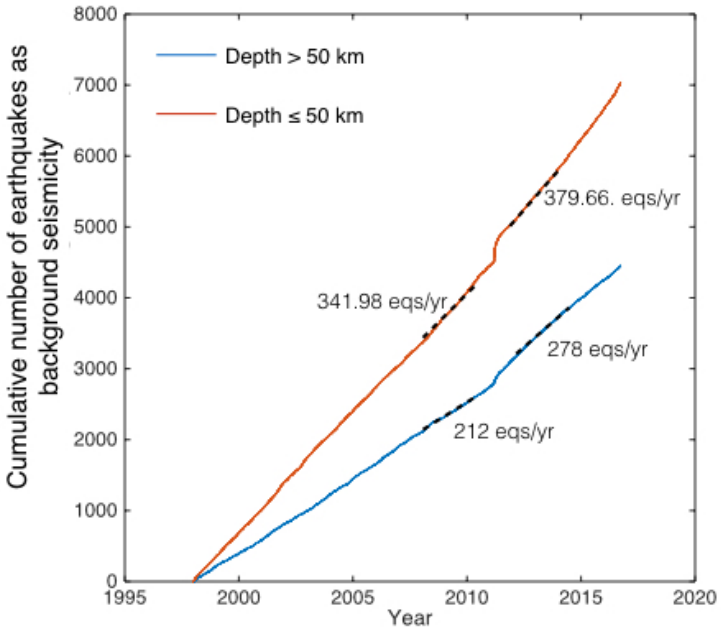

Figure 4.11 Temporal distribution of background seismicity in different depth range. Red line indicates seismicity occurred at shallower depth and blue line indicates seismicity occurred at deeper depth. A different behavior is observed that seismicity increased more rapidly in the earthquake occurred at deeper part than the shallower part.

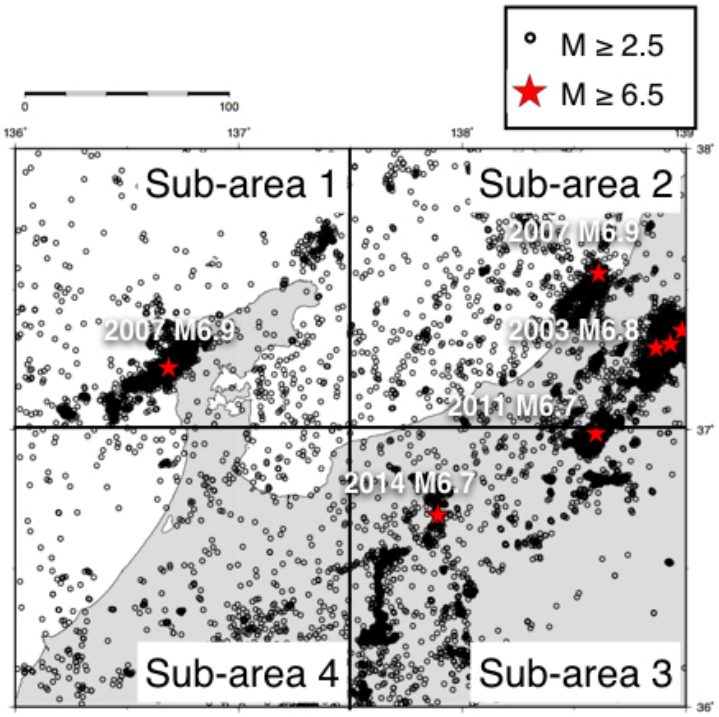

Figure 4.12 Spatial distribution of seismicity in small areas of western part of Hokuriku region, Japan. Black circle indicates M ≥ 2.5 events and red star indicates M ≥ 6.5 event. We divided this area into four sub-areas for investigating the areal dependency.

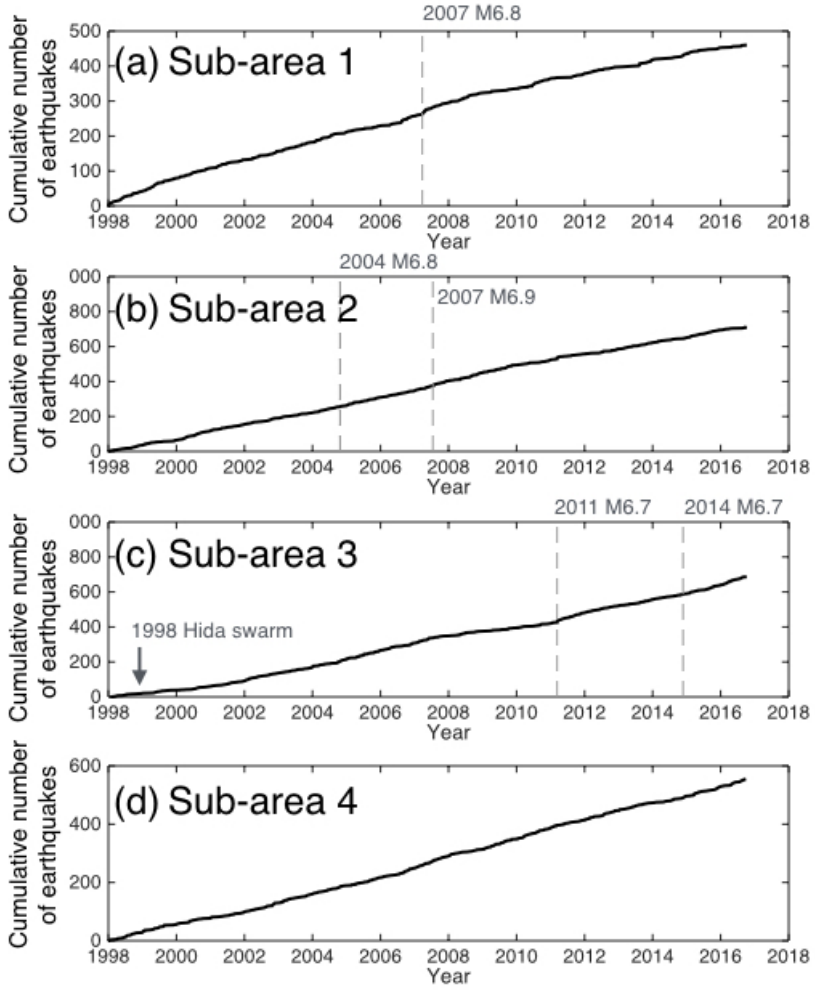

Figure 4.13 Temporal distribution of sub-areas: (a) Sub-area 1, (b) Sub-area 2, (c) Sub-area 3 and (d) Sub-area 4. Background seismicity is estimated by S = 0.02° and T = 512 day, same as the suggested parameters in Chubu region. Grey dash line indicates the occurrence time of M ≥ 6.5 event occurred in each sub-area.

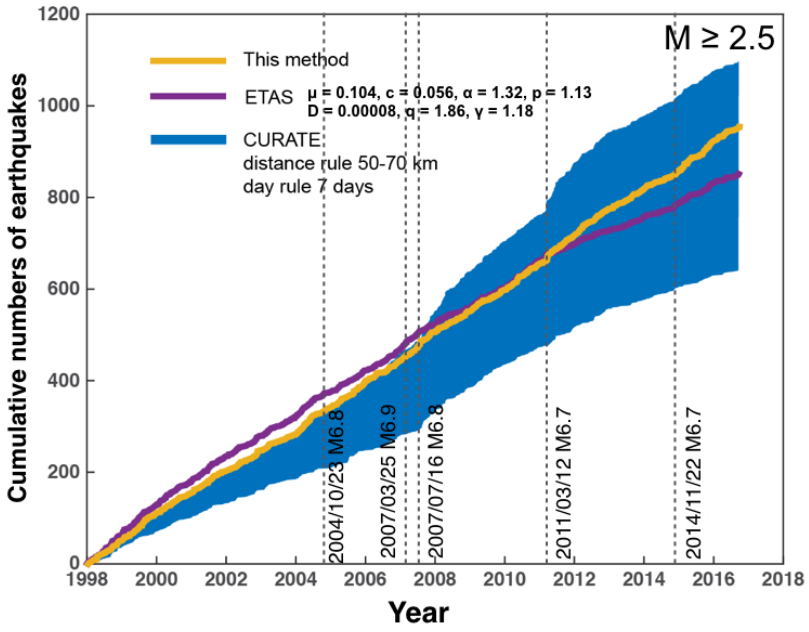

Figure 4.14 Cumulative number of earthquakes in the declustered catalogs with time for ETAS (purple), CURATE (blue) and new algorithm proposed by this study (yellow). Note that we present the CURATE with multiple parameter values. Dash black line indicates the occurrence time of M ≥ 6.5 event.

Chapter 5 Conclusion

In this study, we have developed a new algorithm to divide an original earthquake catalog into background seismicity and spatio-temporal clusters for the cases characterized by both mainshock-aftershock sequence and swarm activity with no specific assumptions. From the perspective of the better seismic hazard estimate, selecting spatiotemporal earthquake clusters provides us a clue to understand earthquake interaction, whereas background seismicity also suggests time-dependent change in stress condition and precursory signal prior to a large earthquake in a region. This new approach starts with selecting transient earthquake clusters (spatial clusters) by two free parameters, cell size in space S and time window T, which aims to find the high seismicity density areas. Then we adopted a self-derived rate parameter (backward mean inter-event time) to quantify the temporal relationship between earthquakes in each spatial cluster. We found that the backward mean inter-event time can be well applicable to screen the observed temporal sequence in a cluster with regards to mainshock-aftershock and/or swarm type sequence. Two important factors control the quality of the estimated background seismicity. One is how to select a proper spatial cluster which represents a relativity high seismicity density area from an input catalog; the other is how to define a reasonable temporal threshold for quantifying the temporal relationship between earthquakes. We designed a parameter filtering process for finding a proper parameter set from numerous possible parameter sets. The two concepts, 1) a more stable background seismicity following Poisson behavior, and 2) maximizing the number of earthquakes in the background seismicity were introduced in the filtering process to choose the best parameter combination of S and T. As a result of several representative tests with the JMA catalog in the different tectonic environments, we found that our new approach is capable of selecting earthquake clusters in terms of mainshock-aftershock sequence and/or swarm sequence. In our analysis to decluster input catalogs, several areas like Iwate region (inland southern Tohoku) and Kanto and Fukushima regions have been continuously affected by the 2011 M9.0 Tohoku-oki earthquake, which suggests that those areas might be still suffering from the post-seismic relaxation of the Tohoku-oki mainshock. We also demonstrated that the parameter choice is not so sensitive to the size of a study areas from our test of the western Hokuriku region. Finally, we proved that our algorithm is sufficiently competitive with other previous declustering techniques. But we found limitations and weakness in our new algorithm using the backward rate (inter-event time) method such as real-time application in an on-going aftershock sequence. Further tests and modifications considering the unstable and complex evolution of earthquake inter-event times might be considered as a future work.

We also expect two of our resulted catalogs can be addressed in several subjects. One of the benefits from our declustered catalog (background seismicity) is to detect a precursory seismic signal (seismic quiescence or seismic activation) prior to a large earthquake. Recently several studies reported a correlation between temporal changes of background seismicity and long-term acceleration of aseismic slip before a large event [e.g, Wu and Chiao, 2006; Kawamura and Chen, 2013; Katsumata, 2015, 2017]. We hope that this algorithm, by estimating the background seismicity in the global or regional scale, would help us understand the process of earthquake nucleation. Regarding the spatio-temporal sequence,

two interesting topics would be studied. One is to investigate earthquake interaction. In our spatio-temporal catalog, temporal relationship between sequences might help us to investigate the pattern of the sequence migration. Such migration pattern may use for demonstrating the earthquake rupture propagation or reflecting the triggering behavior due to aseismic slip or fluid migration. The other future work is to analyze the difference between different types of earthquake clusters. Seismic swarm is distinguished from mainshock-aftershock sequence with regards to the various statistical characteristics. Previous studies distinguished swarm sequence from mainshock-aftershock sequence based on the empirical Omori-Utsu law or bath's law (magnitude difference of mainshock and second large aftershock is around 1.1-1.5 [Bath, 1965]). However, swarm sequences that do not fulfill the criterion were vastly found around the world. It makes a given earthquake sequence very difficult to differentiate swarm sequence from typical mainshock-aftershock sequence. We hope that our spatio-temporal catalog can statistically characterize the difference between the mainshock-aftershock sequence and swarm sequence. After a swarm catalog is established, we can incorporate with the earthquake forecasting for the future hazard estimation.

Reference

Aki, K. (1965), Maximum likelihood estimate of b in the formula log N= a-bM and its confidence limits, *Bull. Earthq. Res. Inst., Tokyo Univ.*, *43*, 237-239.

Båth, M. (1965), Lateral inhomogeneities of the upper mantle, *Tectonophysics*, *2*(6), 483-514.

Cao, T., M. D. Petersen, and M. S. Reichle (1996), Seismic hazard estimate from background seismicity in southern California, *Bulletin of the Seismological Society of America*, *86*(5), 1372-1381.

Chouliaras, G., I. Kassaras, V. Kapetanidis, P. Petrou, and G. Drakatos (2015), Seismotectonic analysis of the 2013 seismic sequence at the western Corinth Rift, *Journal of Geodynamics*, *90*, 42-57.

Chuang, L. Y., K. H. Chen, A. Wech, T. Byrne, and W. Peng (2014), Ambient tremors in a collisional orogenic belt, *Geophysical Research Letters*, *41*(5), 1485-1491.

Cocco, M., S. Hainzl, F. Catalli, B. Enescu, A. Lombardi, and J. Woessner (2010), Sensitivity study of forecasted aftershock seismicity based on Coulomb stress calculation and rate-and state-dependent frictional response, *Journal of Geophysical Research: Solid Earth*, *115*(B5).

Dieterich, J. (1994), A constitutive law for rate of earthquake production and its application to earthquake clustering, *Journal of Geophysical Research: Solid Earth*, *99*(B2), 2601-2618.

Dieterich, J. H. (1992), Earthquake nucleation on faults with rate-and state-dependent strength, *Tectonophysics*, *211*(1-4), 115-134.

Dixon, W. J., and J. Massey Frank (1950), *Introduction To Statistical Analsis*, McGraw-Hill Book Company, Inc; New York.

Felzer, K. R., and E. E. Brodsky (2006), Decay of aftershock density with distance indicates triggering by dynamic stress, *Nature*, *441*(7094), 735.

Frohlich, C., and S. D. Davis (1990), Single-link cluster analysis as a method to evaluate spatial and temporal properties of earthquake catalogues, *Geophysical Journal International*, *100*(1), 19-32.

Gardner, J., and L. Knopoff (1974), Is the sequence of earthquakes in Southern California, with aftershocks removed, Poissonian?, *Bulletin of the Seismological Society of America*, *64*(5), 1363-1367.

Gardonio, B., D. Marsan, O. Lengliné, B. Enescu, M. Bouchon, and J. L. Got (2015), Changes in seismicity and stress loading on subduction faults in the Kanto region, Japan, 2011–2014, *Journal of Geophysical Research: Solid Earth*, *120*(4), 2616-2626.

Geller, R. J. (2011), Shake-up time for Japanese seismology, *Nature*, *472*(7344), 407-409.

Gutenberg, B., and C. F. Richter (1944), Frequency of earthquakes in California, *Bulletin of the Seismological Society of America*, *34*(4), 185-188.

Habermann, R. (1983), Teleseismic detection in the Aleutian Island arc, *Journal of Geophysical Research: Solid Earth*, *88*(B6), 5056-5064.

Habermann, R. E. (1987), Man-made changes of seismicity rates, *Bulletin of the Seismological Society of America*, *77*(1), 141-159.

Harte, D. (2012), Bias in fitting the ETAS model: A case study based on New Zealand seismicity, *Geophysical Journal International*, *192*(1), 390-412.

Hayes, G. P. (2011), Rapid source characterization of the 2011 Mw 9.0 off the Pacific coast of Tohoku earthquake, *Earth, planets and space*, *63*(7), 4.

Imanishi, K., R. Ando, and Y. Kuwahara (2012), Unusual shallow normal-faulting earthquake sequence in compressional northeast Japan activated after the 2011 off the Pacific coast of Tohoku earthquake, *Geophysical Research Letters*, *39*(9).

Institute, G. S. (1987), *Horizontal strain in Japan 1985–1883*, Association for the Development of Earthquake Prediction.

Jacobs, K. M., E. G. Smith, M. K. Savage, and J. Zhuang (2013), Cumulative rate analysis (CURATE): A clustering algorithm for swarm dominated catalogs, *Journal of Geophysical Research: Solid Earth*, *118*(2), 553-569.

Kafka, A. L. (2002), Statistical analysis of the hypothesis that seismicity delineates areas where future large earthquakes are likely to occur in the central and eastern United States, *Seismological Research Letters*, *73*(6), 992-1003.

Kagan, Y. Y. (2003), Accuracy of modern global earthquake catalogs, *Physics of the Earth and Planetary Interiors*, *135*(2), 173-209.

Kagan, Y. Y., and D. D. Jackson (2000), Probabilistic forecasting of earthquakes, *Geophysical Journal International*, *143*(2), 438-453.

Kanamori, H., and D. L. Anderson (1975), Theoretical basis of some empirical relations in seismology, *Bulletin of the seismological society of America*, *65*(5), 1073-1095.

Kato, A., A. Saiga, T. Takeda, T. Iwasaki, and T. Matsuzawa (2014), Non-volcanic seismic swarm and fluid transportation driven by subduction of the Philippine Sea slab beneath the Kii Peninsula, Japan, *Earth, Planets and Space*, *66*(1), 86.

Kato, A., S. Sakai, T. Iidaka, T. Iwasaki, and N. Hirata (2010), Non-volcanic seismic swarms triggered by circulating fluids and pressure fluctuations above a solidified diorite intrusion, *Geophysical Research Letters*, *37*(15).

Kato, A., S. i. Sakai, and K. Obara (2011), A normal-faulting seismic sequence triggered by the 2011 off the Pacific coast of Tohoku Earthquake: Wholesale stress regime changes in the upper plate, *Earth, planets and space*, *63*(7), 43.

Katsumata, K. (2015), A Long-Term Seismic Quiescence before the 2004 Sumatra (Mw 9.1) Earthquake, *Bulletin of the Seismological Society of America*, *105*(1), 167-176.

Katsumata, K. (2017), Long-Term Seismic Quiescences and Great Earthquakes in and Around the Japan Subduction Zone Between 1975 and 2012, *Pure and Applied Geophysics*, *174*(6), 2427-2442.

Kawamura, M., and C.-c. Chen (2013), Precursory change in seismicity revealed by the Epidemic-Type Aftershock-Sequences model: A case study of the 1999 Chi-Chi, Taiwan earthquake, *Tectonophysics*, *592*, 141-149.

Kilb, D. (2000), Earthquake triggering by dynamic stresses, *Nature*, *408*, 570-574.

King, G. C., R. S. Stein, and J. Lin (1994), Static stress changes and the triggering of earthquakes, *Bulletin of the Seismological Society of America*, *84*(3), 935-953.

Llenos, A. L., J. J. McGuire, and Y. Ogata (2009), Modeling seismic swarms triggered by aseismic transients, *Earth and Planetary Science Letters*, *281*(1), 59-69.

Loveless, J. P., and B. J. Meade (2010), Geodetic imaging of plate motions, slip rates, and partitioning of deformation in Japan, *Journal of Geophysical Research: Solid Earth*, *115*(B2).

Luen, B., and P. B. Stark (2012), Poisson tests of declustered catalogues, *Geophysical journal international*, *189*(1), 691-700.

Marsan, D., and O. Lengline (2008), Extending Earthquakes9 Reach Through Cascading, *Science*, *319*(5866), 1076-1079.

Matsumoto, S., S. Nakao, T. Ohkura, M. Miyazaki, H. Shimizu, Y. Abe, H. Inoue, M. Nakamoto, S. Yoshikawa, and Y. Yamashita (2015), Spatial heterogeneities in tectonic stress in Kyushu, Japan and their relation to a major shear zone, *Earth, Planets and Space*, *67*(1), 172.

Matthews, M. V., and P. A. Reasenberg (1988), Statistical methods for investigating quiescence and other temporal seismicity patterns, *Pure and Applied Geophysics*, *126*(2-4), 357-372.

Minoura, K., F. Imamura, D. Sugawara, Y. Kono, and T. Iwashita (2001), The 869 Jŏgan tsunami deposit and recurrence interval of large-scale tsunami on the Pacific coast of northeast Japan, *J. Nat. Disaster Sci.*, *23*, 83-88.

Miyazawa, M. (2016), An investigation into the remote triggering of the Oita earthquake by the 2016 Mw 7.0 Kumamoto earthquake using full wavefield simulation, *Earth, Planets and Space*, *68*(1), 205.

Mizoue, M., M. Nakamura, N. Seto, Y. Ishiketa, and T. Yokota (1983), 11. Three-layered Distribution of Microearthquakes in Relation to Focal Mechanism Variation in the Kii Peninsula, Southwestern Honshu, Japan.

Mogi, K. (1962), Study of elastic shocks caused by the fracture of heterogeneous materials and its relation to earthquake phenomena, *Bull. Earthq. Res. Inst., Univ. Tokyo*, *40*, 125-173.

Mogi, K. (1963), Magnitude-frequency relation for elastic shocks accompanying fractures of various materials and some related problems in earthquakes (2nd paper).

Mogi, K. (1979), Two kinds of seismic gaps, *pure and applied geophysics*, *117*(6), 1172-1186.

Mori, J., and R. E. Abercrombie (1997), Depth dependence of earthquake frequency-magnitude distributions in California: Implications for rupture initiation, *Journal of Geophysical Research: Solid Earth*, *102*(B7), 15081-15090.

Morita, Y., S. Nakao, and Y. Hayashi (2006), A quantitative approach to the dike intrusion process inferred from a joint analysis of geodetic and seismological data for the 1998 earthquake swarm off the east coast of Izu Peninsula, central Japan, *Journal of Geophysical Research: Solid Earth*, *111*(B6).

Nishimura, S., and M. Hashimoto (2006), A model with rigid rotations and slip deficits for the GPS-derived velocity field in southwest Japan, *Tectonophysics*, *421*(3), 187-207.

Ogata, Y. (1988), Statistical models for earthquake occurrences and residual analysis for point processes, *Journal of the American Statistical association*, *83*(401), 9-27.

Ogata, Y. (2005), Detection of anomalous seismicity as a stress change sensor, *Journal of Geophysical Research: Solid Earth*, *110*(B5).

Ohmi, S., K. Watanabe, T. Shibutani, N. Hirano, and S. Nakao (2002), The 2000 Western Tottori Earthquake—Seismic activity revealed by the regional seismic networks—, *Earth, planets and*

space, *54*(8), 819-830.

Okada, T., K. Yoshida, S. Ueki, J. Nakajima, N. Uchida, T. Matsuzawa, N. Umino, and A. Hasegawa (2011), Shallow inland earthquakes in NE Japan possibly triggered by the 2011 off the Pacific coast of Tohoku Earthquake, *Earth, planets and space*, *63*(7), 44.

Okada, Y., E. Yamamoto, and T. Ohkubo (2000), Coswarm and preswarm crustal deformation in the eastern Izu Peninsula, central Japan, *Journal of Geophysical Research: Solid Earth*, *105*(B1), 681-692.

Omori, F. (1894), *On the after-shocks of earthquakes*, The University.

Peng, Z., and J. Gomberg (2010), An integrated perspective of the continuum between earthquakes and slow-slip phenomena, *Nature Geoscience*, *3*(9), 599-607.

Reasenberg, P. (1985), Second-order moment of central California seismicity, 1969–1982, *Journal of Geophysical Research: Solid Earth*, *90*(B7), 5479-5495.

Reasenberg, P. A., and R. W. Simpson (1992), Response of regional seismicity to the static stress change produced by the Loma Prieta earthquake, *Science*, *255*(5052), 1687-1690.

Ruff, L., and H. Kanamori (1980), Seismicity and the subduction process, *Physics of the Earth and Planetary interiors*, *23*(3), 240-252.

Scholz, C. H. (2002), *The mechanics of earthquakes and faulting*, Cambridge university press.

Seno, T., and M. Yoshida (2004), Where and why do large shallow intraslab earthquakes occur?, *Physics of the Earth and Planetary Interiors*, *141*(3), 183-206.

Simons, M., S. E. Minson, A. Sladen, F. Ortega, J. Jiang, S. E. Owen, L. Meng, J.-P. Ampuero, S. Wei, and R. Chu (2011), The 2011 magnitude 9.0 Tohoku-Oki earthquake: Mosaicking the megathrust from seconds to centuries, *science*, *332*(6036), 1421-1425.

Steger, C. (1996), Extracting curvilinear structures: A differential geometric approach, *Computer Vision—ECCV'96*, 630-641.

Stein, R. S., G. C. King, and J. Lin (1994), Stress triggering of the 1994 M= 6.7 Northridge, California, earthquake by its predecessors, *Science*, *265*(5177), 1432-1435.

Stein, S., and E. A. Okal (2011), The size of the 2011 Tohoku earthquake need not have been a surprise, *Eos, Transactions American Geophysical Union*, *92*(27), 227-228.

Sugawara, D., F. Imamura, K. Goto, H. Matsumoto, and K. Minoura (2013), The 2011 Tohoku-oki earthquake tsunami: similarities and differences to the 869 Jogan tsunami on the Sendai plain, *Pure and Applied Geophysics*, *170*(5), 831-843.

Toda, S., J. Lin, and R. S. Stein (2011), Using the 2011 Mw 9.0 off the Pacific coast of Tohoku Earthquake to test the Coulomb stress triggering hypothesis and to calculate faults brought closer to failure, *Earth, planets and space*, *63*(7), 39.

Toda, S., and R. S. Stein (2013), The 2011 M= 9.0 Tohoku oki earthquake more than doubled the probability of large shocks beneath Tokyo, *Geophysical Research Letters*, *40*(11), 2562-2566.

Toda, S., R. S. Stein, G. C. Beroza, and D. Marsan (2012), Aftershocks halted by static stress shadows, *Nature Geoscience*, *5*(6), 410-413.

Toda, S., R. S. Stein, and J. Lin (2011), Widespread seismicity excitation throughout central Japan following the 2011 M= 9.0 Tohoku earthquake and its interpretation by Coulomb stress transfer,

Geophysical Research Letters, *38*(7).

Toda, S., R. S. Stein, and T. Sagiya (2002), Evidence from the AD 2000 Izu islands earthquake swarm that stressing rate governs seismicity, *Nature*, *419*(6902), 58-61.

Uchida, N., and T. Matsuzawa (2013), Pre-and postseismic slow slip surrounding the 2011 Tohoku-oki earthquake rupture, *Earth and Planetary Science Letters*, *374*, 81-91.

Uchide, T., H. Horikawa, M. Nakai, R. Matsushita, N. Shigematsu, R. Ando, and K. Imanishi (2016), The 2016 Kumamoto–Oita earthquake sequence: aftershock seismicity gap and dynamic triggering in volcanic areas, *Earth, Planets and Space*, *68*(1), 180.

Ueno, T., T. Saito, K. Shiomi, B. Enescu, H. Hirose, and K. Obara (2012), Fractional seismic velocity change related to magma intrusions during earthquake swarms in the eastern Izu peninsula, central Japan, *Journal of Geophysical Research: Solid Earth*, *117*(B12).

Ukawa, M., E. Fujita, E. Yamamoto, Y. Okada, and M. Kikuchi (2000), The 2000 Miyakejima eruption, *Earth, planets and space*, *52*(8), xix-xxvi.

Utsu, T. (1970), Aftershocks and earthquake statistics (1): Some parameters which characterize an aftershock sequence and their interrelations, *Journal of the Faculty of Science, Hokkaido University. Series 7, Geophysics*, *3*(3), 129-195.

Vere-Jones, D. (1970), Stochastic models for earthquake occurrence, *Journal of the Royal Statistical Society. Series B (Methodological)*, 1-62.

Wiemer, S. (2000), Introducing probabilistic aftershock hazard mapping, *Geophysical Research Letters*, *27*(20), 3405-3408.

Wiemer, S. (2001), A software package to analyze seismicity: ZMAP, *Seismological Research Letters*, *72*(3), 373-382.

Wiemer, S., and M. Wyss (2000), Minimum magnitude of completeness in earthquake catalogs: Examples from Alaska, the western United States, and Japan, *Bulletin of the Seismological Society of America*, *90*(4), 859-869.

Woessner, J., and S. Wiemer (2005), Assessing the quality of earthquake catalogues: Estimating the magnitude of completeness and its uncertainty, *Bulletin of the Seismological Society of America*, *95*(2), 684-698.

Wu, Y.-M., and L.-Y. Chiao (2006), Seismic Quiescence before the 1999 Chi-Chi, Taiwan, Mw 7.6 Earthquake, *Bulletin of the Seismological Society of America*, *96*(1), 321-327.

Wyss, M., and R. E. Habermann (1988), Precursory seismic quiescence, *Pure and Applied Geophysics*, *126*(2), 319-332.

Yoshida, A., K. Hosono, H. Takayama, A. Kobayashi, and K. Maeda (2011), Seismic and geodetic evidence for the existence of hot materials beneath the Wakayama swarm activity, southwestern Japan, *Tectonophysics*, *510*(1), 124-131.

Zhuang, J., Y. Ogata, and D. Vere-Jones (2002), Stochastic declustering of space-time earthquake occurrences, *Journal of the American Statistical Association*, *97*(458), 369-380.

.

Appendix A

Matlab code for identifying spatial cluster, please go to
https://www.dropbox.com/sh/abf0lj6bv1qpmie/AADpjXqZtOj9RWEdhRXZQ412a?dl=0